

# Atomic Layer Deposition of Metal Oxides for Emerging Applications

by

Sathees Kannan Selvaraj

B.Tech. (Coimbatore Institute of Technology, India) 2007

M.Tech. (Indian Institute of Technology Kanpur, India) 2009

Thesis submitted in partial fulfillment of the requirements  
for the degree of Doctor of Philosophy in Chemical Engineering  
in the Graduate College of the  
University of Illinois at Chicago, 2015

Chicago, Illinois

Defense Committee:

Christos G. Takoudis, Chair and Advisor

Gregory Jursich, Department of Bioengineering

Cortino Sukotjo, Department of Restorative Dentistry

Alan Feinerman, Department of Electrical and Computer Engineering

Jeremiah Abiade, Department of Mechanical Engineering

## ACKNOWLEDGMENTS

First and foremost, I want to thank my advisor and dissertation chair, Prof. Christos Takoudis, for his insightful suggestions and contribution to the research projects as well as the outstanding mentorship that he has provided me. I would like to thank Dr. Gregory Jursich for many helpful discussions. Thanks to my other committee members, Prof. Alan Feinerman, Dr. Cortino Sukotjo and Dr. Jeremiah Abiade for taking time out of their busy schedules to serve on my graduate committee.

I thank my group alumni Manish, Runshen, Jorge and Arman and all AMReL & IBTN lab members for their help and support during my PhD. Thanks to chemical and bioengineering department staffs Karen Milla, Bill Schmilke, John Sitasz, Jay Lin, Jessica Terrones and Lukasz Zientara for all their help. Most grateful thanks to my parents, wife and family members for their encouragement and unconditional support.

Financial support from the National Science Foundation (NSF CBET 1067424, DMR 1309114, EEC 1062943 and CBET 1346282) and Dean's Scholar award from University of Illinois at Chicago is gratefully acknowledged.

## CONTRIBUTION OF AUTHORS

Chapter 1 is a brief introduction to the research technique used in this dissertation. Chapters 2 & 3 are adapted from published manuscripts (1; 2; 3; 4; 5) for which I am the primary author. Prof. Alan Feinerman helped to collect data plotted in Figure 33 of Section 3.1. Jaya Parulekar contributed in literature review of Section 3.2. For Section 3.3, Albert Colon helped to collect Figure 47 & Figure 48 data, Jorge Rossero prepared two samples and Dr. Junxia Shi reviewed the manuscript. Section 3.4 is under review for publication, for which, Siliang Chang prepared bacteria stock solution, Arghya Bishal aided in generating Figure 52 and Arman Butt prepared polished Ti-V samples. As a primary author, I performed all other experiments and wrote the manuscripts. My advisor, Prof. Christos G. Takoudis helped to conceive the projects and in correcting manuscripts. Dr. Gregory Jursich contributed through helpful discussions and reviewed section 2.1.

## TABLE OF CONTENTS

<b><u>CHAPTER</u></b>		<b><u>PAGE</u></b>
<b>1</b>	<b>INTRODUCTION . . . . .</b>	<b>1</b>
1.1	ALD Process . . . . .	1
1.2	History of ALD . . . . .	2
1.3	ALD State-of-the-art . . . . .	4
1.4	Thesis overview . . . . .	4
<b>2</b>	<b>EXPERIMENTAL . . . . .</b>	<b>6</b>
2.1	Design of ALD/CVD hybrid reactor . . . . .	6
2.1.1	Introduction . . . . .	6
2.1.2	System Description . . . . .	9
2.1.3	Control System Implementation . . . . .	15
2.1.4	Experimental Verification . . . . .	16
2.1.5	Summary . . . . .	24
2.2	Scalable control program for ALD/CVD hybrid reactor . . .	24
2.2.1	Introduction . . . . .	24
2.2.2	ALD Reactor Operation . . . . .	26
2.2.3	Control Program Operation . . . . .	27
2.2.4	Master Program . . . . .	32
2.2.5	Sub-VI programs . . . . .	34
2.2.6	Program testing . . . . .	43
2.2.7	Summary . . . . .	43
<b>3</b>	<b>RESULTS AND DISCUSSION . . . . .</b>	<b>45</b>
3.1	ALD of SnO <sub>x</sub> . . . . .	45
3.1.1	Introduction . . . . .	45
3.1.2	Experimental . . . . .	46
3.1.3	Results and Discussion . . . . .	48
3.1.4	Summary . . . . .	63
3.2	Selective ALD of ZrO <sub>2</sub> . . . . .	65
3.2.1	Introduction . . . . .	65
3.2.2	Experimental . . . . .	68
3.2.3	Results and Discussion . . . . .	69
3.2.4	Summary . . . . .	76
3.3	ALD of HfO <sub>2</sub> using ethanol . . . . .	78
3.3.1	Introduction . . . . .	78
3.3.2	Experimental . . . . .	80
3.3.3	Results and Discussion . . . . .	82

## TABLE OF CONTENTS (Continued)

<u>CHAPTER</u>		<u>PAGE</u>
	3.3.4 Summary . . . . .	97
	3.4 ALD of SnTiO <sub>x</sub> . . . . .	97
	3.4.1 Introduction . . . . .	97
	3.4.2 Materials and Methods . . . . .	100
	3.4.3 Results and Discussion . . . . .	101
	3.4.4 Summary . . . . .	106
<b>4</b>	<b>CONCLUSION AND FUTURE WORK . . . . .</b>	<b>110</b>
	4.1 Conclusion . . . . .	110
	4.1.1 Design of portable ALD/CVD hybrid system . . . . .	110
	4.1.2 Scalable control program for the hybrid system . . . . .	111
	4.1.3 ALD of SnO <sub>x</sub> . . . . .	112
	4.1.4 Selective ALD of ZrO <sub>2</sub> . . . . .	113
	4.1.5 ALD of HfO <sub>2</sub> using ethanol . . . . .	113
	4.1.6 ALD of SnTiO <sub>x</sub> . . . . .	114
	4.2 Future Work . . . . .	115
	4.2.1 SALD of metal oxides and metals . . . . .	115
	4.2.2 ALD on biomaterials . . . . .	115
	<b>CITED LITERATURE . . . . .</b>	<b>117</b>
	<b>APPENDICES . . . . .</b>	<b>131</b>
	<b>Appendix A . . . . .</b>	<b>132</b>
	<b>Appendix B . . . . .</b>	<b>135</b>
	<b>VITA . . . . .</b>	<b>137</b>

## LIST OF FIGURES

<b>FIGURE</b>		<b>PAGE</b>
1	Schematic of the ALD process showing substrate surface with active nucleation centers (a), ALD Sub-cycle 1: Precursor pulse (b), Sub-cycle 2: Precursor purge (c), Sub-cycle 3: Oxidizer pulse (d), Sub-cycle 4: Oxidizer purge. Arrows indicate ALD processing sequence. . . . .	3
2	Schematic diagram of the ALD/CVD hybrid reactor system. . . . .	12
3	3-Dimensional representation of the portable ALD/CVD system. (Only major components are shown). . . . .	13
4	Schematic diagram of homemade UV-ozone generator. . . . .	15
5	(a) LabVIEW block diagram for ALD mode in a single delivery line ALD/CVD hybrid system. (b) ALD Recipe for ALD/CVD system with two delivery lines. . . . .	17
6	Effect of precursor pulse time on TiO <sub>2</sub> ALD growth rate at 200 °C substrate temperature. The bubbler temperature was at 65 °C. The system pressure was 0.5 Torr. The vertical error bars indicate film uniformity across the sample. . . . .	18
7	Effect of oxidizer (water vapor) pulse time on TiO <sub>2</sub> ALD growth rate. All ALD conditions are the same as those in Figure 6. . . . .	19
8	TiO <sub>2</sub> ALD growth rate as a function of reactor temperature. Other conditions are the same as in Figure 6. . . . .	20
9	TiO <sub>2</sub> ALD growth rate as a function of number of ALD cycles. The substrate was at 200 °C. The growth rate is constant at 0.04 nm/cycle. . . . .	21
10	XPS spectra for atomic layer deposited 30 nm-thick TiO <sub>2</sub> at 200 °C substrate temperature with TDEAT and water. . . . .	22
11	Low magnification TEM image of as-deposited ALD-TiO <sub>2</sub> /CVD-SnO <sub>x</sub> hybrid film deposited at 250 °C substrate temperature. . . . .	25
12	Schematic representation of flow-type ALD system with four precursor delivery lines named A, B, C and D. More precursor lines can be added without affecting the overall system design and control program logic. . . . .	28
13	Valve status (T-Open & F-Close) for different sub-cycles during ALD using precursor delivery line-A. Valve number V1-3 and V13 are indicated in Figure 12. . . . .	29
14	Front panel of the ALD control program. All input parameters are grouped on left boxes. The right side box shows valve status and the deposition times. . . . .	30
15	Algorithmic representation of the basic program operation and flow. Four layers are shown here, which can be scaled down or up. . . . .	31
16	LabVIEW block diagram of the ALD program. The program consists of six custom-written sub-VI programs. . . . .	33

## LIST OF FIGURES (Continued)

<u>FIGURE</u>		<u>PAGE</u>
17	Sub VI: ALD Sub Cycle Recipe. This sub-VI uses loop-index number to identify the current sub-cycle and returns the corresponding sub-cycle recipe. . . . .	35
18	LabVIEW block diagram of the ALD Cycle Ratio Index Sub VI. It returns Ratio-index number to ALD Ratio Selector sub-VI. . . . .	36
19	Sub VI: ALD Ratio Selector. It assigns sub-cycle recipe to the active layer and closes all other valves. Also it passes the corresponding sub-cycle times to ALD Cycle Clock sub-VI. . . . .	38
20	Sub VI: ALD Precursor Selector. The sub-VI has four case structures to represent four layers, with five cases for each case structure. . . . .	40
21	Sub VI: ALD Cycle Clock. This sub-VI is used to halt the loop iteration during ALD cycles. The output of this program is sent to Wait function as shown in Figure 16. . . . .	41
22	The Sub VI ALD Time shown here calculates total deposition time and time remaining using the ALD sub-cycle times, layer ratio and total number of super cycles. . . . .	42
23	Outcome of the ALD test run showing valve status of the all 13 valves during different ALD sub-cycles. The program starts with opening the by-pass valve of the Layer-1 precursor line and end with closing all the valves. . . . .	44
24	Sn(acac) <sub>2</sub> precursor saturation curve. The Si(100) substrate was at 200 °C. The Sn(acac) <sub>2</sub> precursor was kept at 70 °C. The system pressure was 0.5 Torr. The vertical error bars indicate film uniformity across the sample. Ozone pulsing time was kept constant at 1s. . . . .	49
25	Ozone oxidizer saturation curve showing the effect of ozone dosage on the SnO <sub>x</sub> film growth rate. Deposition conditions are the same as those in Figure 24. . . . .	50
26	SnO <sub>x</sub> film growth rate as a function of substrate temperature. ALD was carried out using 6 s precursor pulse: 15 s N <sub>2</sub> purge : 1 s oxidizer pulse : 15 s N <sub>2</sub> purge. The precursor was kept at 70 °C and the deposition was carried out at 0.5 Torr. . . . .	52
27	Thickness tunability of SnO <sub>x</sub> ALD process carried out at 200 °C. Deposition conditions are the same as those mentioned in Figure 26. . . . .	53
28	Si 2p core scans of 4 nm-thick SnO <sub>x</sub> film before and after 600 °C annealing in nitrogen ambient for 5 min. Films were deposited at 200 °C. Other deposition conditions are the same as those in Figure 26. . . . .	55
29	Sn 3d core scans of 20 nm-thick SnO <sub>x</sub> as-deposited films showing the effect of Ar <sup>+</sup> beam sputtering. The film deposition was carried out at 200 °C using the ALD deposition conditions mentioned in Figure 26. . . . .	56
30	GIXRD of as-deposited and annealed 30 nm-thick SnO <sub>x</sub> films. Films were deposited at 200 °C. Other ALD conditions are the same as those in Figure 26. The annealing was carried out for 5 min in nitrogen. . . . .	58

## LIST OF FIGURES (Continued)

<u>FIGURE</u>		<u>PAGE</u>
31	Refractive index (at 450 nm) of $\text{SnO}_x$ films deposited at different substrate temperatures using the ALD deposition conditions mentioned in Figure 26 . . . . .	60
32	RMS roughness values of as-deposited and annealed $\text{SnO}_x$ films. Growth conditions are the same as those in Figure 26. $\text{SnO}_x$ films were deposited at 200 °C. Annealing was performed for 5 min in nitrogen. . . . .	62
33	Current-voltage characteristics of as-deposited at 200 °C and post deposition annealed $\text{SnO}_x$ films (main); Resistivity of 20 nm-thick $\text{SnO}_x$ film deposited at 200 °C (inset (a)), post-deposition annealed at 600 °C for 5 min in nitrogen ambient (inset (b)), and deposited at 300 °C followed by annealing at 600 °C for 5 min in nitrogen (inset (c)). . . . .	64
34	Schematic illustration of processing steps proposed for the SALD of $\text{ZrO}_2$ using ethanol as the oxygen source. . . . .	67
35	$\text{ZrO}_2$ -ALD film thickness as a function of ALD cycle number showing excellent thickness tunability of the process on the silicon side of the substrate using ethanol as the oxygen source. The deposition was carried out at 200 °C substrate temperature and 500 mTorr deposition pressure using 6 s ZyALD : 15 s Ar : 10 s ethanol : 20 s Ar pulses. . . . .	70
36	XPS spectra of the silicon side of the substrate after 0 (a), 50 (b) and 100 (c) ALD cycles. Upon 5 min of $\text{Ar}^+$ beam sputtering, the C 1s peak disappeared (d). All deposition conditions are the same as those mentioned in Figure 35. . . . .	72
37	XPS spectra on copper side of the substrate after 0 (a), 70 (b), 100 (c) and 200 (d) ALD cycles, showing the onset of the $\text{ZrO}_2$ -ALD film growth only after 100 or more ALD cycles. The ALD conditions are the same as those in Figure 35. . . . .	74
38	XPS survey scans on copper surface after 50 $\text{ZrO}_2$ ALD cycles using water (a) and oxygen (b) as the ALD oxygen sources. All other ALD parameters are the same as those in Figure 35. . . . .	75
39	Change in sheet resistance ( $(R-R_o)/R_o$ ) of copper layer in as-deposited ( $R_o$ ) and annealed ( $R$ ) Cu/2 nm-thick $\text{ZrO}_2/\text{Si}$ structures. The annealing was carried out in 20 slpm of $\text{N}_2$ for 5 min. . . . .	77
40	ALD $\text{HfO}_2$ growth rate on Si(100) as a function of precursor pulse time at 200 °C and 500 mTorr. TDEAH was kept at 60 °C. . . . .	84
41	ALD $\text{HfO}_2$ growth rate on Si(100) as a function of oxidizer (ethanol) pulse time. . . . .	85
42	Growth rate of $\text{HfO}_2$ as a function of ALD reactor temperature. ALD cycle times used are 5 s precursor pulse : 15 s purge : 1 s oxidizer pulse : 15 s purge. . . . .	87
43	Growth rate of $\text{HfO}_2$ as a function of number of ALD cycles carried out at 200 °C. Schematic representation of the TDEAH molecule is shown in inset. . . . .	88



## LIST OF FIGURES (Continued)

<u>FIGURE</u>		<u>PAGE</u>
44	Hf 4f (a) and O 1s (b) core spectra of 35 nm-thick HfO <sub>2</sub> sample deposited at 200 °C and annealed at 700 °C for 5 min in nitrogen ambient. Spectra were taken after 20 min of Ar <sup>+</sup> beam sputtering. ALD cycle times used were the same as those in Figure 42. . . . .	89
45	C 1s core XPS spectra showing the removal of surface carbon contamination upon 15 min Ar <sup>+</sup> beam sputtering. . . . .	91
46	Si 2p core spectra of as-deposited and annealed 4 nm-thick HfO <sub>2</sub> film showing the formation of SiO <sub>2</sub> interface upon high temperature annealing in nitrogen ambient for 5 min. . . . .	92
47	Normalized capacitance-voltage curves of as-deposited and annealed samples prepared using ethanol and water as the ALD oxygen sources. The thickness of films is 35 nm. All other deposition and annealing conditions are the same as those in Figure 44. . . . .	95
48	Current-voltage characteristics of 35 nm-thick as-deposited and annealed ALD HfO <sub>2</sub> deposited using ethanol and water as the ALD oxygen sources. Film deposition and annealing conditions were those mentioned in Figure 44. . . . .	96
49	TiO <sub>2</sub> and SnO <sub>x</sub> film thickness as a function of number of ALD cycles carried out at 200 °C on silicon(100) substrate. TDEAT and Sn(acac) <sub>2</sub> were used as titanium and tin sources, respectively. ALD reactor pressure was kept at 0.5 Torr. . . . .	103
50	XPS survey (a), Ti 2p (b), Sn 3d (c), O 1s (d) and C 1s (e) spectra of 50% Sn doped TiO <sub>2</sub> thin film deposited at 200 °C showing contamination-free clean film with appropriate chemical nature. . . . .	105
51	The number of survived e-coli bacteria in six groups after 3 min of UV exposure. The bar graph values represent mean values of six experiments and the error bar indicates standard deviation. . . . .	107
52	Representative pictures of survived e-coli bacterial colonies in six experimental groups. Inoculated agar plates were incubated at 37 °C for 12 hrs. . . . .	108

## SUMMARY

Thin films are used in many industries, such as semiconductor, energy, catalysis, automobile, biomedical industries etc. Deposition of thin films with desired thickness, composition, purity and crystalline structure are the key to achieve superior device performance and functionality. Different deposition methods, such as sputtering, electron beam evaporation, molecular beam epitaxy, pulsed laser deposition, sol-gel deposition, spin coating, chemical vapor deposition (CVD) and atomic layer deposition (ALD), were developed to cater different applications. Of particular interest is the recently developed ALD technique. ALD is the bottom-up, vapor phase deposition technique with many unique characteristics. Bottom-up nature of the ALD process offers excellent control on thickness and composition and superior conformality.

ALD technique, that was first developed in 1970's took about two decades of research before becoming a mainstream production tool. Even though ALD was primarily developed by semiconductor industries, it is now widely used in other industries. This thesis focuses on the development of a novel portable ALD/CVD hybrid reactor, reactor control architecture and applicability of ALD in different emerging application areas. Design aspects of the portable reactor and its scalable LabVIEW control program are discussed in detail. ALD of titanium oxide and CVD of tin oxide was used to test and optimize the hybrid reactor. Film growth rate and stoichiometry were comparable to literature values.

ALD of tin oxide was studied for transparent conducting oxide application, often used in optoelectronic devices. ALD was performed using tin(II)acetylacetonate as a new tin precursor

## SUMMARY (Continued)

and ozone as the oxygen source. Linear growth rate of 0.1 nm/cycle was achieved within ALD temperature window (175 to 300 °C). Resistivity of the films were in the order of 0.3  $\Omega$ -cm.

A novel ethanol based ALD process was developed for selective ALD (SALD) of metal oxides. SALD process is unique in that no lithography or patterning techniques are needed for selective deposition. SALD of  $\text{ZrO}_2$  was carried out on copper patterned silicon substrates using ethanol as the oxygen source. Ethanol served as ALD oxygen source on silicon side and copper reducing agent on copper side of the substrate. The ethanol based SALD process was able to prevent ALD deposition on copper side up to at least 70 ALD cycles. The  $\text{ZrO}_2$  nano film was found to withstand temperatures as high as 700 °C. Ethanol based ALD process was then further studied for deposition of hafnium oxide for high-k application. The hafnium precursor, tetrakis(diethylamino)hafnium showed good reactivity with ethanol and exhibited ALD growth behavior. Film growth rate of 0.05 nm/cycle was observed within the temperature window of 200-280 °C.  $\text{HfO}_2$  films showed leakage current density of  $5 \times 10^{-8}$  A/cm<sup>2</sup> at 1 V gate bias, which is comparable to films prepared with water based ALD process.

ALD of Sn-doped  $\text{TiO}_2$  on Ti-V surface was studied for photoactivated disinfection of biomedical implants. In this study, ALD was used to change the surface composition of titanium based biomedical implants. Ultra-thin films ( $\sim 15$  nm) of tin-doped titanium oxide showed excellent antibacterial activity. Up to 98.5% disinfection was achieved within 3 min of low intensity UV exposure at a bacterial killing rate of 18 million/min-cm<sup>2</sup> of implant surface.

## CHAPTER 1

### INTRODUCTION

[Part of this chapter is adapted from my published manuscripts. (1; 2; 3; 4; 5)]

Thin films are characterized by materials or layer of materials of Ångstrom to nanometer thickness. These films are used in wide range of application ranging from microelectronics, fuel cells to biomaterials. Thin films are deposited by different techniques such as spin coating, plating, sol-gel, e-beam evaporation, molecular beam epitaxy, pulsed laser deposition, sputtering, chemical vapor deposition (CVD) and atomic layer deposition (ALD). These deposition techniques are broadly classified into physical and chemical deposition, based on the way the film reacts with underlying substrate. Chemical deposition can further be classified into CVD and ALD. Each of these deposition methods has its own advantages and limitations. This thesis is focused on ALD of metal oxides. Ultra-thin ( $< 50$  nm) films of metal oxides were deposited for microelectronics, energy and biomedical applications. This chapter introduces the ALD technique, its history and current state-of-the-art.

#### 1.1 ALD Process

ALD is performed by sequential and self-limited exposure of reactants to substrate surface in cyclic manner. Each ALD cycle typically consists of four sub-cycles (Figure 1). In the first sub-cycle, the substrate surface is exposed to precursor vapors until saturation. The precursor vapors chemisorb on the nucleation sites of the substrate surface and form a layer of adsorbed precursor molecules. The excess precursor molecules are purged out in the second sub-cycle,

called precursor purging step. The purging steps in between precursor and oxidizer pulsing steps differentiate ALD from the CVD process; in which, both precursor and oxidizer streams flow into the chamber simultaneously. Once all excess precursor molecules are purged out, the second reactant, typically an oxygen source such as water vapor, oxygen or ozone is introduced into the chamber. This oxidizer reacts with the adsorbed precursor molecules and forms a layer of material on the substrate surface and also generates gaseous by-products. The oxidizer exposure also prepares the film surface for precursor adsorption in the next precursor pulse. The unreacted oxidizer and the ALD reaction by-products such as  $\text{CO}_2$ ,  $\text{H}_2\text{O}$ ,  $\text{NH}_3$  etc., (6) are purged out of the chamber in the last ALD sub-cycle, called oxidizer purging step. These four sub-cycles deposit a layer of material of specific thickness, typically  $\sim 0.1$  nm/cycle. These steps are repeated cyclically until desired film thickness is achieved.

## **1.2 History of ALD**

Unlike CVD, ALD is a relatively new technique developed in 1960's and 1970's by two independent investigators. (7) In 1960s, the concept of ALD was developed under the name of "Molecular Layering" by Soviet researchers Profs. Valentin Borisovich Aleskovskii and S.I. Kol'tsov. The same technique was developed independently by a Finnish researcher Prof. Tuomo Suntola in 1970's under the name of "Atomic Layer Epitaxy" for electroluminescent flat panel application. After some initial lag period in 1980's, the interest in ALD process resumed in mid-1990's due to the advent of microelectronic industries. Commercial application of ALD in microelectronic industry was achieved in 2000s.

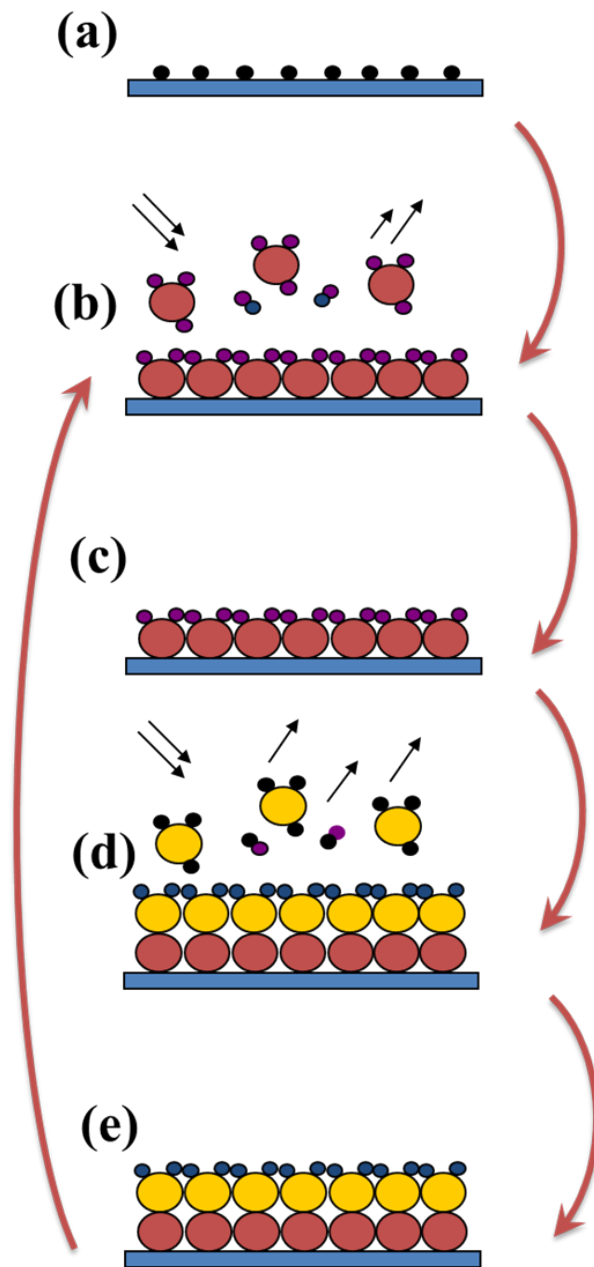


Figure 1: Schematic of the ALD process showing substrate surface with active nucleation centers (a), ALD Sub-cycle 1: Precursor pulse (b), Sub-cycle 2: Precursor purge (c), Sub-cycle 3: Oxidizer pulse (d), Sub-cycle 4: Oxidizer purge. Arrows indicate ALD processing sequence.

### 1.3 ALD State-of-the-art

Ever since the commercialization of ALD process by semiconductor industries, flurry of research activities are being carried out in other application areas, such as catalysis, sensors, optoelectronics, biomaterials, protective and decorative coatings etc. Variants of conventional ALD process, such as selective ALD process, atomic layer infiltration, molecular layer deposition, alcohol based ALD process etc., (4; 5; 8; 9; 10; 11; 12) are also explored to cater emerging new applications. Of these, a chapter of this thesis touches upon alcohol based selective ALD process for back-end-of-the-line (BEOL) related semiconductor application.

### 1.4 Thesis overview

The thesis is divided into two sections. The first section (Experimental) describes the design of ALD/CVD reactor and second section (Results and Discussion) describes the usage of ALD in emerging application areas. Chapter 2.1 summarizes design, fabrication and testing of a portable ALD/CVD hybrid reactor used in this work.  $\text{TiO}_2$  ALD process, that was used to test the reactor, is also included in this chapter. The hybrid reactor's LabVIEW control program is given in chapter 2.2. Chapter 3.1 presents growth behavior and properties of atomic layer deposited tin oxide on silicon from novel tin(II)acetylacetonate precursor and ozone. A novel chemical approach for selective ALD of metal oxides on metal oxide surface is described in chapter 3.2. Chapter 3.3 compares the growth and dielectric behavior of atomic layer deposited hafnium oxide while using ethanol as the oxygen source against water based ALD process. Atomic layer deposited tin-doped titanium oxide nanofilm for enhanced pho-

toactivated antibacterial applications on titanium-based biomedical implants is discussed in chapter 3.4. Conclusion and future direction of all the projects are given in chapter 4.



## CHAPTER 2

### EXPERIMENTAL

This chapter is divided into two sections. Design of ALD/CVD hybrid reactor is described in detail in the first section. LabVIEW control program developed for the hybrid reactor is explained in the second section.

#### **2.1    Design of ALD/CVD hybrid reactor**

This section was previously published as "Design and implementation of a novel portable atomic layer deposition/chemical vapor deposition hybrid reactor" in Review of Scientific Instruments.

##### **2.1.1    Introduction**

Functional thin films form the backbone of many technologies in microelectronics, optoelectronics, and chemical industries by providing functional thin film surface coatings related to catalysis, solar panels and batteries (13; 14; 15; 16; 17; 18), for example. These films function in diverse thickness scale from micrometers to nano-meters. Often, functionality of such films requires high purity at precise composition. Even minuscule impurity incorporation can be detrimental on device performance; therefore, it becomes necessary to avoid impurity contamination. Multi-chamber cluster tools are commonly employed to avoid contamination during processing steps (19). Though it has an advantage of using separate chamber for each processing steps, they are rather complex by design and expensive. One simple approach to avoid

contamination due to ambient exposure is by performing all deposition processing within a single chamber without breaking vacuum and potentially exposing film materials internal to the device to ambient environment. For multilayer film structures, this is best accomplished by integrating different film deposition techniques within a single chamber (20; 21; 22; 23; 24; 25; 26). A wide variety of deposition methods are used for different thin film applications. Atomic layer deposition (ALD) & chemical vapor deposition (CVD) methods are efficient methods for conformal films which are complementary to each other with advantages and limitations. ALD for example, has precise thickness and composition control along with superior conformality (27), whereas growth rate of ALD is typically an order of magnitude or two lower than that of other deposition techniques such as CVD or physical vapor deposition (PVD) (28; 29). Combining ALD & CVD in one reactor system enables faster film growth for thicker films along with precisely controlled thickness and composition for thinner films when performed by ALD. For example, ALD can be used to deposit ultra thin adhesion layers for a copper interconnect application followed by a thicker copper layer (25) by CVD for the Cu interconnect all without vacuum break in a single deposition chamber. This will ensure a pristine ALD/CVD interface, free from contaminants of the ambient environment. There are few reports on hybrid thin film deposition systems in the open literature. For example, Martin et al. (22) combined reactive magnetron sputtering and e-beam evaporation; Kala et al. (24) coupled nano-particle synthesis setup with thin film evaporation deposition setup to form nano-particle incorporated thin film structures. Zeng et al. (20) combined PVD and CVD to deposit superconducting  $\text{MgB}_2$  thin films. Reid et al. (21) used CVD and ALD in single deposition chamber to deposit high-k

dielectric films. Cheng et al. (26) used metal organic chemical vapor deposition (MOCVD) and ALD to deposit ALD of high-k oxide on MOCVD deposited III-V compound semiconductor without vacuum break. Mantovan et al. (23) used their customized ALD/CVD system to deposit magnetic tunnel junctions. Our group built a multi-material hybrid ALD/CVD reactor back in 2009 (30) and used this for CVD (31; 32) and ALD (33; 34; 35; 36) processes. All these papers used ALD/CVD hybrid apparatus for their respective application without discussing much about the system from equipment design point of view. This section is intended to cover these aspects including control design.

In this section, detailed descriptions are provided on the design and construction of precursor delivery system, oxidizer delivery system, UV-ozone generator, bubbler and control architecture of a portable ALD/CVD hybrid system. As a test of the system, ALD, CVD and ALD/CVD hybrid films are deposited using this novel reactor system offering ALD precise thickness and composition control along with faster film growth capabilities of CVD. The resulting films are appropriately characterized to prove the effectiveness of the designed system. The reactor design is particularly suited for depositing all components of thin film intermediate temperature solid oxide fuel cell structures using ALD and CVD within single deposition system without vacuum break.

### **2.1.2 System Description**

The ALD/CVD hybrid system is a flow-type reactor. Three major sections of the system, the deposition chamber, precursor delivery system and oxidizer delivery system are discussed in detail in the following section along with the precursor bubbler and ozone generator design.

#### **2.1.2.1 Deposition chamber**

The deposition chamber is a hot-wall, perpendicular-flow, aluminum chamber with optical diagnostic access. The chamber walls are heated by cartridge heaters and electrical heating tapes. The wafer stage is heated separately by two cartridge heaters located within the wafer stage, outside of the vacuum chamber. Detailed diagnostic flow analysis of the deposition chamber and computational flow analysis are reported elsewhere (37). The precursors are kept in stainless steel (SS) bubblers and transported to deposition chamber through heated stainless steel tubes. The temperature is measured using glass braid insulated type-K thermocouple having accuracy of 2.2 °C. The system temperature is controlled by a single 6-zone proportional-integral-derivative controller (CN616, Omega Engineering Inc.). The heating power controller consists of six solid state relays housed together in a grounded steel enclosure for portability. The reactor walls and delivery lines are heated 30 °C above precursor bubbler temperature to avoid precursor condensation. The wafer stage, delivery lines and precursor bubblers can be heated up to 450 °C. High purity nitrogen (99.998% purity) is used to carry precursor vapor from the bubbler to the deposition chamber and to purge precursor/oxidizer out of the deposition chamber. A two stage, oil sealed rotary vane pump (Edwards Vacuum Inc.) is used with zeolite fore line trap (13x10 Angstrom; 1/8 in. pellets; Kurt J. Lesker Company). The zeolite trap

prevents pump oil from back streaming into the deposition chamber as well as avoids precursors from getting into the pump. A manual ball valve is installed between the vacuum pump and the deposition chamber to isolate the deposition chamber during sample transfer and to regulate chamber pressure during deposition. A flexible, 1 m long, SS unbraided hose is used between pump and chamber to prevent pump vibration from reaching deposition chamber. The system has a base pressure of less than 40 mTorr and typically the ALD/CVD deposition is carried out at 500 mTorr. The deposition chamber is equipped with two pressure gauges covering the ranges of  $1 \times 10^{-3}$ -2 Torr range (Varian 801, Varian Inc.) and 1-760 Torr range (Series 902 Piezo transducer, MKS Instruments).

#### **2.1.2.2 Precursor delivery line**

Precursor delivery lines are carefully designed to accommodate ALD & CVD modes, minimize cost, improve compactness & facilitate portability. The system has two delivery lines with a common by-pass line. Each line has two bellow-sealed pneumatic valves (Model: SS-BNVV51-C, Swagelok) and two manual plug valves (Model: SS-4P4T, Swagelok) arranged as shown in Figure 2. Manual plug valves are used to protect air-sensitive precursor from coming in contact with air during precursor transfer. Oxidizer delivery is controlled by a 3-way bellow sealed switching valve (Model: SS-4BY-V35-1C, Swagelok). In ALD mode, valves V3&V4 for line A or V5&V6 for line B are opened momentarily, followed by precursor purging, oxidizer pulse and oxidizer purge steps in a cyclic manner. V1 valve in bypass line is opened for precursor purging and oxidizer purging steps, whereas V2 is opened for the oxidizer pulse step. For CVD mode, V3&V4 for line A or V5&V6 for line B are opened along with oxidizer valve V2

for a specified time. This valve configuration allows for both ALD and CVD deposition modes within a single delivery system configuration. A custom-designed LabVIEW computer control program with I/O voltage interface electromechanically controls a series of miniature valves (Model: ET-3-24, Clippard Instrument Laboratory, Inc.) which, in turn, controls  $N_2$  pressure to the pneumatic valves in the delivery lines. Thus, via computer command, the open/close sequencing of delivery valves is controlled for ALD or CVD operation which allows alternating between the two modes of operation thereby providing a more efficient means of synthesizing thick-thin (i.e., micro-nano) laminated film structures within a single hybrid processing chamber. All valves are bolted firmly on a 12x12 in. aluminum plate for rigidity; and mounted right on top of the deposition chamber for compactness. Deposition chamber, valve plates & control system parts are so arranged to minimize footprint & improve rigidity as shown in Figure 3.

#### **2.1.2.3 Oxidizer delivery line**

This system is capable of delivering pure oxygen, ozone/oxygen mixture or water vapor to the deposition chamber. Water vapor is delivered as wet nitrogen created by passing  $N_2$  over the head space of a water reservoir maintained at ice temperature. The dip tube within the water reservoir is deliberately cut to avoid nitrogen injection inside the water bath to reduce moisture content in the  $N_2$  without requiring additional dilution or heating-up of downstream delivery lines to prevent water vapor condensation (38). In this system, the open-ended dip tube was cut 1 in. above water level. This arrangement markedly reduced oxidizer purging time from 20 s to 10 s. (38) This oxidizer delivery line is connected with a proportional relief valve

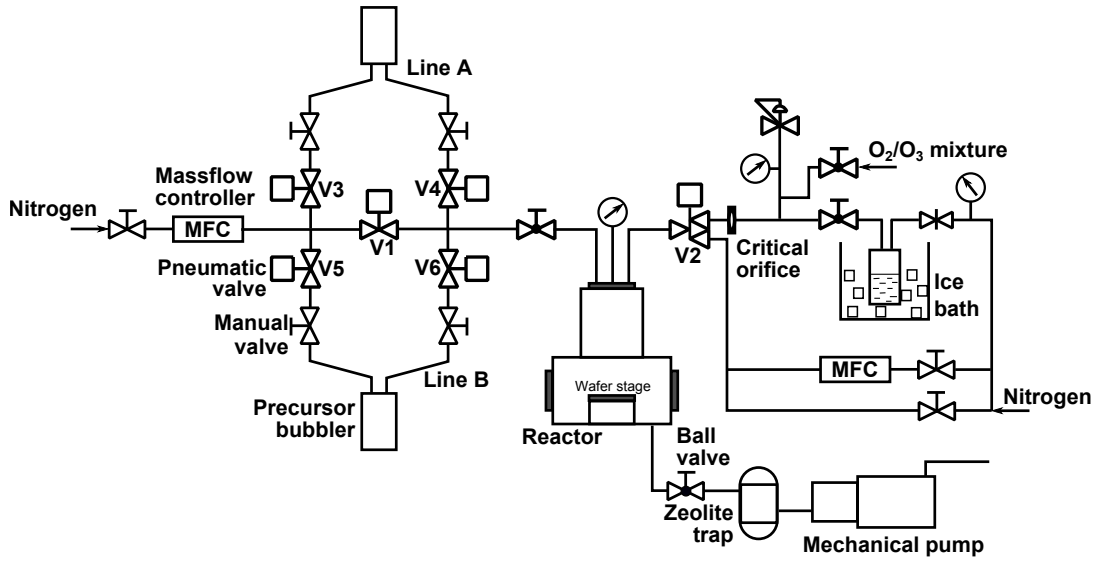


Figure 2: Schematic diagram of the ALD/CVD hybrid reactor system.

(Model: SS-RL3S4, Swagelok) and a pressure gauge to facilitate continuous stream of oxidizer at a set pressure (0.7 psi).

#### 2.1.2.4 Bubbler design

Most vapor deposition systems use heated-open boat to deliver solid/low-vapor pressure liquid precursors and passivated stainless steel bubblers for moderate to high vapor pressure liquids. In this study, continuous flow CVD-type bubblers (39) are used to accommodate ALD & CVD operating modes. The precursor bubbler components are fabricated from 316L stainless steel, assembled using combination of tungsten-inert gas (TIG) and CO<sub>2</sub> laser welding techniques. Conflat flanges with copper gasket are used to seal the bubbler reservoir to the top cap which has two Swagelok VCR fittings (1/4 in. diameter, Model: 6LV-4-VCR-3-4TB7) TIG

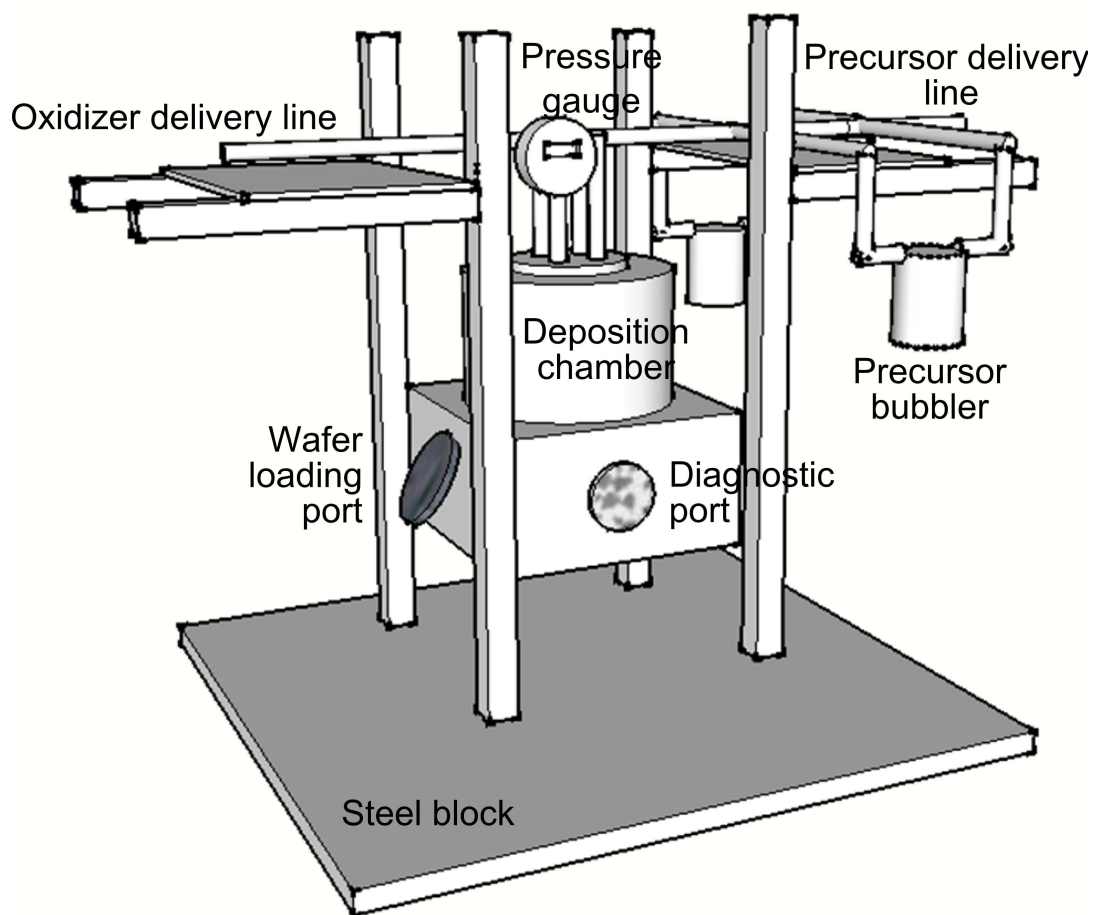


Figure 3: 3-Dimensional representation of the portable ALD/CVD system. (Only major components are shown).



welded onto the cap for gas in and out ports. The fittings on the cap have manual plug valves at each end. Two kinds of bubbler are used, one with dip tube for most liquid precursors and another without dip tube (sublimator) for solid precursors or very high vapor pressure liquid precursors like dimethyl zinc (33). Wetted areas of the bubbler are electropolished internally and externally to minimize potential surface reactions and outgassing with the precursor. After electropolishing, the bubblers were sonicated in organic solvents (Methanol and Acetone) and baked at 200 °C overnight before loading the precursor into the bubbler.

#### **2.1.2.5 Ozone generator**

Ozone is commonly produced by two methods: corona discharge and UV lamp illumination. In corona discharge, an electric discharge split oxygen molecules within the discharge region and form ozone. Alternatively, an UV lamp that emits light in the far UV region ( $\sim 185$  nm) can produce ozone by photolysis of oxygen molecules (40). Although corona discharge produces a high concentration of ozone, a UV lamp produces more uniform concentration over long period of time which is preferred for this study. An important aspect of ozone generator design is the selection of sealing material, as even low level of ozone leak can also be harmful to respiratory tract and lungs (41). Ozone being a strong oxidizer affects O-rings used for sealing. Viton, Kalrez & Teflon O-rings are reported to be more resistant to ozone attack (42). Viton O-rings coated with a thin layer of Fomblin high vacuum grease is used in this system. A 25 Watt UV germicidal lamp (Model: G24T5VH/U, Atlantic Ultraviolet Corporation) is used with suitable lamp holder and ballast. The lamp is housed within a 2.5 in. diameter aluminum cylinder with gas inlet and outlet ports. A four-pin, O-ring sealed power feedthrough is used to route the

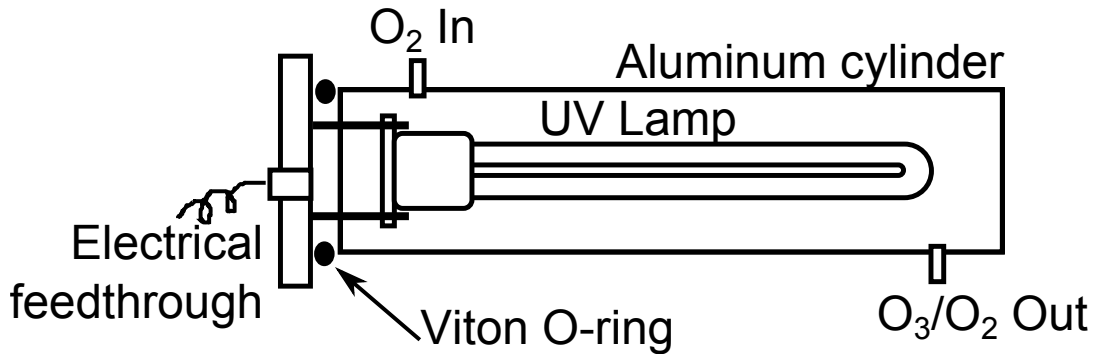


Figure 4: Schematic diagram of homemade UV-ozone generator.

power cables of UV lamp through cylinder cap. Schematic diagram of our homemade UV-ozone generator is shown in Figure 4. The generator is placed immediately upstream of the deposition chamber to reduce ozone decomposition in delivery line. With pure oxygen (99.999 % purity) at 0.7 psi as inlet gas, our custom-built ozone generator produces about 1000 ppm of ozone, as measured with an ozone analyzer (Model 450, Advanced Pollution Inc.).

### 2.1.3 Control System Implementation

This section describes a simple way to write LabVIEW program to control ALD mode of operation in a single delivery line ALD/CVD hybrid system. LabVIEW (Version 11.0.1) block diagram of the program is shown in Figure 5(a). This program takes number of ALD cycles ( $N_c$ ), precursor pulse time, precursor purge time, oxidizer pulse and oxidizer purge times as input, and controls the four pneumatic valves (V1-V4) located at precursor and oxidizer delivery lines. Valve position (True/False) for all four ALD sub-cycles are stored in 'ALD Recipe' block in the form of 2-dimensional (2-D) array of Boolean constants. This 2-D array is then fed to

'Index Array-1' (IA-1) block. 'Build Array' block build 1-dimensional array of sub-cycle times and feed it to 'IA-3'. 'IA' block returns the element or sub-array of n-dimension array at the supplied index number. This index number (0-3) is supplied by 'Quotient & Remainder' block to IA-1 and IA-3, thus combining valve positions for a particular sub-cycle with its corresponding sub-cycle time. This valve position information is then send to Boolean indicators and 'Data Acquisition' module (not shown) that communicates with valve-hardware; whereas, sub-cycle time is send to 'Wait (ms)' block, that halts the LabVIEW program in the same valve positions for the specified sub-cycle time before switching to the next sub-cycle valve positions. The entire process repeats  $4 \times N_c$  times in loop to cover all four ALD sub-cycles for  $N_c$  number of times. The ALD program described here is, however, a simplified version of the actual program, that has few extra recipes (Figure 5(b)) to include 'wait time before deposition' and second precursor line.

#### **2.1.4 Experimental Verification**

The ALD mode of reactor operation was demonstrated with ALD of  $\text{TiO}_2$  using tetrakis (diethylamino) titanium (TDEAT) and water vapor. Deposition was carried out on highly doped p-type Si(100) substrates (resistivity 1-10  $\Omega\text{-cm}$ ) cut into 2 x 2 cm pieces. Radio Corporation of America standard cleaning (RCA SC-1) procedure was followed to clean the substrate prior to deposition. Deionized water (resistivity  $\geq 17 \text{ M}\Omega\text{-cm}$ ) and nitrogen was used to clean the substrate after every RCA step. Substrates were loaded immediately after cleaning. Figure 6 shows the effect of precursor pulse duration on growth rate of  $\text{TiO}_2$  films deposited at 200 °C with 1 s oxidizer pulse. Precursor and oxidizer purging times were optimally fixed at 15 s and



Figure 5: (a) LabVIEW block diagram for ALD mode in a single delivery line ALD/CVD hybrid system. (b) ALD Recipe for ALD/CVD system with two delivery lines.

10 s respectively, after ensuring no change in growth rate with further increase. The TDEAT bubbler temperature was kept constant at 65 °C. With increasing precursor pulse duration to 2 s, the film growth rate increases to 0.04 nm/cycle; no further increase in the growth rate was observed for longer precursor pulse durations beyond 2 s. This confirms the characteristic self-limiting growth behavior of ALD. Film growth rate was relatively insensitive to changes in oxidizer pulse time tested from 50 ms to 2 s (Figure 7). The TiO<sub>2</sub> film growth rate dependence on reactor temperature is shown in Figure 8; it is found to be independent of reactor temperature between 150 and 275 °C, indicating adsorption controlled growth regime. Figure 9 shows the film thickness measured after different number of ALD cycles. Good linearity demonstrates

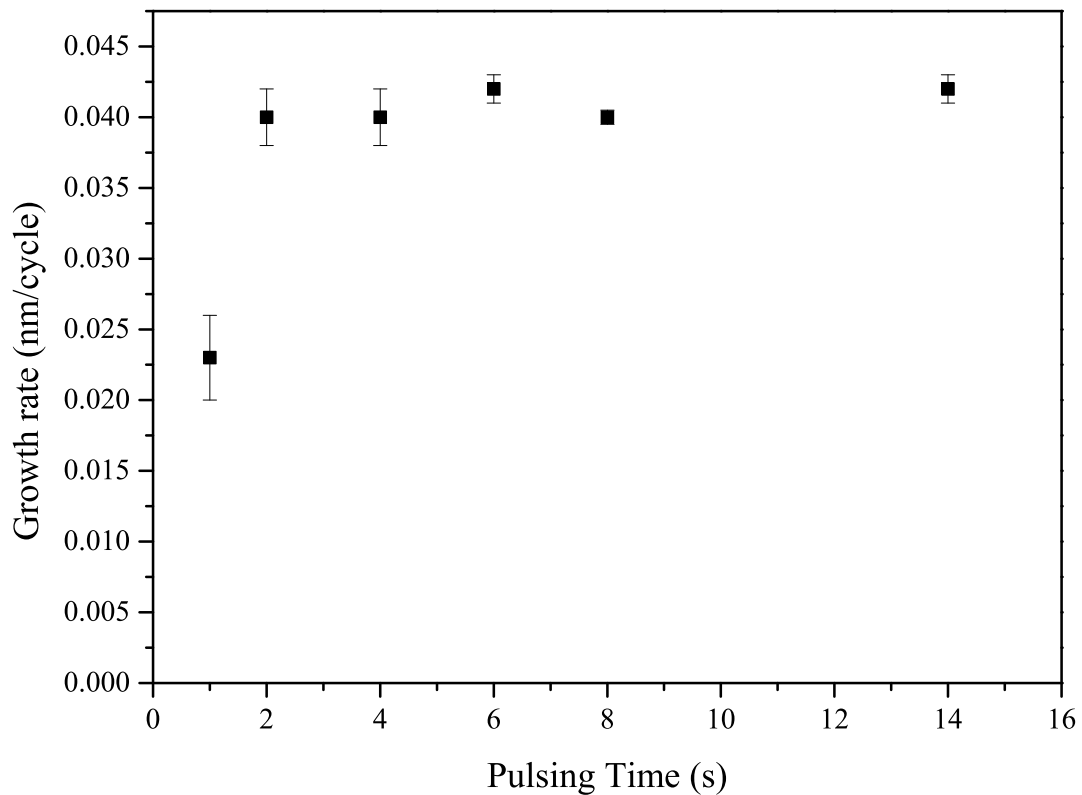


Figure 6: Effect of precursor pulse time on  $\text{TiO}_2$  ALD growth rate at 200 °C substrate temperature. The bubbler temperature was at 65 °C. The system pressure was 0.5 Torr. The vertical error bars indicate film uniformity across the sample.

the thickness tunability with this reactor. The  $\text{TiO}_2$  ALD growth rate is in good agreement with reported values in the literature (43).

The composition of ALD  $\text{TiO}_2$  films were probed with high resolution X-ray Photoelectron Spectroscopy (XPS) (Kratos AXIS-165, Kratos Analytical Ltd.) equipped with a monochromatic  $\text{Al K}\alpha$  (1486.6 eV) X-ray source operating at 15 kV and 10 mA. Spectra were taken after sputtering the surface using  $\sim 100$  nA  $\text{Ar}^+$  beam for 20 min. Survey spectrum of 30 nm-thick

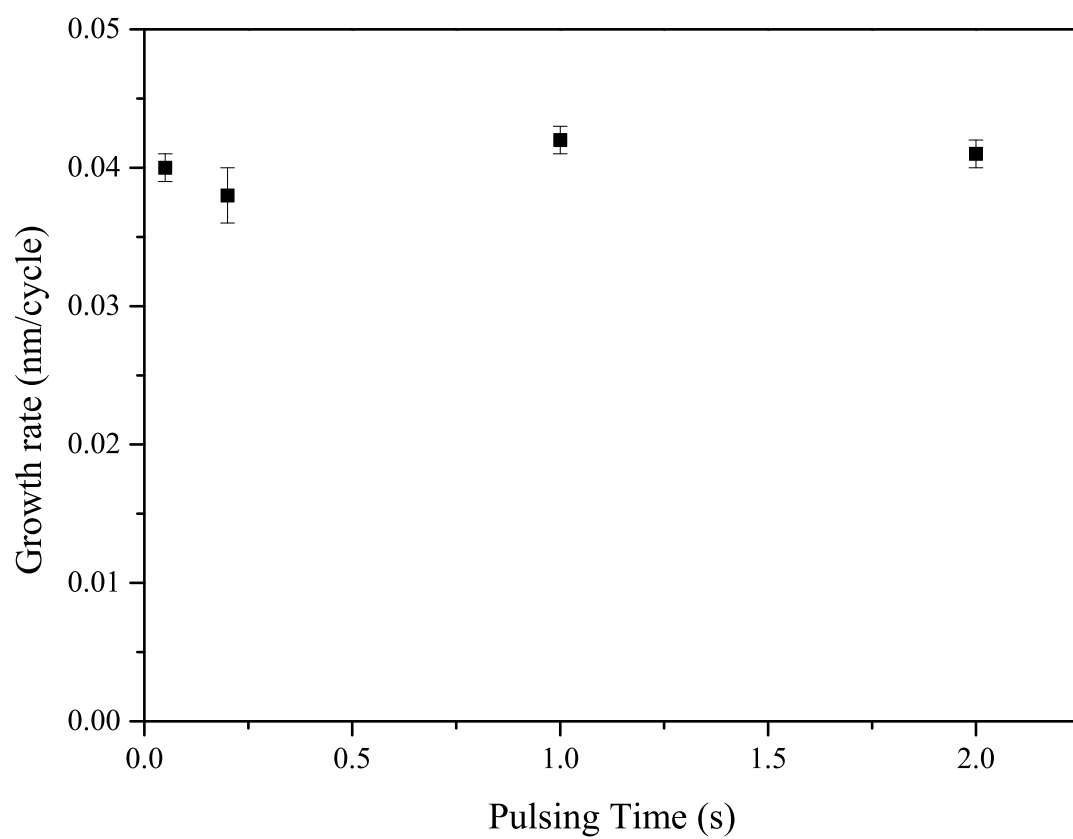


Figure 7: Effect of oxidizer (water vapor) pulse time on  $\text{TiO}_2$  ALD growth rate. All ALD conditions are the same as those in Figure 6.

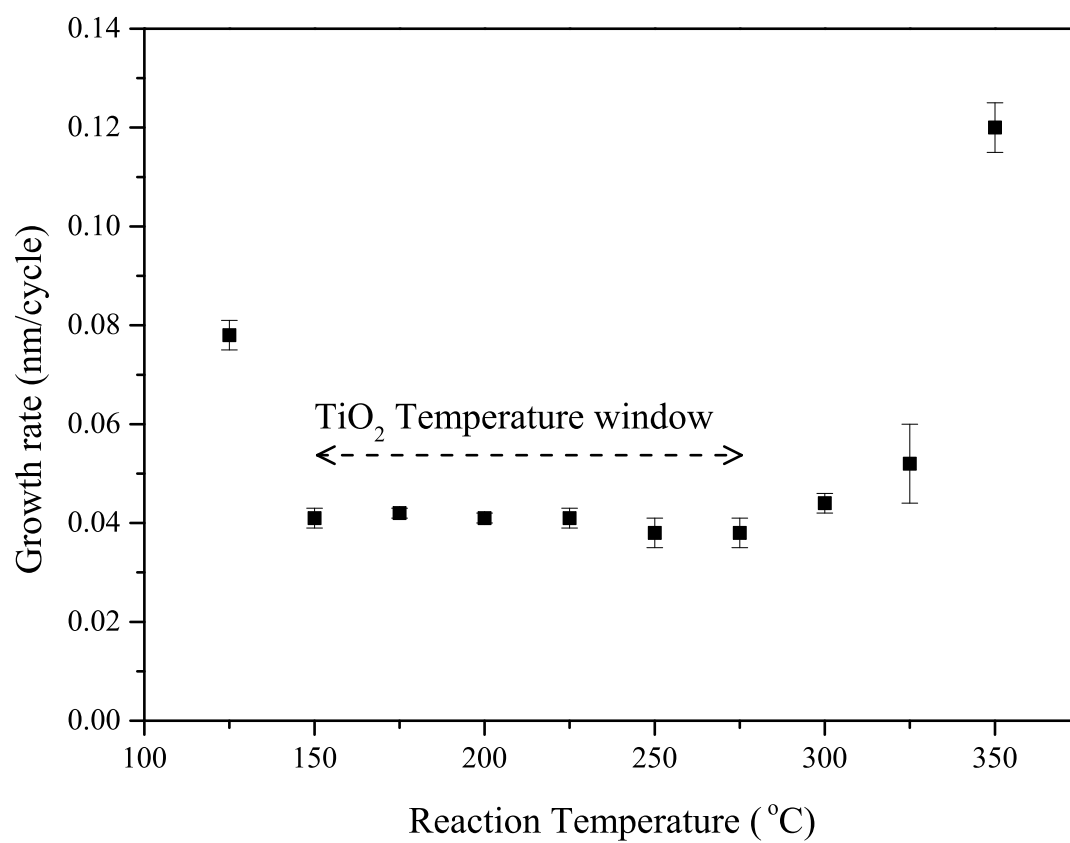


Figure 8: TiO<sub>2</sub> ALD growth rate as a function of reactor temperature. Other conditions are the same as in Figure 6.

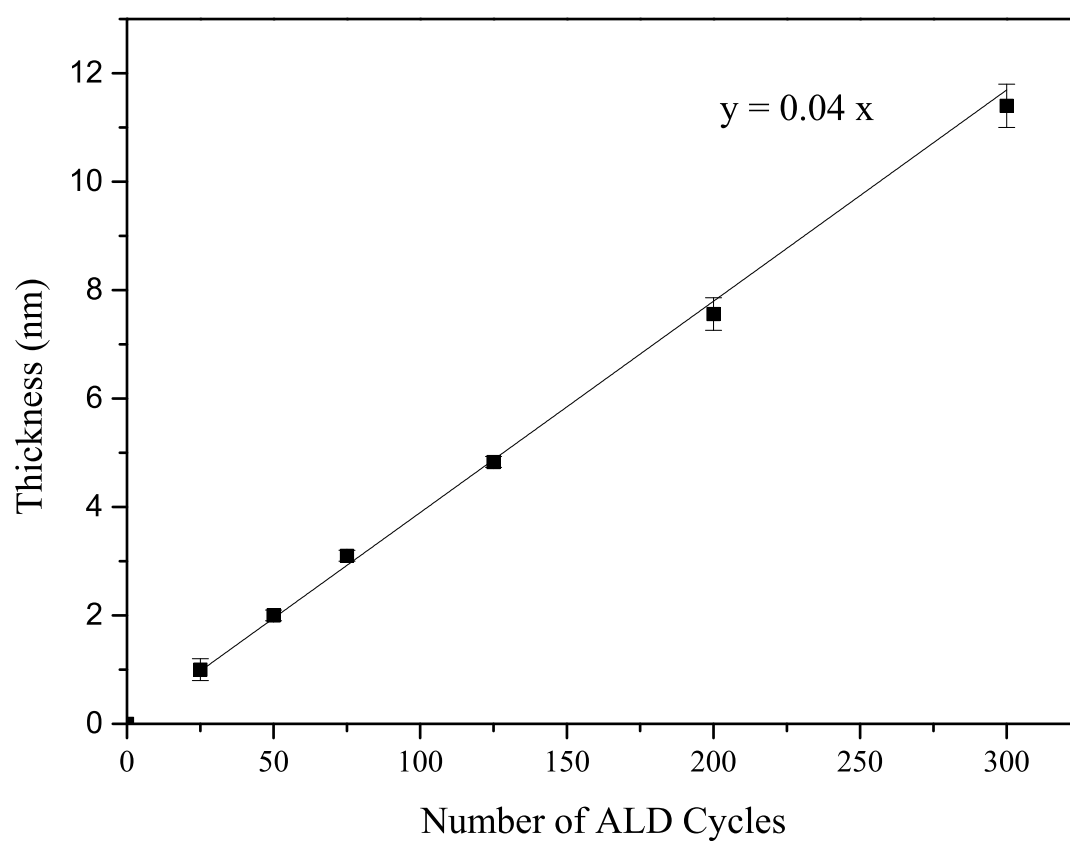


Figure 9: TiO<sub>2</sub> ALD growth rate as a function of number of ALD cycles. The substrate was at 200 °C. The growth rate is constant at 0.04 nm/cycle.



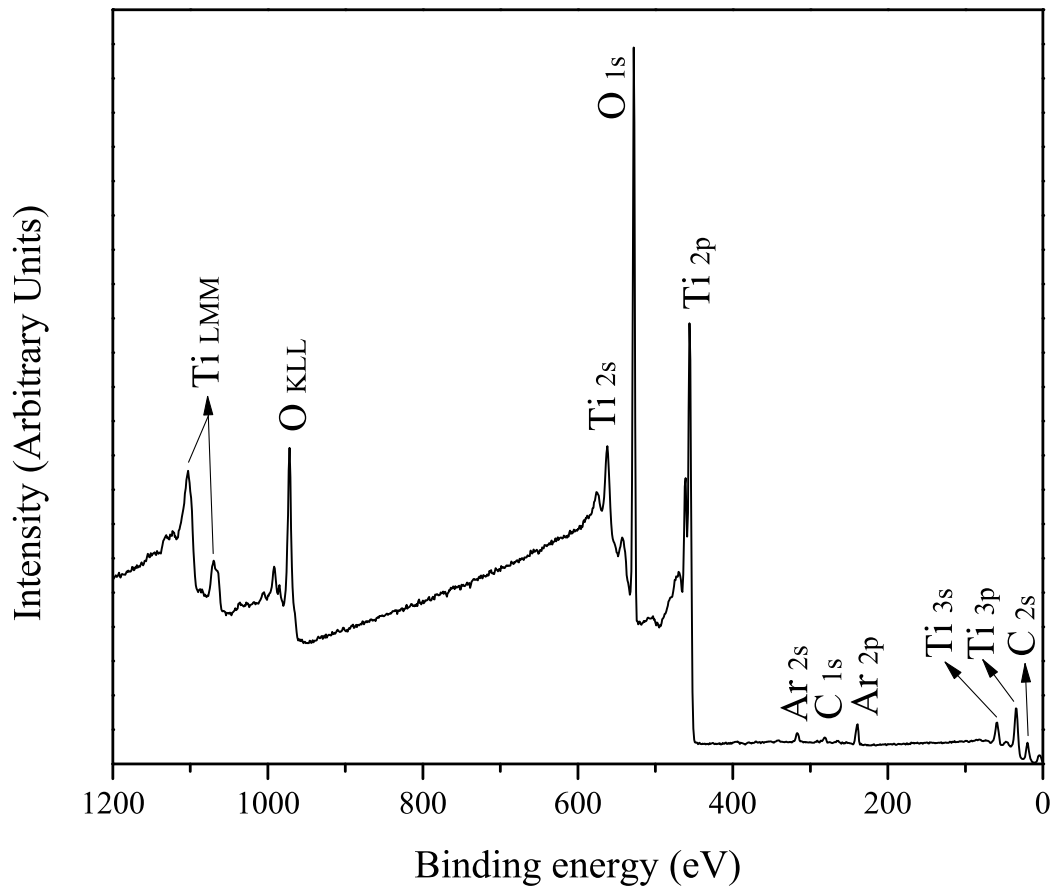


Figure 10: XPS spectra for atomic layer deposited 30 nm-thick  $\text{TiO}_2$  at 200 °C substrate temperature with TDEAT and water.

film (Figure 10) shows stoichiometric titanium oxide ( $\text{Ti} \sim 32$  atom %;  $\text{O} \sim 66$  atom %) with a trace amount of carbon ( $\sim 2$  atom %) and argon. Argon in the film most likely came from the  $\text{Ar}^+$  beam sputtering, and it is omitted from elemental analysis.

The CVD mode of the reactor with similar delivery system has been used and reported earlier from our group (31; 32). A few CVD experiments were conducted with this reactor setup to

probe the growth rate of  $\text{SnO}_x$  CVD using tin(II)acetylacetonate and ozone at 250 °C reactor temperature and 70 °C precursor bubbler temperature. The growth rate was found to be 0.7 nm/min, which is about half of the value reported with the same precursor but with a different reactor system having an order of magnitude higher gas flowrate than our system (44). The ALD/CVD hybrid mode was demonstrated using ALD of  $\text{TiO}_2$  and CVD of  $\text{SnO}_x$  at 250 °C. A prolonged 5 min  $\text{N}_2$  purging was performed when changing from ALD mode to CVD mode or vica versa to avoid memory effects. This purging time is an order of magnitude higher than the purging time we use for ALD of  $\text{TiO}_2$  and  $\text{SnO}_x$  in the same system. Thus cross contamination between titanium and tin was avoided/minimized. It is to be noted that this system has two purging lines, precursor purging line (also called bypass line) and oxidizer purging line (through 3-way switching valve) to ensure complete purging of remaining precursor and oxidizer out of deposition chamber. A low magnification transmission electron microscopy (TEM) image of as-deposited ALD- $\text{TiO}_2$ /CVD- $\text{SnO}_x$  is shown in Figure 11. Distinct layers of ALD and CVD are observed. The thickness of layers are measured to be  $\sim 108$  nm CVD- $\text{SnO}_x$  : 10 nm ALD- $\text{TiO}_2$  : 82 nm CVD- $\text{SnO}_x$  : 11 nm ALD- $\text{TiO}_2$  which corresponds to 150 min of CVD- $\text{SnO}_x$  : 150 cycles of ALD- $\text{TiO}_2$  : 150 min of CVD- $\text{SnO}_x$  : 150 cycles of ALD- $\text{TiO}_2$ . The reduced thickness in the first CVD- $\text{SnO}_x$  layer may be due to possible phase change from prolonged exposure ( $\sim 4$  hrs more than the second CVD- $\text{SnO}_x$ .layer) to 250 °C during the deposition of top layers. Fortunato et al. (45) reported phase change in tin oxide films when exposed to temperature as low as 200 °C for 1 hr. Njoroge et al. (46) reported upto 9% increase in density when annealed at 280 °C for  $\text{Ge}_2\text{Sb}_{2.04}\text{Te}_{4.74}$  films. All these, along with darker first CVD- $\text{SnO}_x$  layer in TEM

image, suggest that phase change lead to tighter packing thereby lowered thickness of the first CVD-SnO<sub>x</sub> layer. The 2 nm-thick bright layer between silicon substrate and ALD-TiO<sub>2</sub> layer is most likely a silicon oxide layer. These experiments and characterization results show successful deposition of ALD, CVD & ALD/CVD hybrid layers using this reactor.

### **2.1.5 Summary**

A portable ALD/CVD hybrid reactor setup is described and successfully tested with ALD of TiO<sub>2</sub>, CVD of SnO<sub>x</sub> and ALD-TiO<sub>2</sub>/CVD-SnO<sub>x</sub> hybrid film depositions. TiO<sub>2</sub> ALD results demonstrate thickness tunability of the reactor for ALD deposition. The resultant film was analyzed with XPS and found to be stoichiometric TiO<sub>2</sub> with a trace amount of carbon. ALD rate and film purity are in good agreement with literature values. Deposition of ALD-TiO<sub>2</sub>/CVD-SnO<sub>x</sub> hybrid films proved the ability of the reactor to deposit thick-thin nano-laminate structures without vacuum break; TEM confirmed the distinct ALD and CVD layers. Changes in vapor delivery system & control architecture of conventional vapor deposition system paved the way to accommodate ALD & CVD modes of operation in a single portable deposition system.

## **2.2 Scalable control program for ALD/CVD hybrid reactor**

This section was previously published as "Scalable control program for multi-precursor flow-type atomic layer deposition system" in Journal of Vacuum Science & Technology A.

### **2.2.1 Introduction**

ALD is a relatively nascent thin film deposition technique developed by Tuomo Suntola in the 1970s for electroluminescent display coating application. (47) ALD is now widely accepted in many industries. Most of these applications demand deposition of more than one material

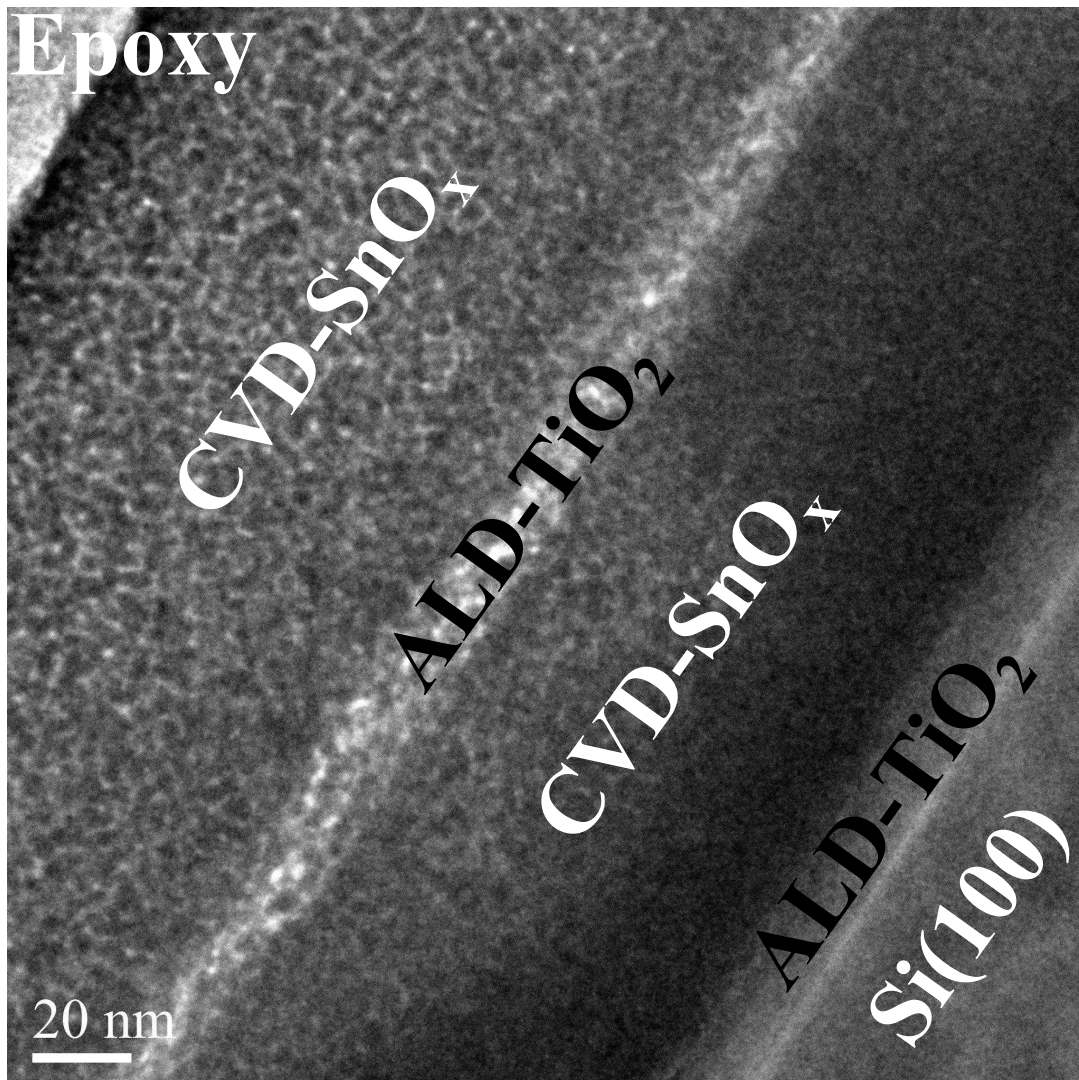


Figure 11: Low magnification TEM image of as-deposited ALD-TiO<sub>2</sub>/CVD-SnO<sub>x</sub> hybrid film deposited at 250 °C substrate temperature.

in the form of nanolaminates or mixed materials, such as ternary oxides for amorphous high dielectric constant layers (35; 48) and diffusion barriers, (49) quaternary metal oxides for fuel cell electrode applications, (50) and quaternary metal sulfides for photovoltaic applications, (51) to name a few. ALD of such complex multilayered and mixed materials require sophisticated control systems to carry out precisely timed operations of numerous control valves in the ALD system. The ALD reactors are normally controlled by computer programs; one such program to control a single precursor line flow-type ALD reactor was briefly described in the previous section. (1)

In this section, we report the development of a scalable control program to control multi-precursor flow-type ALD reactor. The program described here can be used to deposit up to four different layers of materials in cyclic manner from the available four-precursor combination. The programing logic implemented in LabVIEW (version 13.0), is fairly general and can be applied in any similar control program software to effectively control ALD reactor systems. The programming logic is so written to facilitate easy scale up and down in terms of number of precursors and number of layers used in the ALD process. In the first part of the section, the ALD process principle and reactor operation are explained briefly, followed by the description of the control program and its scalability aspects in the second part.

### **2.2.2 ALD Reactor Operation**

Figure 12 shows schematic representation of the flow-type ALD reactor system with four precursor delivery lines and one oxidizer delivery line. (36) Each precursor delivery line has three pneumatic valves. These open sequentially to allow either precursor laden carrier gas

during precursor pulse sub-cycle or just the carrier gas during the purging sub-cycle. For instance, to grow film using precursor-A, its delivery line valves V1 and V2 opens up during the precursor-pulsing sub-cycle, followed by the opening of V3 to purge excess precursor, V13 to pulse oxidizer, V3 again to purge excess oxidizer in sequential and cyclic manner until the required film thickness is reached. For precursors that need to be operated without carrier gas, the same ALD reactor configuration can be used after closing the upstream mass flow controller and manual plug valve located at inlet side of the precursor bubbler. The valve status (T-Open & F-Close) of different sub-cycles for the ALD using precursor A is shown in Figure 13. This valve status is same for precursor delivery lines that operate with and without carrier gas. For programming purposes, a new sub-cycle called stand-by is introduced prior to precursor pulsing sub-cycle. This sub-cycle opens up bypass line valve to stabilize gas-pressure during the start of deposition and when shifting between precursor-lines. These critically timed valve sequencing is realized using the computer control program described in detail in the following sections.

### **2.2.3 Control Program Operation**

The front panel of the control program is shown in Figure 14. It has four layers numbered from 1 to 4. A layer here is defined as the film or part of the film deposited using a single precursor line. Each layer has a drop-down list to select the precursor to use. None option in the drop-down list is used to disable a layer. During each cycle, the program scans all four layers and its ratios in sequence. If, for example, Layer 1 has Precursor B with ratio 2, Layer 2 has Precursor D with ratio 5 and rest of the Layers has None option selected. Then the program will start with 2 ALD cycles using precursor B followed by 5 ALD cycles using precursor D

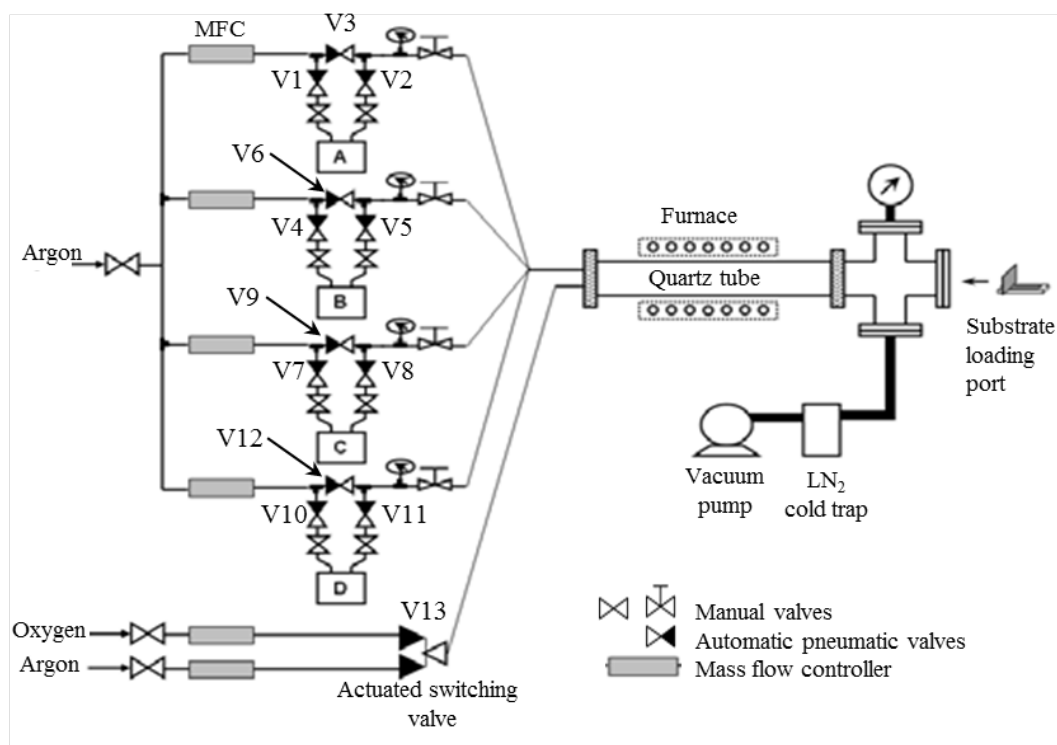


Figure 12: Schematic representation of flow-type ALD system with four precursor delivery lines named A, B, C and D. More precursor lines can be added without affecting the overall system design and control program logic.

	V1	V2	V3	V13
Wait	F	F	T	F
Cycle 1:Standby	F	F	T	F
Cycle 1:P <sub>Pulse</sub>	T	T	F	F
Cycle 1:P <sub>Purge</sub>	F	F	T	F
Cycle 1:O <sub>Pulse</sub>	F	F	F	T
Cycle 1:O <sub>Purge</sub>	F	F	T	F
Cycle 2:Standby	F	F	T	F
Cycle 2:P <sub>Pulse</sub>	T	T	F	F
Cycle 2:P <sub>Purge</sub>	F	F	T	F
Final cycle:O <sub>Purge</sub>	F	F	T	F
End	F	F	F	F

Figure 13: Valve status (T-Open & F-Close) for different sub-cycles during ALD using precursor delivery line-A. Valve number V1-3 and V13 are indicated in Figure 12.



## ALD Control Program

**Super-cycle number**  **Wait before deposition**

STOP

**Total Deposition Time**  
06:17:40

**Time Remaining**  
06:17:40

**Time Elapsed**  
0 00:00:00

**Valve Status**

**Precursor A:** In ☐ Out ☐ Bypass ☐

**Precursor B:** In ☐ Out ☐ Bypass ☒

**Precursor C:** In ☐ Out ☐ Bypass ☐

**Precursor D:** In ☐ Out ☐ Bypass ☐

**Oxidizer valve** ☐

	LAYER 1	LAYER 2	LAYER 3	LAYER 4
<b>Line</b>	Line B	Line D	None	None
<b>Ratio</b>	2	5	0	0
<b>Standby</b>	5	5	0	0
<b>P_pulse</b>	2	3	0	0
<b>P_purge</b>	10	15	0	0
<b>O_pulse</b>	1	1	0	0
<b>O_purge</b>	10	10	0	0

Figure 14: Front panel of the ALD control program. All input parameters are grouped on left boxes. The right side box shows valve status and the deposition times.

and count it as one super-cycle. Before starting the ALD super-cycle, the program keeps the bypass valve of the first Layer precursor line open to stabilize the gas pressure in the line, for the duration of time specified in Wait before deposition box. All the valves are closed either after the end of all ALD cycles or when the stop button is pressed. The stop button is used to abort the deposition at any time during ALD operation. The basic program operation is algorithmically represented in Figure 15.

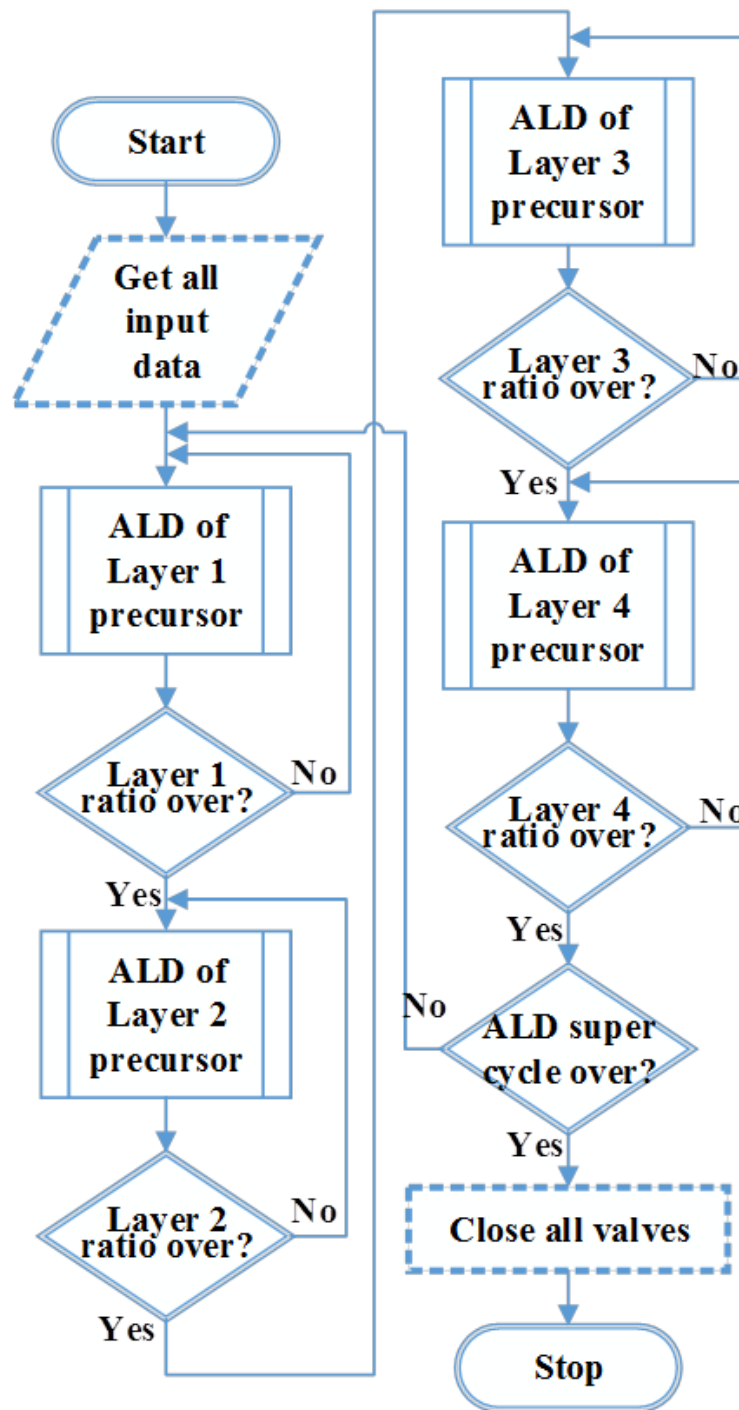


Figure 15: Algorithmic representation of the basic program operation and flow. Four layers are shown here, which can be scaled down or up.

#### 2.2.4 Master Program

LabVIEW block diagram of the ALD control program (VI-Virtual Instruments) is shown in Figure 16. This master program uses the functionality of six sub-programs (sub-VI) to control the ALD process. It takes super-cycle number (N), layer ratios (R1-R4), layer times and layer precursors as input and controls the operation of the 13 valves in the ALD system; first 12 of which corresponds to four precursor delivery lines (3 valves for each line) and the 13th one for the oxidizer line valve, as numbered in Figure 12. ALD Sub-Cycle Recipe sub-VI snatches the appropriate sub-cycle recipe of valve positions (1-dimensional array of four boolean constants) from the user-defined ALD Recipe(2-D array of boolean constants) and returns to the ALD Ratio Selector sub-VI. This sub-VI assigns the sub-cycle recipe to a particular layer and closes all valves in other layers. This decision is taken using the inputs from ALD Cycle Ratio Index sub-VI. Now, that the sub-cycle recipe is assigned to a particular layer, ALD Precursor Selector sub-VI chooses the precursor to use for this layer. Valve status is assigned for that particular precursor line and valves in other precursor lines are closed. These valves status is fed to the instrument interface that opens/closes pneumatic valves using miniature solenoids. In the meantime, ALD Cycle Clock tells the program to halt at the particular valve position for specified sub-cycle time. Thus the particular sub-cycle valve position is retained for its corresponding sub-cycle time. Also, the ALD Time sub-VI calculates total deposition time, time elapsed and remaining time. This entire operation is housed inside a loop, which repeats the process for  $N \times (R1 + R2 + R3 + R4) \times 5 + 1$  times. Thus all sub-cycles are achieved for

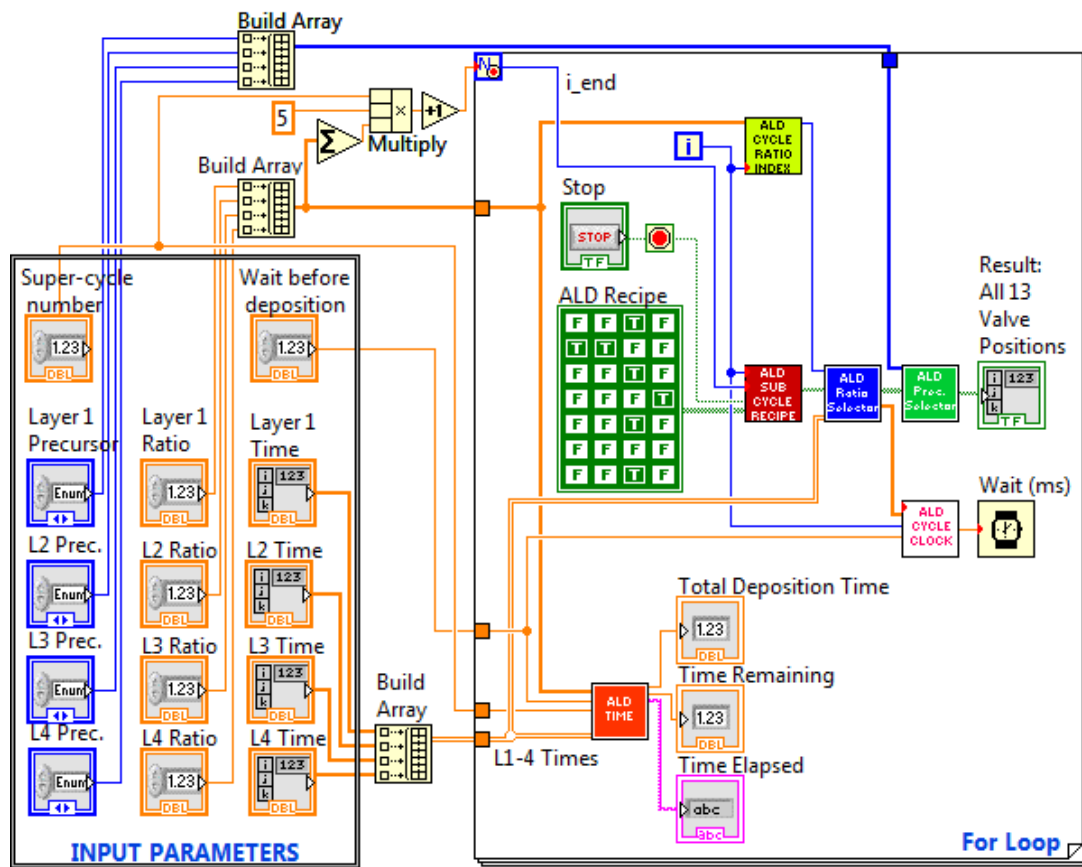


Figure 16: LabVIEW block diagram of the ALD program. The program consists of six custom-written sub-VI programs.

the specified number of times. The six sub-VIs used in this master program is explained in the following section.

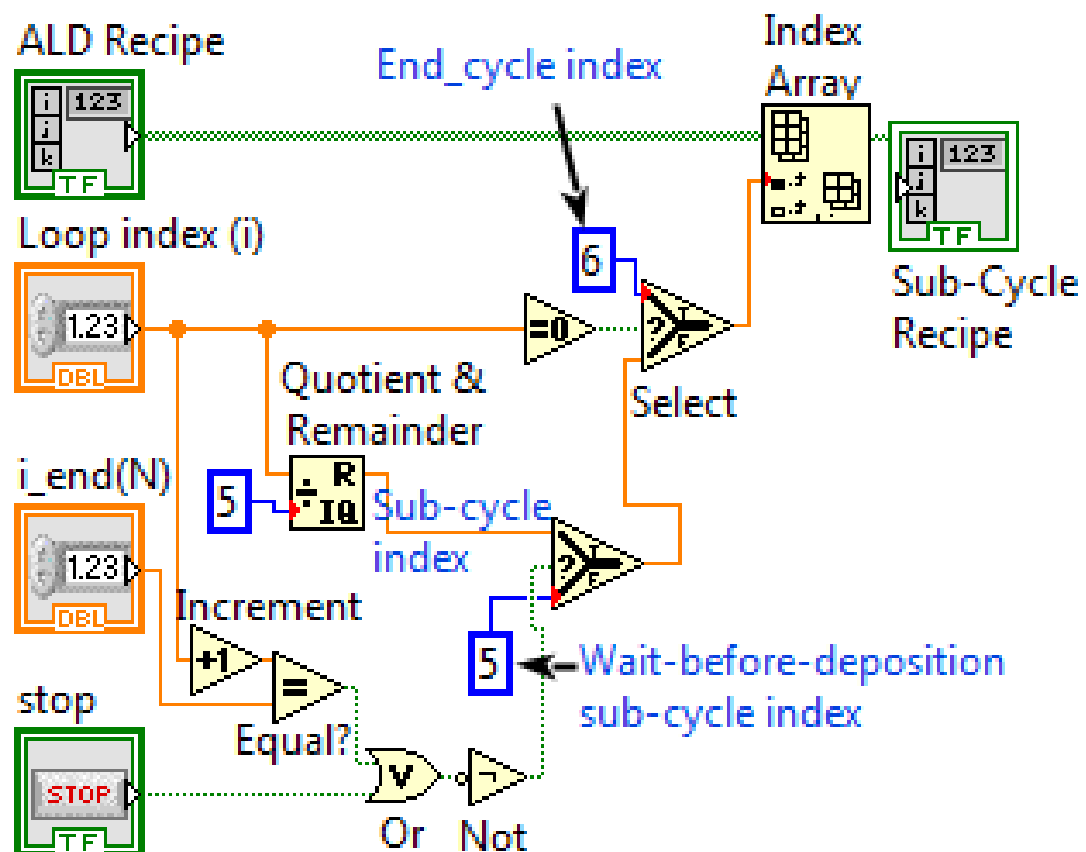
### **2.2.5 Sub-VI programs**

#### **2.2.5.1 Sub-VI: ALD Sub Cycle Recipe**

The sub-VI shown in Figure 17, supplies valve positions of each sub-cycle from ALD Recipe. ALD Recipe is a user defined recipe of valve positions for different sub-cycles. It is a 2D array of boolean constants. The sub-VI calculates the current sub-cycle index number from the loop iteration index number (i) by dividing it by 5 (total number of sub-cycles per ALD cycle). The remainder (0 to 4) gives the current sub-cycle index. This index is used to select sub-cycle recipe. Thus, the sub-VI returns sub-cycle recipe in the form of 1-D array of four boolean constants. When the loop index number (i) equals to zero, the sub-VI returns the 7th row of the ALD recipe, i.e. FFTF, for wait before deposition sub-cycle. Then it proceeds to the ALD cycles. After the end of all ALD cycles or when the Stop button in the front panel is pressed, the sub VI returns FFFF, to close all the valves.

#### **2.2.5.2 Sub-VI: ALD Cycle Ratio Index**

This sub-VI (Figure 18) supplies Ratio Index number which is used to decide on which layer to deposit during a particular cycle. The program uses the remainder of current cycle number divided by the sum of all ratios to take this decision. If the remainder is between 0 and R1, the sub-VI return 1000, which then converted to integer number (1) using the Boolean array to Integer function. This will tell the program to keep depositing Layer 1 until the remainder goes above R1. If the remainder is between R1 & R1+R2, R1+R2 & R1+R2+R3 or R1+R2+R3 & R1+R2+R3+R4 it returns 0100 (2), 0010 (4) or 0001 (8) and deposit Layer 2, 3 or 4, respectively. The same process can be extrapolated when more than four layers are desired.



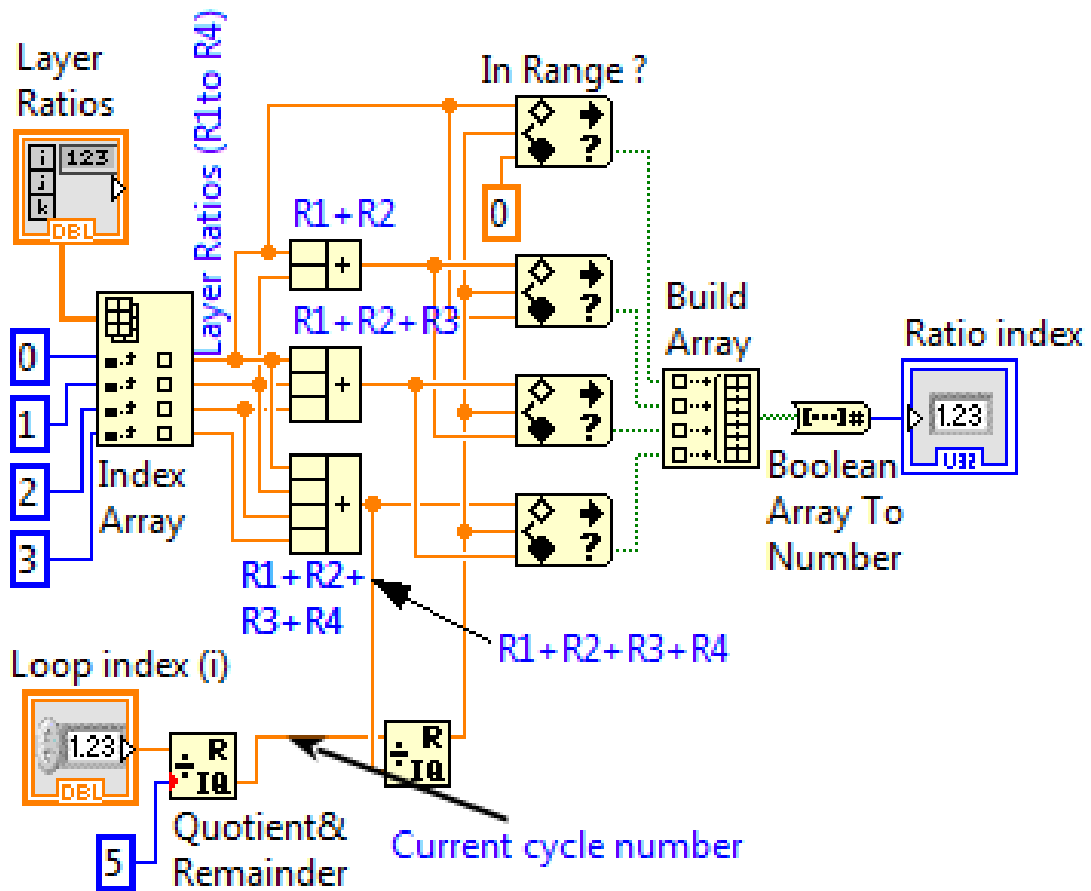


Figure 18: LabVIEW block diagram of the ALD Cycle Ratio Index Sub VI. It returns Ratio-index number to ALD Ratio Selector sub-VI.

This ratio index number (1, 2, 4 or 8) is passed on to ALD Ratio Selector sub-VI to select the layer to deposit for the particular ALD cycle.

#### 2.2.5.3 Sub-VI: ALD Ratio Selector

This sub-VI in Figure 19, uses a case structure with four cases to assign sub-cycle recipe to each layer based on the input from ALD Cycle Ratio Index sub-VI. Also, the sub-VI returns

layer times to ALD Cycle Clock. The four cases in this sub-VI are named after the ratio index numbers 1, 2, 4 and 8. The case is selected based on the index that ALD Cycle Ratio Index returns. If the index value is 1, case 1 is selected in which the sub-cycle recipe is wired to Layer 1 along with its corresponding Layer 1 sub-cycle times. And rest of the layer valves are turned off deliberately. In the second case, the sub-cycle recipe and time is connected to Layer 2 and so on. The number of cases in this sub-VI's case structure is equal to the number of Layers, thus the cases has to be increased accordingly to use more than four layers. Sub-cycle time is passed on to ALD Cycle Clock sub-VI and sub-cycle recipe is sent to ALD Precursor Selector sub-VI.

#### **2.2.5.4    Sub-VI: ALD Precursor Selector**

This sub-VI is used to define which precursor to use in each layer (Figure 20). It has four case structures to represent four layers. Each case structure has five cases, four for the four precursors and the None option. The number of case structures has to be increased for increase in number of Layers beyond four and number of cases in each case structure should be increased if more than four precursor lines are added to the ALD system. The drop-down list in the Front Panel is used to choose the precursors for each layer. The incoming sub-cycle ALD recipe in the form of 1-D array of four boolean constants is split into two, with first three elements getting inserted in different places in the 1x13 element boolean 1-D array, based on the precursor selection. The first 3 boolean constants in ALD recipe is inserted at first 3 spots in the 1x13 1-D array if precursor-A is chosen for that layer, and spots 4-6 for precursor-B, spots 7-9 for precursor-C and spots 10-12 for precursor-D. The 13th spot in this array is filled



Figure 19: Sub VI: ALD Ratio Selector. It assigns sub-cycle recipe to the active layer and closes all other valves. Also it passes the corresponding sub-cycle times to ALD Cycle Clock sub-VI.

by the 4th boolean constant in the sub-cycle recipe, which corresponds to oxidizer valve. The resultant 1x13 array from all four Layers case structure is combined and used to control the 13 valves as numbered in Figure 12. The size of the 1x13 boolean 1-D array should be increased for any increase in number of precursor delivery lines beyond four.

#### **2.2.5.5    Sub-VI: ALD Cycle Clock**

ALD Cycle Clock sub-VI (Figure 21) is used to halt the valve positions of a particular sub-cycle for its corresponding sub-cycle time. The function takes loop index (i), and sub-cycle times as input and returns appropriate wait time. The program calculates current sub-cycle number using the method explained in Section 2.2.5.1 and use this as the index to get appropriate wait time from sub-cycle time array. This value is sent to the Wait function, which pauses the Loop iteration for the specified time; thus maintains the same valve position for that period of time. At the start of the program, when loop index number (i) is equal to zero, the program returns wait before deposition time as the output to the Wait function.

#### **2.2.5.6    Sub-VI: ALD Time**

This sub-VI (Figure 22) is used to calculate total deposition time, time elapsed since the start of the deposition, and the remaining time. Time required to complete one super-cycle is calculated by adding all 5 sub-cycle durations and multiplying it with its corresponding layer ratio of each layer. These when multiplied with super-cycle number and added four layers together, gives the total deposition time. Remaining time is calculated by subtracting the elapsed time from the total deposition time. Elapsed time is obtained from the LabVIEW inbuilt function Elapsed time.

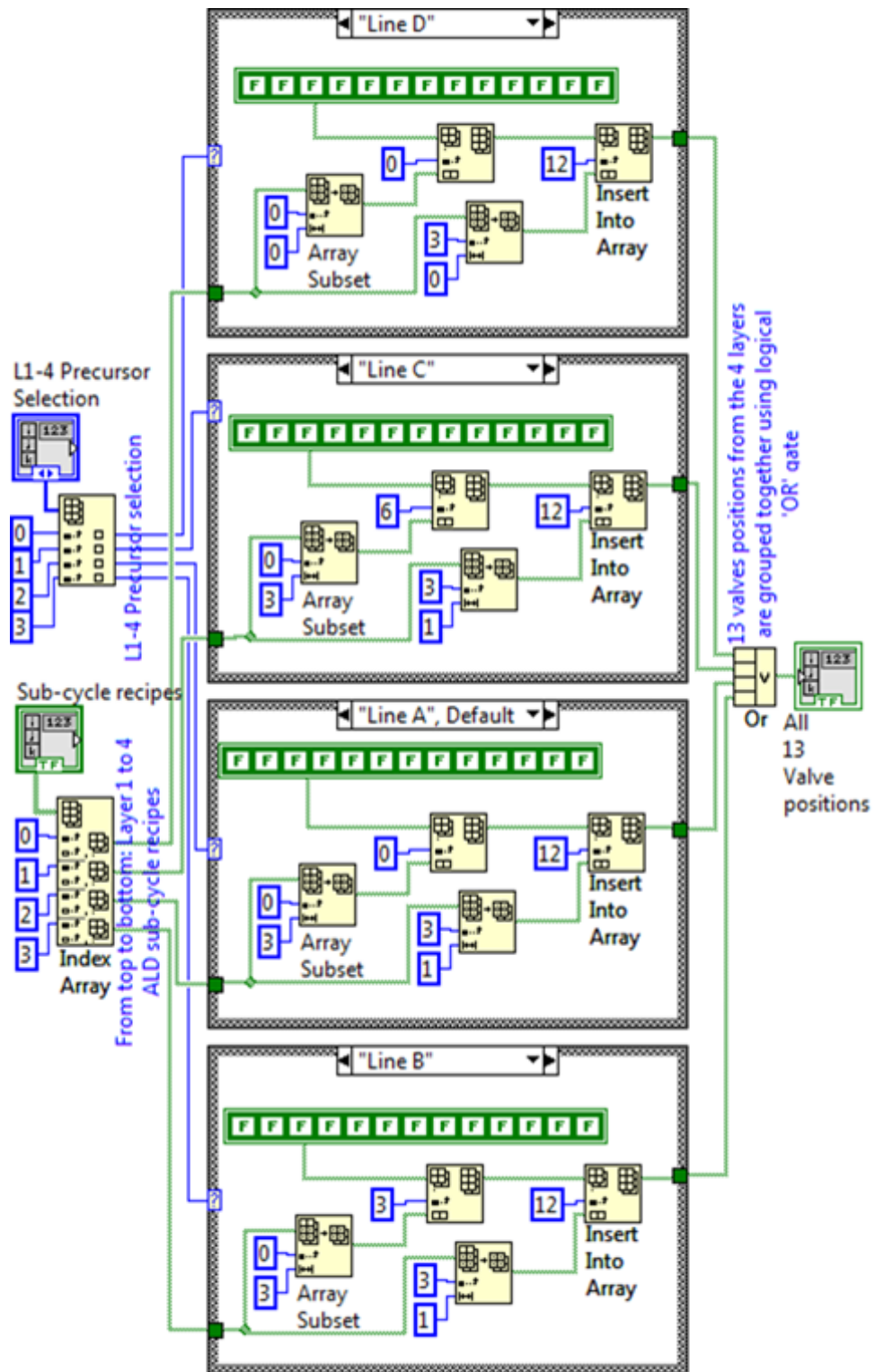


Figure 20: Sub VI: ALD Precursor Selector. The sub-VI has four case structures to represent four layers, with five cases for each case structure.

Wait before deposition

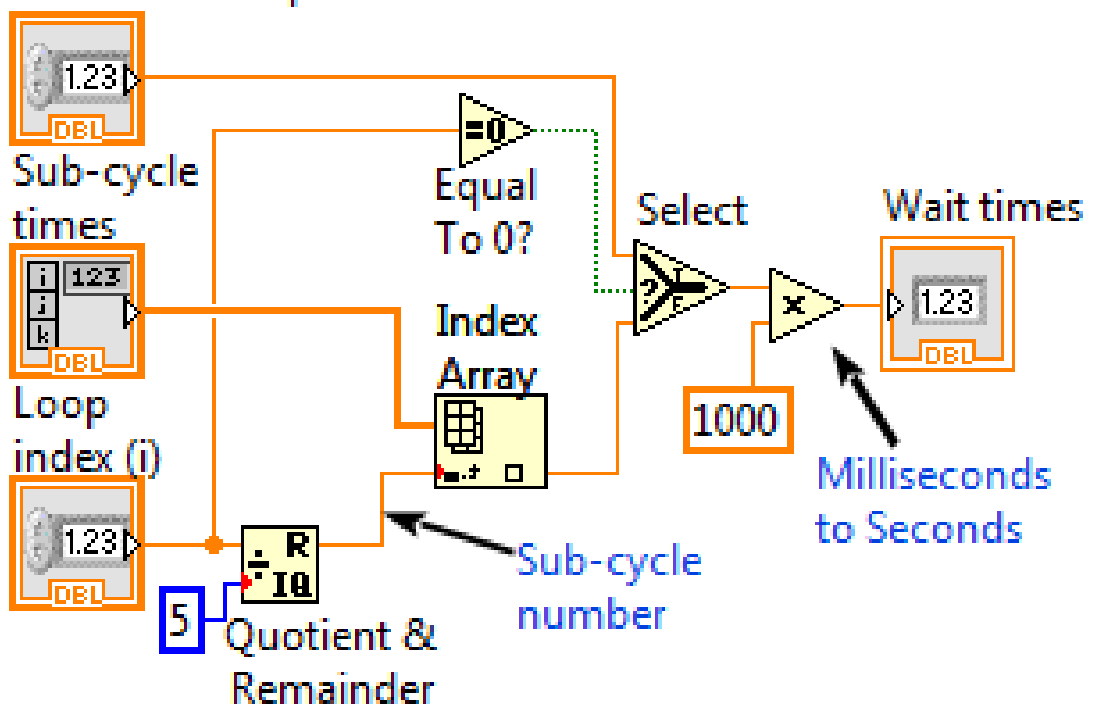


Figure 21: Sub VI: ALD Cycle Clock. This sub-VI is used to halt the loop iteration during ALD cycles. The output of this program is sent to Wait function as shown in Figure 16.

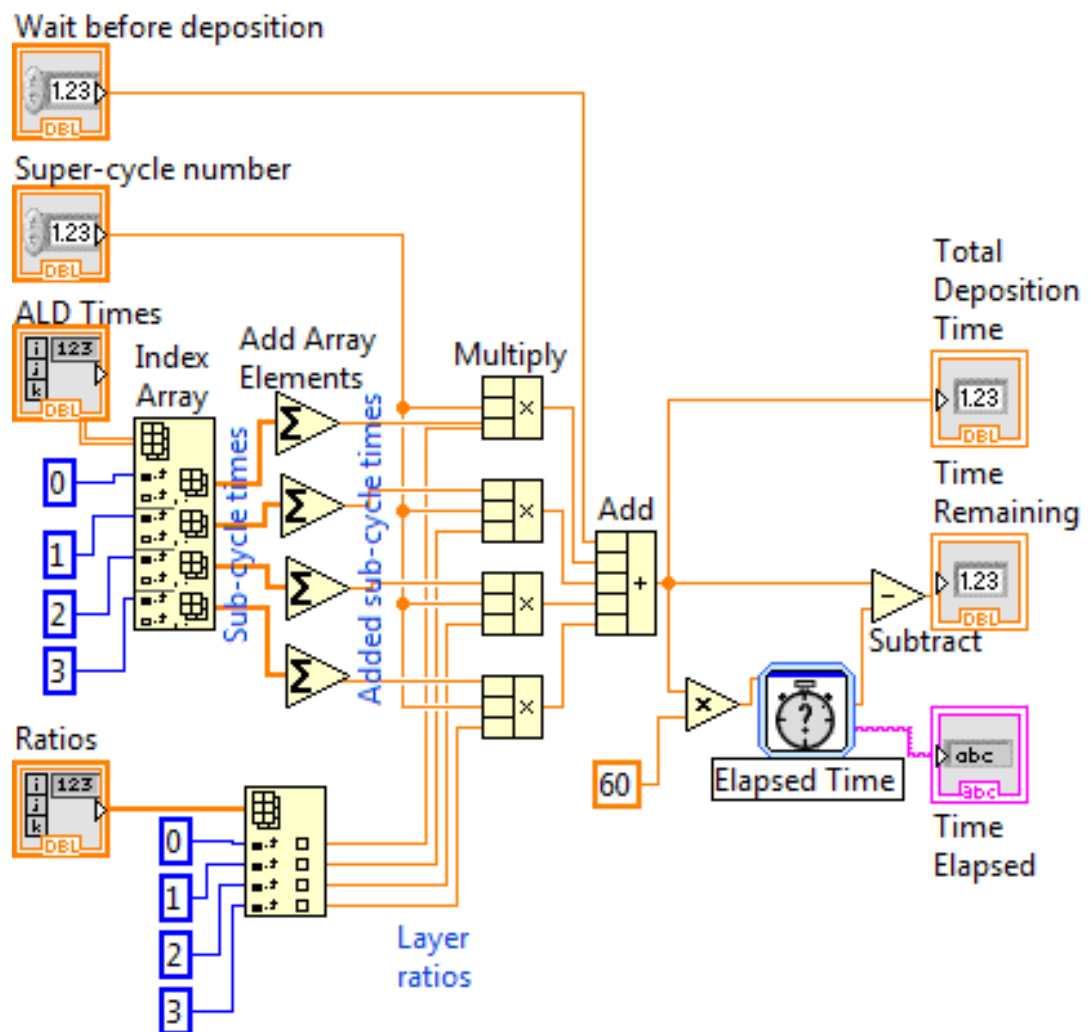


Figure 22: The Sub VI ALD Time shown here calculates total deposition time and time remaining using the ALD sub-cycle times, layer ratio and total number of super cycles.

### **2.2.6 Program testing**

The developed program was subjected to rigorous testing before inducting it for the actual ALD deposition process. The testing was carried out using various possible input parameters. One such test outcome is presented pictorially in Figure 23. In this case, all four precursors are used in reverse order with ratio 1. The program starts with wait before deposition sub-cycle and continue to ALD of precursor line D, C, B and A in sequential manner before reaching the final sub-cycle, in which all the valves are closed and the program stops thereafter.

### **2.2.7 Summary**

A scalable control program is designed and implemented in LabVIEW programming environment to control multi-precursor line flow type ALD reactor. The program can be used to deposit up to four layers (or more) using the four available precursor lines (or more) in the ALD system, cyclically, in any order in any combination and in any ratios. It is this versatility and scalability that makes this program useful and easily adaptable for similar ALD systems. The programming logic detailed in this section would aid the thin film researchers to design custom-written control programs to control their home-built ALD system or similar experimental systems.

		V1	V2	V3	V4	V5	V6	V7	V8	V9	V10	V11	V12	V13
Layer 1	Wait	F	F	F	F	F	F	F	F	F	F	T	F	F
	Cycle 1:Standby	F	F	F	F	F	F	F	F	F	F	T	F	F
	Cycle 1:P <sub>Pulse</sub>	F	F	F	F	F	F	F	F	F	T	T	F	F
	Cycle 1:P <sub>Purge</sub>	F	F	F	F	F	F	F	F	F	F	T	F	F
	Cycle 1:O <sub>Pulse</sub>	F	F	F	F	F	F	F	F	F	F	F	F	T
	Cycle 1:O <sub>Purge</sub>	F	F	F	F	F	F	F	F	F	F	T	F	F
Layer 2	Cycle 1:Standby	F	F	F	F	F	F	F	T	F	F	F	F	F
	Cycle 1:P <sub>Pulse</sub>	F	F	F	F	F	F	T	T	F	F	F	F	F
	Cycle 1:P <sub>Purge</sub>	F	F	F	F	F	F	F	T	F	F	F	F	F
	Cycle 1:O <sub>Pulse</sub>	F	F	F	F	F	F	F	F	F	F	F	F	T
	Cycle 1:O <sub>Purge</sub>	F	F	F	F	F	F	F	T	F	F	F	F	F
Layer 3	Cycle 1:Standby	F	F	F	F	T	F	F	F	F	F	F	F	F
	Cycle 1:P <sub>Pulse</sub>	F	F	F	T	T	F	F	F	F	F	F	F	F
	Cycle 1:P <sub>Purge</sub>	F	F	F	F	T	F	F	F	F	F	F	F	F
	Cycle 1:O <sub>Pulse</sub>	F	F	F	F	F	F	F	F	F	F	F	F	T
	Cycle 1:O <sub>Purge</sub>	F	F	F	F	T	F	F	F	F	F	F	F	F
Layer 4	Cycle 1:Standby	F	F	T	F	F	F	F	F	F	F	F	F	F
	Cycle 1:P <sub>Pulse</sub>	T	T	F	F	F	F	F	F	F	F	F	F	F
	Cycle 1:P <sub>Purge</sub>	F	F	T	F	F	F	F	F	F	F	F	F	F
	Cycle 1:O <sub>Pulse</sub>	F	F	F	F	F	F	F	F	F	F	F	F	T
	Cycle 1:O <sub>Purge</sub>	F	F	T	F	F	F	F	F	F	F	F	F	F
	End	F	F	F	F	F	F	F	F	F	F	F	F	F

Figure 23: Outcome of the ALD test run showing valve status of the all 13 valves during different ALD sub-cycles. The program starts with opening the by-pass valve of the Layer-1 precursor line and end with closing all the valves.

## CHAPTER 3

### RESULTS AND DISCUSSION

The developed ALD/CVD hybrid reactor was used to do ALD of metal oxides for different applications. Results and discussion of four such projects are described in this chapter.

#### 3.1 ALD of SnO<sub>x</sub>

This section was previously published as "Growth behavior and properties of atomic layer deposited tin oxide on silicon from novel tin(II)acetylacetonate precursor and ozone" in Journal of Vacuum Science & Technology A.

##### 3.1.1 Introduction

Tin oxide is widely studied for its application in gas sensors, heat reflective films, thin-film solar cells, oxidation catalysts and optoelectronic devices (52; 53; 54; 55; 56) because of its high transparency (>85%) (57), low resistivity and excellent chemical and thermal stability. (58) Tin oxide is a semiconductor with wide band gap ( $\sim 3.62$  eV) (57) showing n-type conductivity due to its oxygen vacancies. Besides good conductivity, the films have to form stable interface with a silicon surface without any interfacial reaction, such as the formation of SiO<sub>2</sub> by reduction of tin oxide film to elemental tin or sub-oxides at the interface. This is especially important for materials used as transparent conducting oxides (TCO), widely used in many optoelectronic devices. TCOs need to conduct electricity without obstructing photon transfer. The oxidation of silicon to SiO<sub>2</sub> at the interface through the reduction of tin oxide forms a barrier for electron



transfer across the  $\text{SnO}_x$ -Si interface found in solar cells. This leads to degradation of device properties. (59) The interface quality of tin oxide films depends on the deposition method and deposition conditions. Tin oxide has been deposited with several methods, such as sol-gel, (60) chemical vapor deposition, (61) electrostatic spray deposition, (62) spray pyrolysis, (63) magnetron sputtering (64) and atomic layer deposition (65; 66; 67; 68; 69; 70; 71) (ALD). Among these, precise thickness control, excellent conformality and uniformity makes ALD a suitable and preferable method for tin oxide deposition on complex surface geometries such as nanoporous solids used in nano-structured solar cells, for instance.

In this project, thin films of tin oxide were deposited using a novel tin(II) precursor, tin(II) acetylacetonate ( $\text{Sn}(\text{acac})_2$ ), on Si(100) substrate using a custom-built ALD reactor. Three different oxidizers were used as co-reactant in the ALD process. The ALD growth rate of  $\text{SnO}_x$  was examined for different precursor dosage, oxidizer dosage, substrate temperature and number of ALD cycles. A high ALD rate of  $0.1 \pm 0.01$  nm/cycle was observed within the wide ALD temperature window of 175-300 °C. The resulting  $\text{SnO}_x$  films were analyzed using x-ray photoelectron spectroscopy (XPS) for film & interface composition, x-ray diffractometry for structural characteristics, spectral ellipsometry for refractive index, optical profilometry for surface morphology, and four-point probe for resistivity.

### **3.1.2 Experimental**

$\text{SnO}_x$  films were deposited using  $\text{Sn}(\text{acac})_2$  precursor and ozone. Our custom built, hot-wall, perpendicular flow, diagnostic-accessible ALD reactor (1) was used to deposit thin films of  $\text{SnO}_x$  on highly doped P-type Si(100) substrates (resistivity 1-10  $\Omega\text{-cm}$ ). The reactor had

a base pressure of less than 40 mTorr and it can be heated up to 450 °C. The reactor has two delivery lines, one of which was loaded with the  $\text{Sn}(\text{acac})_2$  precursor and kept at 70 °C. The delivery lines and reactor walls are heated to 100 °C to avoid precursor condensation. The reactor can deliver three oxidants; water vapor, oxygen and ozone. All three oxidants were tried in this study. The deposition was carried out at 150-350 °C substrate temperature and 500 mTorr ALD chamber pressure. Nitrogen (99.998% purity) was used as carrier gas and purging gas to transport and purge the precursor. Si wafers were cleaned in accordance with the Radio Corporation of America standard cleaning (RCA SC-1) procedure, i.e., cleaning the substrate in 1:1:5  $\text{NH}_4\text{OH}:\text{H}_2\text{O}_2:\text{H}_2\text{O}$  solution for 15 min followed by a 1% HF dip for 10 s. Wafers were cleaned thoroughly with deionized water (resistivity  $\geq 17 \text{ M}\Omega\text{-cm}$ ) and nitrogen after every RCA cleaning step.

The thickness of  $\text{SnO}_x$  films were measured using spectral ellipsometry (Model M44, J.A. Woolam Co. Inc.). Film thickness was measured at three different points across the film. The mean value of these measurements represents film thickness and standard deviation represents film uniformity. The  $\text{SnO}_x$  film composition and  $\text{SnO}_x$ -Si interface quality were studied using a high resolution x-ray photoelectron spectrometer (Kratos AXIS-165, Kratos Analytical Ltd., United Kingdom) equipped with a monochromatic Al  $K\alpha$  (1486.6 eV) X-ray source operating at 15 kV and 10 mA. All spectra were taken using pass energy of 20 eV, dwell time of 200 ms and step size of 0.1 eV. The binding energies of all spectra were calibrated with the standard carbon 1s line at 285 eV. Glancing incidence x-ray diffraction (GIXRD) spectra was taken using a high resolution x-ray diffractometer (Philips X'pert) configured with the 0.1542 nm x-ray emission

line of Cu. An incident angle of  $1^\circ$  was used to reduce interference from the Si substrate and to increase sensitivity for thin films. Surface morphology of as-deposited and annealed  $\text{SnO}_x$  films were studied using a noncontact optical profiler (Wyko NT3300 system, Tucson, Arizona, USA) in the phase shifting interferometry (PSI) mode with a vertical resolution of 0.1 nm. Resistivity measurements were carried out using a four-point probe and Model 236 Source Measure Unit (Keithley Instruments Inc.). (72) Annealing of  $\text{SnO}_x$  thin films were performed in a preheated quartz furnace (Lindberg Blue three-zone furnace, Vernon Hills, Illinois, USA) in nitrogen for 5 min at different temperatures between 350 and 700  $^\circ\text{C}$ .

### 3.1.3 Results and Discussion

#### 3.1.3.1 Growth characteristics of $\text{SnO}_x$ thin films

Figure 24 & Figure 25 show the precursor and oxidizer saturation curves of the  $\text{SnO}_x$  ALD process using  $\text{Sn}(\text{acac})_2$  and ozone. Precursor and oxidizer dosage are controlled by the length of pulsing time. From Figure 24, it is evident that the Si substrate surface becomes completely saturated with tin precursor molecules after a 6 s long precursor pulse. No further increase in the growth rate (beyond 0.1 nm/cycle) was observed with further increases in the precursor dosage. This indicates the self-limiting nature of the process. Excess precursor is purged out by nitrogen for 15 s prior to the oxidant exposure. Among the three oxidants used (i.e., water vapor, oxygen and ozone), the tin precursor is found to react only with ozone; therefore ozone is used for all depositions in this study. The film growth rate was nearly insensitive to changes in the ozone pulsing time from 1 s up to 5 s (Figure 25). This indicates even a small amount

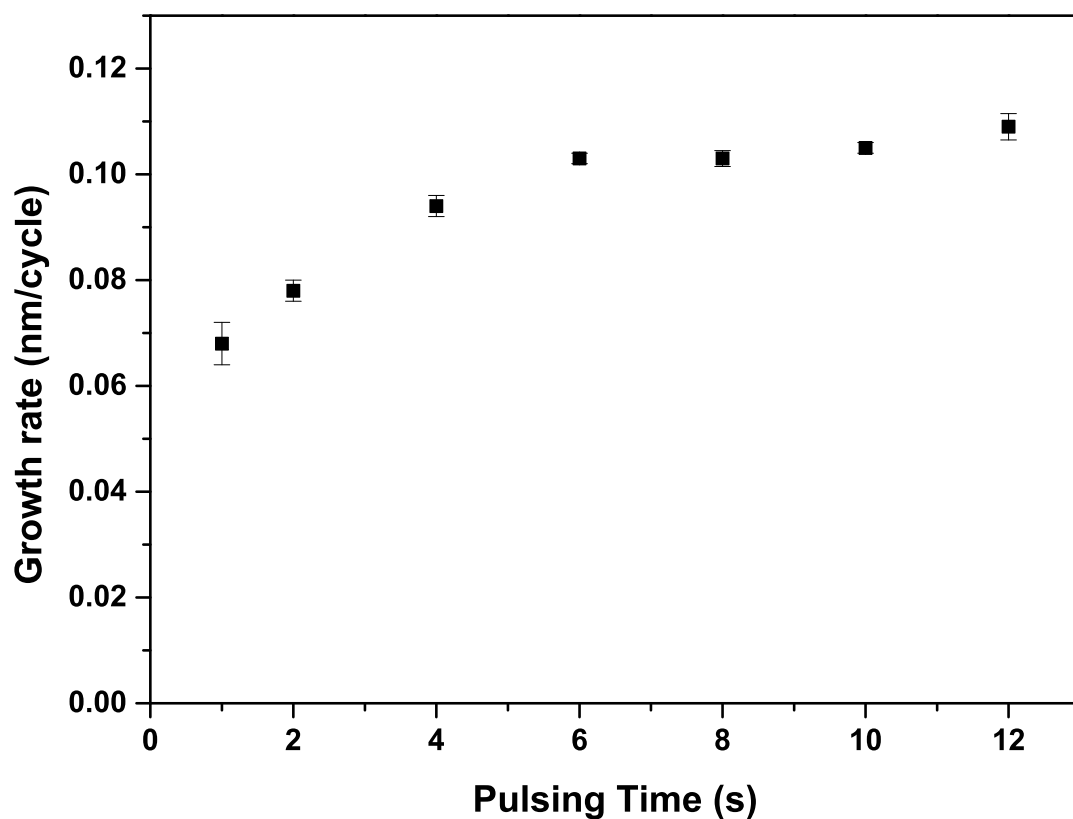


Figure 24:  $\text{Sn}(\text{acac})_2$  precursor saturation curve. The  $\text{Si}(100)$  substrate was at  $200\text{ }^\circ\text{C}$ . The  $\text{Sn}(\text{acac})_2$  precursor was kept at  $70\text{ }^\circ\text{C}$ . The system pressure was 0.5 Torr. The vertical error bars indicate film uniformity across the sample. Ozone pulsing time was kept constant at 1s.

of ozone is sufficient to react with the precursor ligands.

The temperature dependence of the growth rate is studied in the range of  $100\text{--}375\text{ }^\circ\text{C}$  (Figure 26). The growth rate is found to be independent of temperature from  $175$  to  $300\text{ }^\circ\text{C}$  indicating adsorption controlled growth regime. Outside this temperature window, the change of the deposition rate with temperature is significant. The high growth rate below the  $175\text{--}300\text{ }^\circ\text{C}$

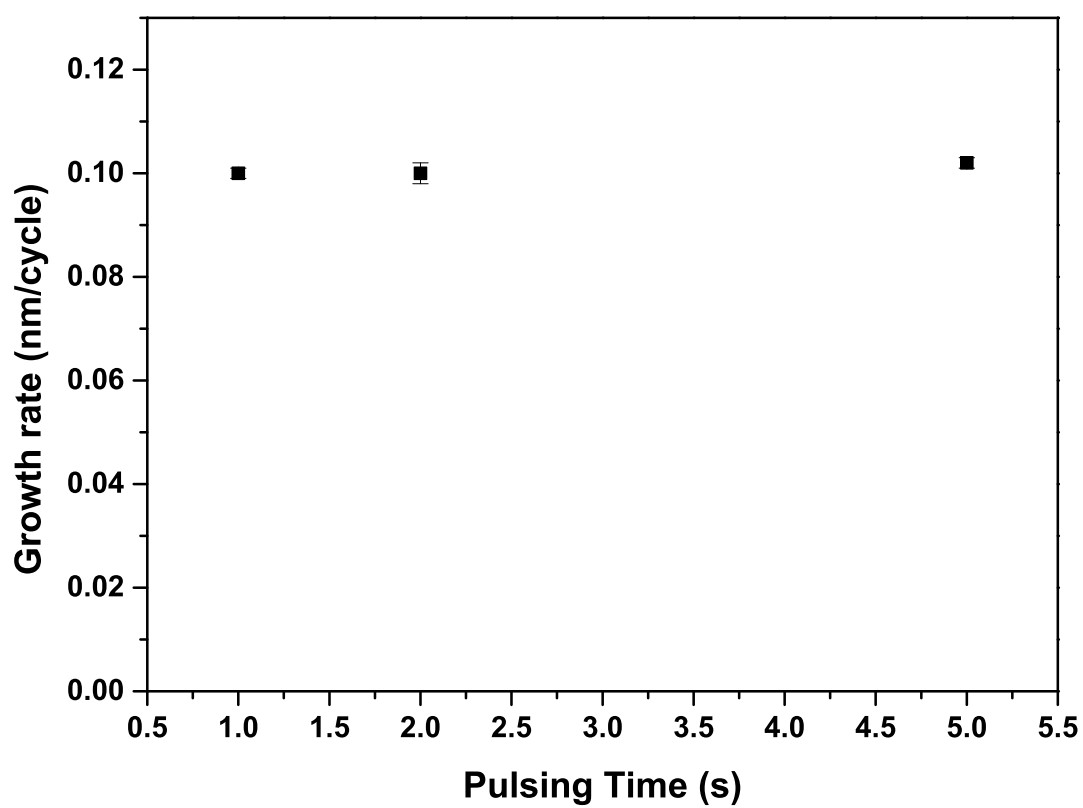


Figure 25: Ozone oxidizer saturation curve showing the effect of ozone dosage on the  $\text{SnO}_x$  film growth rate. Deposition conditions are the same as those in Figure 24.

temperature window may be due to precursor condensation on the substrate surface. The high growth rate above the temperature window is attributed to multilayer precursor deposition due to precursor decomposition. This wide temperature window makes this novel precursor suitable for co-deposition with many other materials that can be deposited within (part of) the same temperature window. Figure 27 shows the change of the tin oxide film thickness for different numbers of ALD cycles. The thickness is found to increase linearly without any apparent growth lag or rush for all different numbers of ALD cycles studied, i.e., up to 300. Constant growth rate facilitates excellent thickness tunability of the ALD process.

### **3.1.3.2 Compositional analysis of $\text{SnO}_x$ film and interface**

Interface properties of ALD  $\text{SnO}_x$  films have not been reported before. The interface quality of  $\text{SnO}_x$  films is crucial for TCO applications. In this study, Si oxidation at the interface was tested at two different temperatures using XPS analysis. The Si 2p core level spectra of 4 nm-thick as-deposited  $\text{SnO}_x$  film deposited at 200 °C and annealed at 600 °C in  $\text{N}_2$  atmosphere for 5 min are shown in Figure 28. The as-deposited film shows only peaks corresponding to bulk Si at 99.3 eV without any evidence of silicate (M-O-Si) at intermediate binding energies or  $\text{SiO}_2$  (O-Si-O) at higher binding energies. This indicates clean deposition with abrupt interface formation at 200 °C, in contrast to CVD deposited  $\text{SnO}_x$  that got reduced at the silicon interface and led to the formation of a  $\text{SiO}_2$  interlayer even for films deposited at temperatures as low as 150 °C. (73) In the XPS spectrum of the post deposition annealed film (Figure 28), an extra peak at 103.3 eV is indicative of  $\text{SiO}_2$ ; this strongly suggests oxidation of Si via reduction of

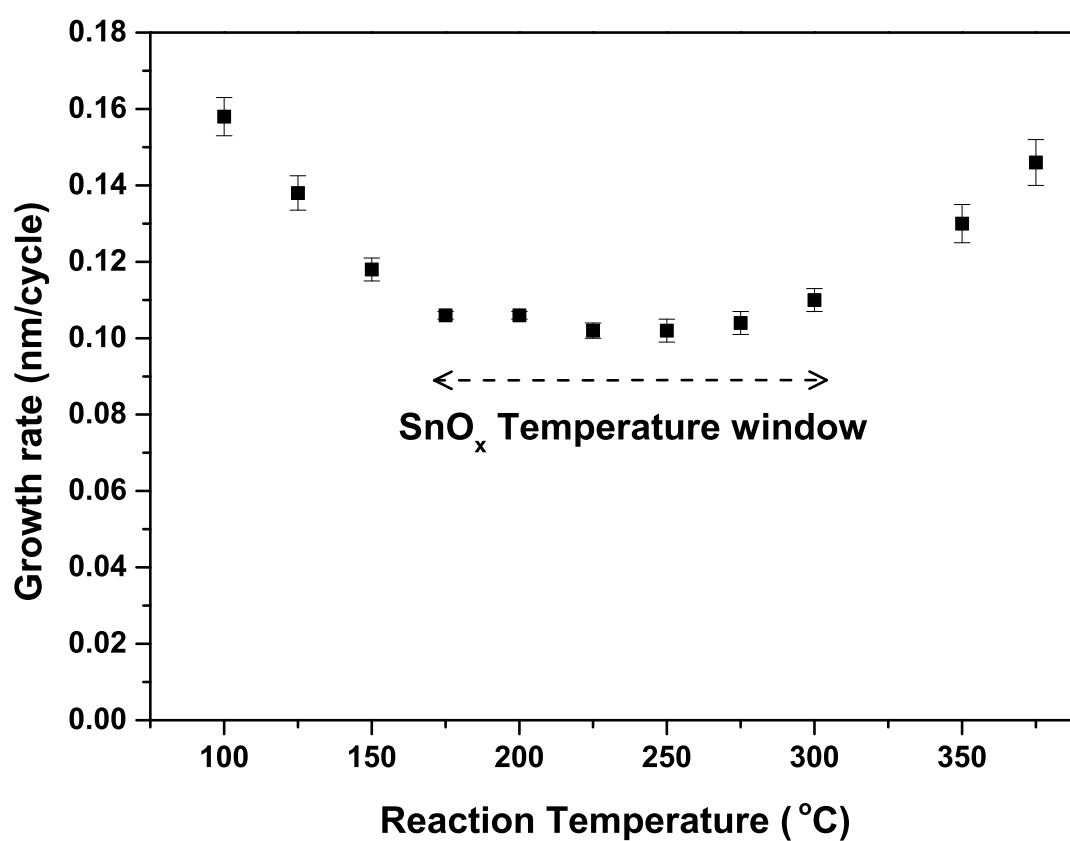


Figure 26: SnO<sub>x</sub> film growth rate as a function of substrate temperature. ALD was carried out using 6 s precursor pulse: 15 s N<sub>2</sub> purge : 1 s oxidizer pulse : 15 s N<sub>2</sub> purge. The precursor was kept at 70 °C and the deposition was carried out at 0.5 Torr.

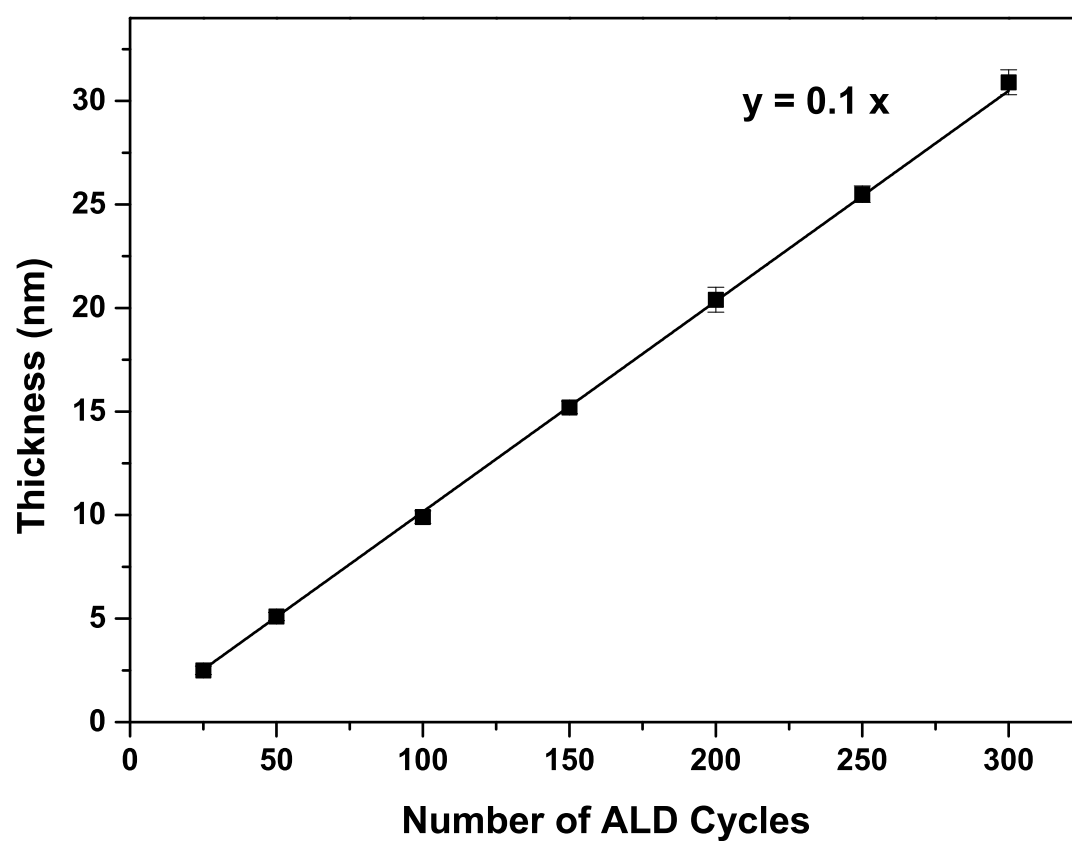


Figure 27: Thickness tunability of SnO<sub>x</sub> ALD process carried out at 200 °C. Deposition conditions are the same as those mentioned in Figure 26.



$\text{SnO}_x$  at the interface. This result is consistent with the values of Gibbs free energy of formation of  $\text{SiO}_2$  (-796 kJ/mole at 25 °C) (74) and  $\text{SnO}_2$  (-515 kJ/mole at 25 °C) (75) which indicate that formation of  $\text{SiO}_2$  is thermodynamically more favorable than that of  $\text{SnO}_2$ . High temperature annealing would have given the required activation energy to overcome a physical barrier such as a diffusion barrier and lead to the formation of a  $\text{SiO}_2$  interlayer. This ALD process will particularly be beneficial to deposit TCO for optoelectronic device applications that don't require annealing after the  $\text{SnO}_x$  ALD process; such as to deposit it as the top layer after finishing all high temperature deposition or annealing processes. The atomic ratio of O/Sn was found to be  $\sim 2.4$ . Excess oxygen might have come from the use of strong oxidizer (69) or from adsorbed moisture or carbon contamination on the film surface due to ambient exposure. Upon 10 min of sputtering using 200 nA  $\text{Ar}^+$  beam, partial surface reduction of  $\text{SnO}_x$  to elemental tin was observed. This is evident from the evolution of an extra peak at a lower binding energy in the Sn 3d spectra (Figure 29). Carbon contamination of  $\sim 4$  atom % was detected even after 30 min of  $\text{Ar}^+$  sputtering, which is not uncommon for films deposited using  $\beta$ -diketonate precursors. (6)

### 3.1.3.3 Film structural analysis

Figure 30 shows x-ray diffraction patterns of 30 nm-thick  $\text{SnO}_x$  films deposited at 200 °C and annealed at 500 °C and 700 °C. As-deposited films (inset) resulted in mostly background signal, without any specific diffraction peaks. This indicates amorphous as-deposited films. Annealed films resulted in diffraction features of the rutile phase of  $\text{SnO}_2$  with tetragonal structure. The diffraction peaks at 26.7, 33.9, 37.9, 51.8 and 54.8° are indexed to (110), (101), (200), (211) &

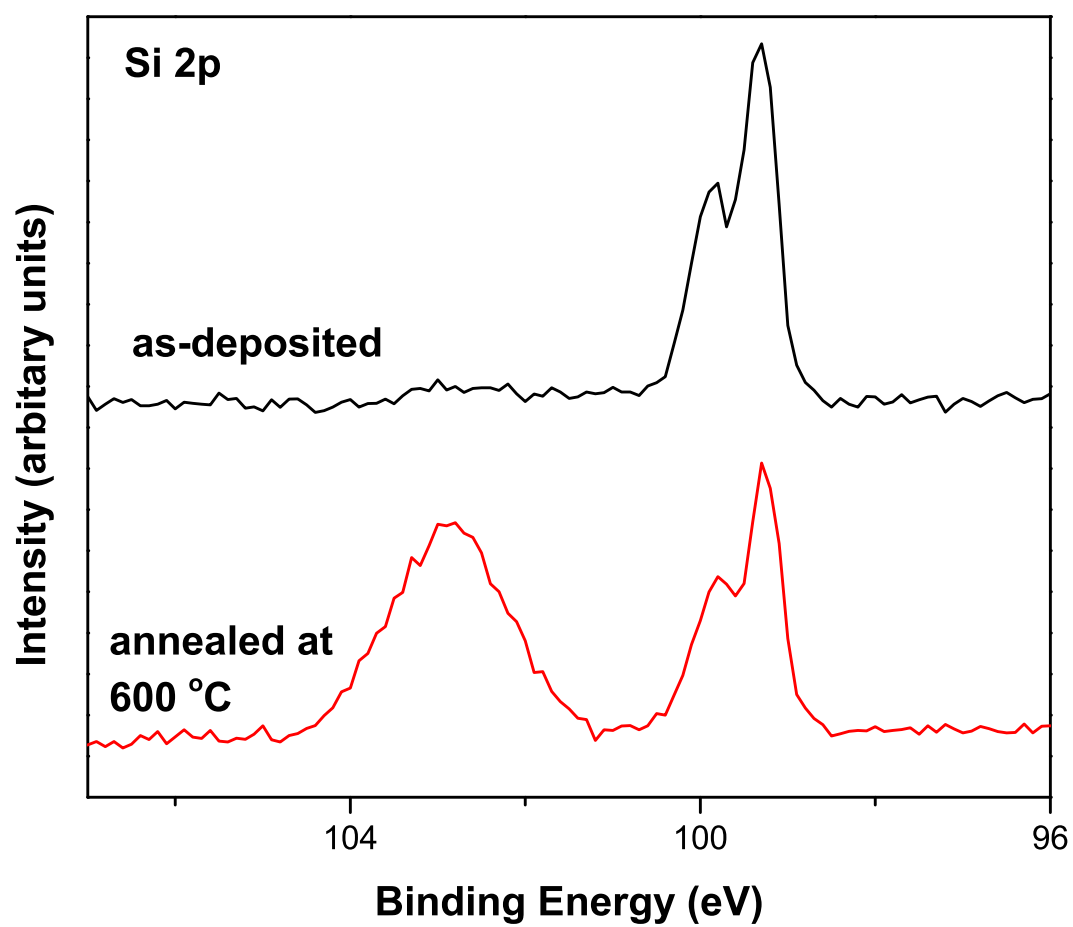


Figure 28: Si 2p core scans of 4 nm-thick  $\text{SnO}_x$  film before and after 600 °C annealing in nitrogen ambient for 5 min. Films were deposited at 200 °C. Other deposition conditions are the same as those in Figure 26.

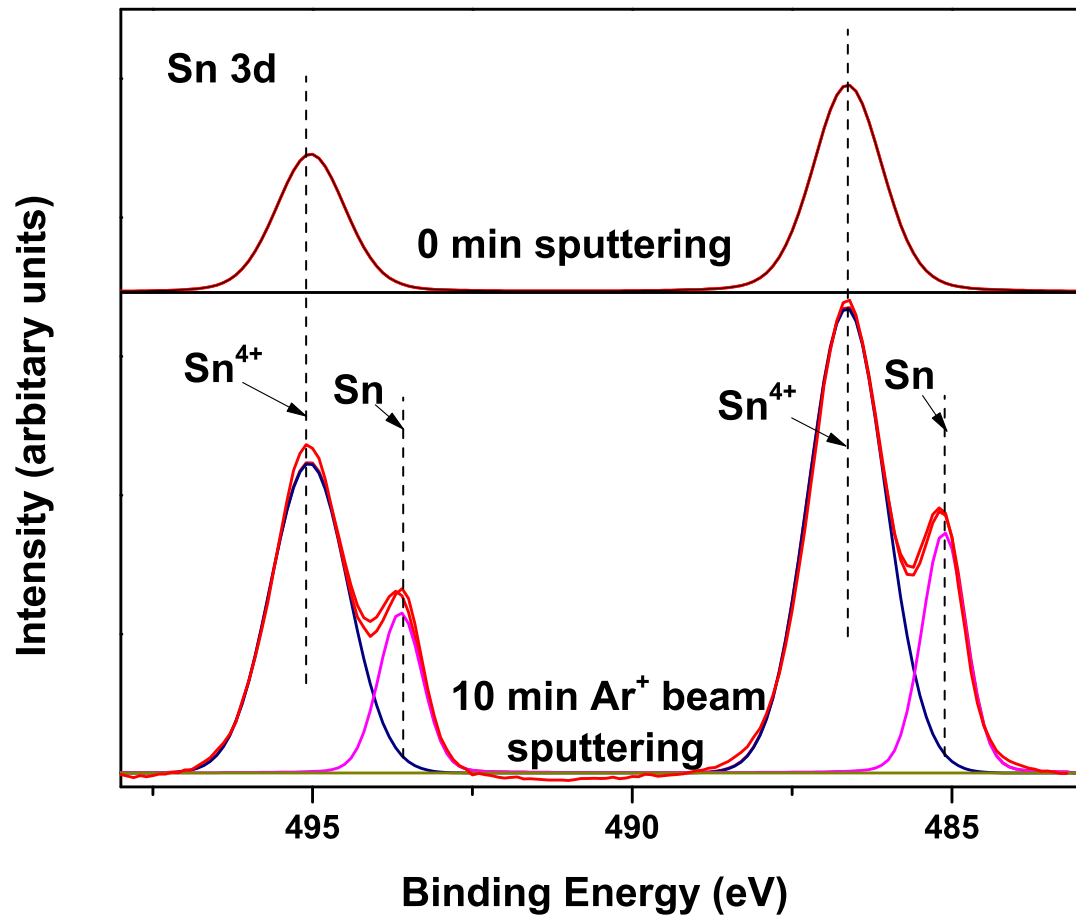


Figure 29: Sn 3d core scans of 20 nm-thick  $\text{SnO}_x$  as-deposited films showing the effect of  $\text{Ar}^+$  beam sputtering. The film deposition was carried out at 200 °C using the ALD deposition conditions mentioned in Figure 26.

(220) plane reflections of tetragonal  $\text{SnO}_2$  (JCPDS file no. 41-1445). These peaks were found to become sharper as the annealing temperature was increased from 500 to 700 °C, and this is attributed to increased crystallinity of the  $\text{SnO}_x$  film. The strongest peaks corresponding to (110) and (101) are common in both annealed films. Thus no apparent structural change happened between 500 and 700 °C besides increased crystallinity. The grain size of films annealed at 500 and 700 °C were calculated to be 4.8 and 6.4 nm, respectively, by using Scherrer's relation for the (110) and (101) reflections. The smaller grain size of films annealed at 500 °C corroborates its broader diffraction peaks. Lattice constants were calculated using Jade 9.0 software. The average lattice constants ( $a \times c$ ) for the tetragonal  $\text{SnO}_x$  films annealed at 500 and 700 °C were calculated to be 0.461 nm  $\times$  0.329 nm and 0.463 nm  $\times$  0.318 nm, respectively. These values are comparable with literature data (0.474 nm  $\times$  0.319 nm). (76) Mixed results were found in XRD studies of  $\text{SnO}_x$  ALD films deposited using different precursors. Choi, (67) Heo et al., (70) and Elam et al., (66) reported their as-deposited films to be amorphous, as opposed to Heo et al., (69) where they used different oxygen source and reported their as-deposited films at 120 °C to have rutile crystalline structure.

The refractive index is a measure of film density, composition and other film properties which change with changes in deposition and processing condition. The refractive index (at 450 nm) of  $\text{SnO}_x$  films was measured using spectral ellipsometry and plotted against deposition temperature (Figure 31). The refractive index of  $\text{SnO}_x$  thin films were relatively constant at  $\sim 1.75$ , below 175 °C deposition temperature. Above this temperature, the film refractive index

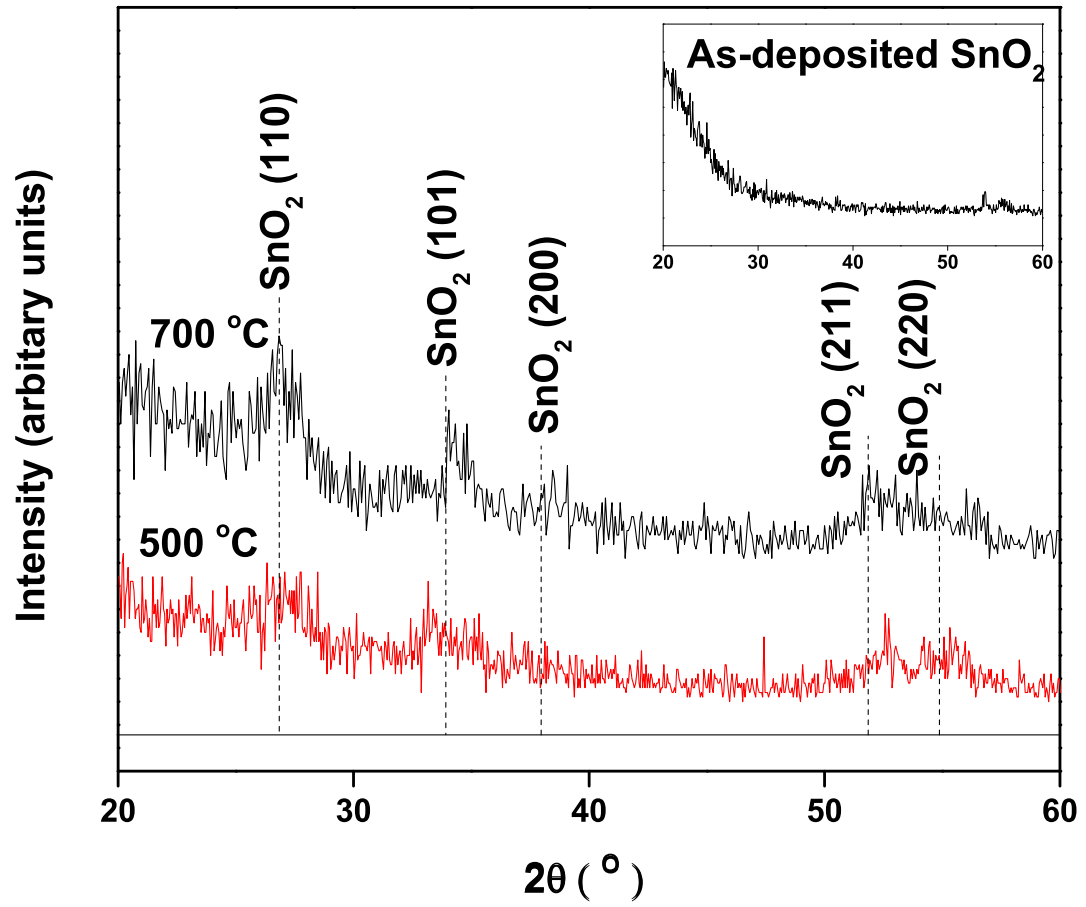


Figure 30: GIXRD of as-deposited and annealed 30 nm-thick SnO<sub>x</sub> films. Films were deposited at 200 °C. Other ALD conditions are the same as those in Figure 26. The annealing was carried out for 5 min in nitrogen.

was found to increase steadily with deposition temperature in the entire ALD temperature window and above. The increase in refractive index suggests the formation of a denser ALD film at higher deposition temperatures. Higher reactivity of the precursor and ozone at higher temperatures might favor the formation of denser films. It is noted that the refractive index of SnO ( $\sim 2.4$ ) is much higher than that of SnO<sub>2</sub> ( $\sim 2$ ) (66). This suggests that the films having refractive index value of 2.0 and above might have a SnO phase. Heo et al., (70) reported similar behavior with their tin(II) precursor above 250 °C. Their x-ray fluorescence spectra revealed the decomposition of tin precursor above 250 °C which helped the formation of a SnO-rich phase. Based on this, (70) Figure 31 indicates precursor decomposition above 300 °C which is consistent with our observation of higher ALD growth rates beyond the ALD temperature window (Figure 26). Our refractive index values are in good agreement with values reported for SnO<sub>x</sub> ALD films deposited using a different precursor. (70)

#### **3.1.3.4 Surface morphology studies**

Surface morphology is one of the key factors that determine the resulting property of a thin film. In some cases, it has been shown to correspond to changes in the underlying crystalline structure. (48) The surface morphology of 30 nm-thick as-deposited and annealed SnO<sub>x</sub> films are studied using a noncontact surface profiler operated in the PSI mode. The profiler produces a high-precision image of the sample surface using light interference. Among the tested films, as-deposited SnO<sub>x</sub> films had relatively smooth surface with a root-mean-square (RMS) roughness of 0.9 nm. The RMS roughness was found to increase gradually upon annealing

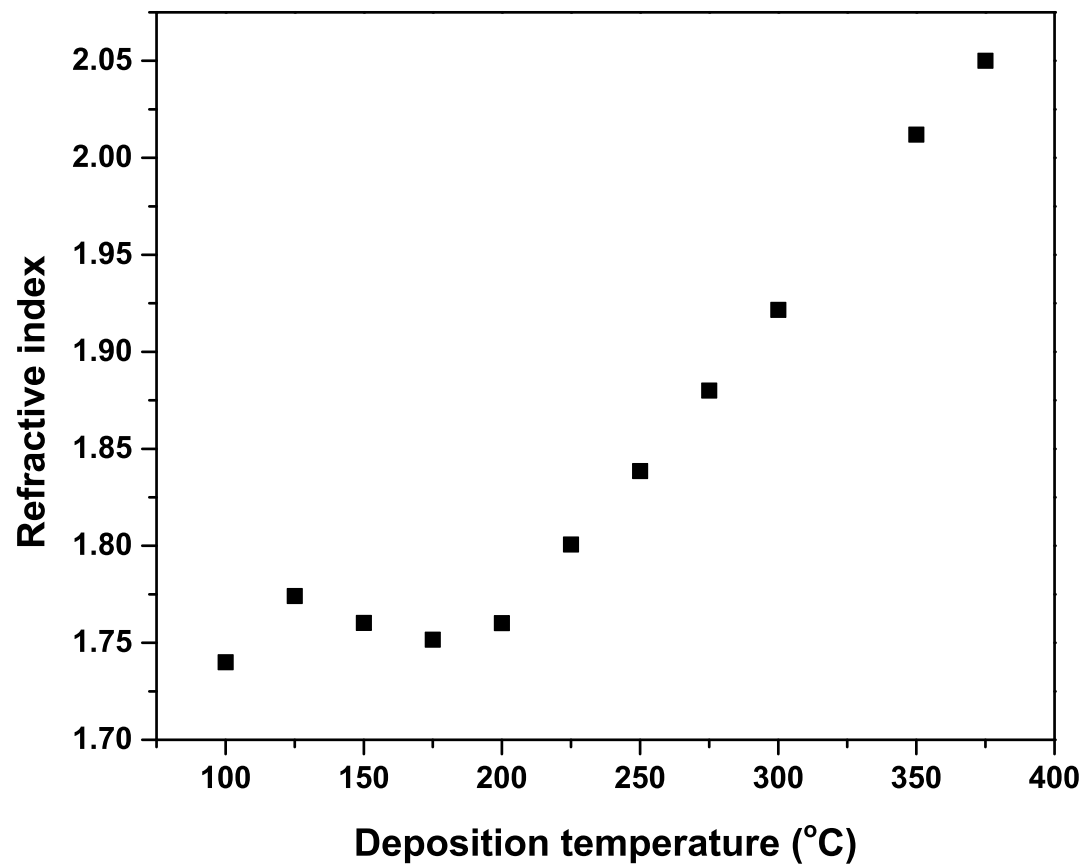


Figure 31: Refractive index (at 450 nm) of  $\text{SnO}_x$  films deposited at different substrate temperatures using the ALD deposition conditions mentioned in Figure 26

(Figure 32). The increase in roughness is consistent with increasing crystallinity of the  $\text{SnO}_x$  film as discussed in the previous section. The RMS roughness of 0.9 nm is slightly higher than the value (of 0.85 nm for the 91 nm-thick film) reported by Elam et al., (66) for  $\text{SnO}_x$  films deposited at slightly lower temperature (150 °C) using a different precursor. The increased roughness is attributed to the higher deposition temperature (200 °C) used in this study.

### 3.1.3.5 Film resistivity studies

One of the critical properties of TCO material is its resistivity. Resistivity of ALD  $\text{SnO}_x$  films are reported to have wide variations, from conducting films to insulating films depending on the ALD deposition and post-deposition treatment conditions. (70) Figure 33 shows current-voltage (I-V) characteristics of 20 nm-thick as-deposited and annealed  $\text{SnO}_x$  films measured using a four-point probe (FPP). (72) Films were deposited at 200 °C ; annealing was carried out at 600 °C in nitrogen ambient for 5 min. Thermally grown 100-nm thick silicon oxide layer was sandwiched between the silicon substrate and  $\text{SnO}_x$  film to minimize the effect of the substrate on the electrical measurements. The I-V curve was obtained by sweeping voltage from -80 mV to 80 mV between the outer two contacts of the FPP and plotting the resulting current against the voltage drop measured across the two inner contacts of the FPP. Linear dependence between the voltage and current indicates resistor-like behavior. The resistivity of  $\text{SnO}_x$  films was calculated by multiplying sheet resistance by film thickness measured using spectral ellipsometry. The resistivity of films deposited at 200 °C was calculated to be 0.6  $\Omega\text{-cm}$  (Figure 33, inset (a)). Annealing was found to lower the resistivity to 0.3  $\Omega\text{-cm}$  (Figure 33,



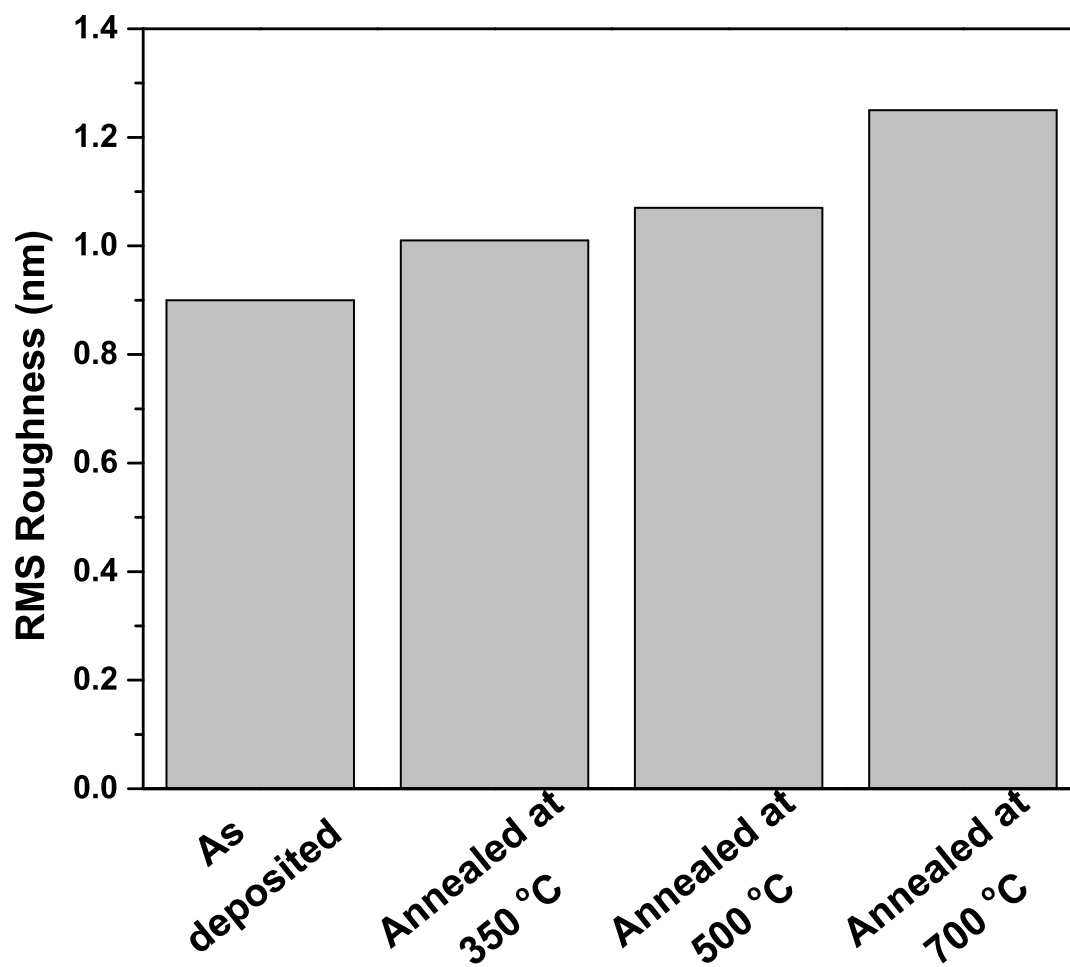


Figure 32: RMS roughness values of as-deposited and annealed SnO<sub>x</sub> films. Growth conditions are the same as those in Figure 26. SnO<sub>x</sub> films were deposited at 200 °C. Annealing was performed for 5 min in nitrogen.

inset (b)). Similar drop in resistivity due to annealing has been reported earlier and attributed to increased carrier concentration or mobility. (77; 78) Films deposited at a higher temperature (300 °C), within our ALD temperature window and subsequently annealed at 600 °C, showed no detectable change in resistivity (0.3  $\Omega$ -cm; Figure 33, inset (c)). The resistivity values are within the range of values reported for films prepared by ALD using other precursors. (69; 70)

#### 3.1.4 Summary

Thin films of tin oxide with a clear interface (i.e., without any SiO<sub>2</sub>) were deposited on silicon surfaces using a novel tin(II) precursor. ALD process parameters were optimized to determine optimum precursor and oxidizer dosages. A wide ALD temperature window was observed from 175 to 300 °C. As-deposited films were found to be amorphous with no formation of SiO<sub>2</sub> or other undesirable interfacial reaction products at the interface with silicon. Annealed films showed crystalline features that corresponded to SnO<sub>2</sub>, with simultaneous silicon oxide formation at the interface. Surface morphology studies of films showed fairly smooth films (RMS roughness of 0.9 nm) with a slight increase in roughness upon high temperature annealing. The resistivity of films deposited within the ALD temperature window and post-deposition annealed were found to be on the order of 0.3  $\Omega$ -cm. These results are promising for introducing Sn(acac)<sub>2</sub> as a suitable ALD precursor to deposit TCO without forming SiO<sub>2</sub> at the interface.

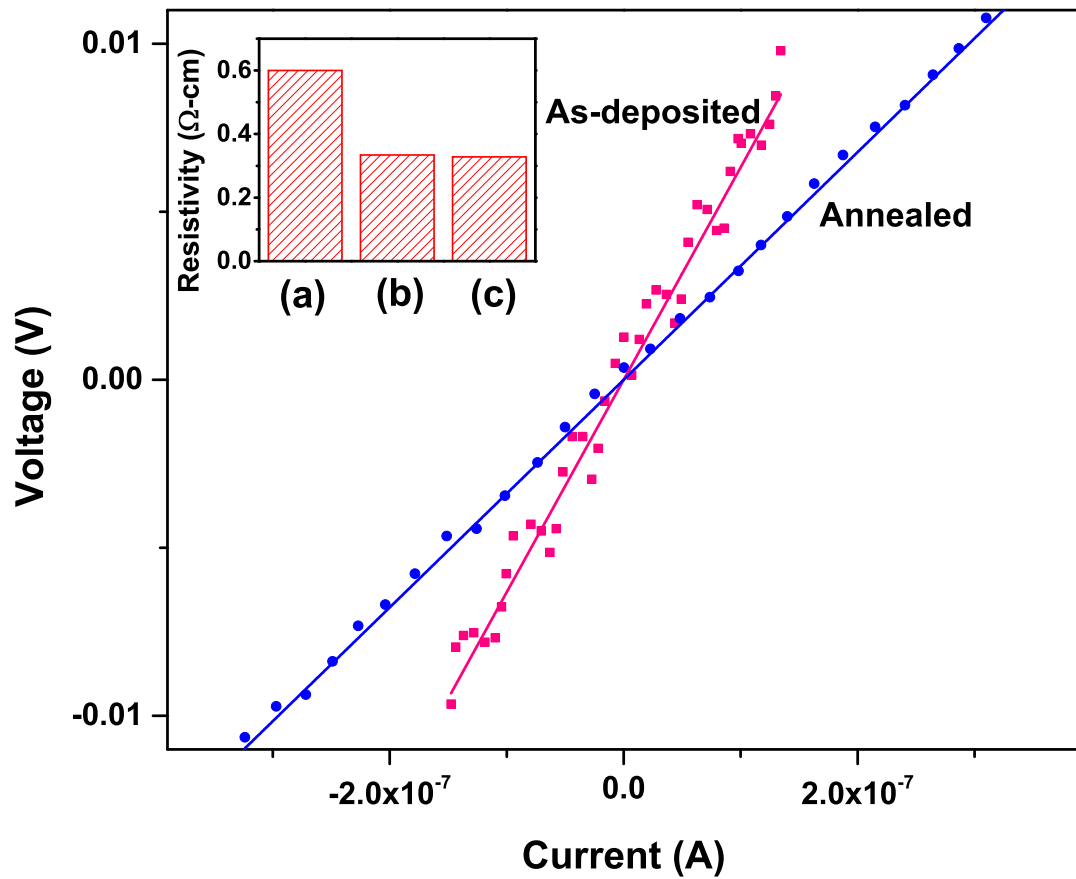


Figure 33: Current-voltage characteristics of as-deposited at 200 °C and post deposition annealed SnO<sub>x</sub> films (main); Resistivity of 20 nm-thick SnO<sub>x</sub> film deposited at 200 °C (inset (a)), post-deposition annealed at 600 °C for 5 min in nitrogen ambient (inset (b)), and deposited at 300 °C followed by annealing at 600 °C for 5 min in nitrogen (inset (c)).

### 3.2 Selective ALD of ZrO<sub>2</sub>

This section was previously published as "Selective atomic layer deposition of zirconia on copper patterned silicon substrates using ethanol as oxygen source as well as copper reductant" in Journal of Vacuum Science & Technology A.

#### 3.2.1 Introduction

Atomic layer deposition (ALD) is an effective vapor phase deposition technique to deposit wide variety of thin films with excellent conformality, and thickness and composition tunability. ALD is widely accepted and used in many technological areas, such as energy, catalysis, sensors, optoelectronics, semiconductor processing (79; 80; 35) etc. Semiconductor processing unanimously leads the race with an array of processing requirements that demand ultra-high purity and control. The current study focuses on a new approach for the selective atomic layer deposition (SALD) of ultra-thin layers for copper diffusion barrier applications. Such a diffusion barrier has to be deposited selectively on interlevel dielectric (ILD) surfaces (e.g., silicon oxide) without deposition on adjacent copper surfaces. Also, the deposition process should protect the copper surface from oxidation, as oxidation degrades mechanical and electrical properties of the copper surface. (81)

Self-assembled monolayers (SAM) have been widely studied for SALD. SAMs typically require extensive surface preparation steps and long assembly time. (82) Ever shrinking dimensions of microelectronic devices demand effective SALD without the need for extra processing steps. In our earlier reports on SALD of HfO<sub>2</sub> and TiO<sub>2</sub>, we made use of the difference in

nucleation time of precursor/oxidizer on different surfaces for selective deposition. (12; 83) The selectivity lasted 25 and 15 ALD cycles for  $\text{HfO}_2$  and  $\text{TiO}_2$ , respectively. This is partly due to the oxidation of copper surface when it gets exposed to water at 200 °C. (84) In this study, in order to prolong the selectivity and prevent oxidation of the copper surface we chose an oxidant-free ALD process. We used anhydrous ethanol, a strong copper reducing agent, (85; 86; 87) as the ALD co-reactant. Ethanol would aid the ALD on silicon while reducing the copper surface at the same time. Use of ethanol itself for the ALD process continuously reduces the copper surface from possible oxidation due to ALD by-products from the silicon side and prolongs selectivity. Figure 34 schematically illustrates the processing steps for the SALD of  $\text{ZrO}_2$  using ethanol.

Use of alcohols in the ALD process has been reported for  $\text{Al}_2\text{O}_3$ ,  $\text{Cr}_2\text{O}_3$ ,  $\text{HfO}_2$  and  $\text{TiO}_2$  films. (8; 9) Also,  $\text{Al}_2\text{O}_3$  films deposited using an alcohol as co-reactant produced denser ALD films than those deposited using oxygen or water. (10) This property of alcohol-based ALD could be particularly beneficial for copper diffusion barrier applications, as denser films make effective copper diffusion barriers.  $\text{ZrO}_2$  with relatively high lattice energy (11188 kJ/mol) (88) has high potential to be a good copper diffusion barrier in multilevel copper metallization for ultra large scale integration. In this study, the SALD of  $\text{ZrO}_2$  is studied along with its copper diffusion barrier characteristics.

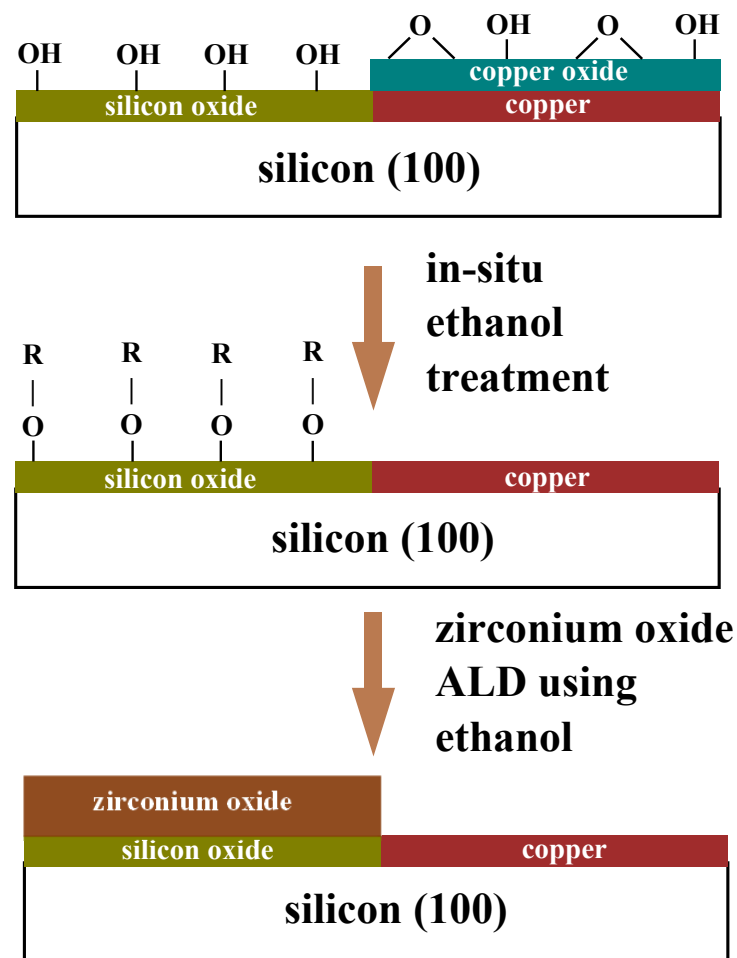


Figure 34: Schematic illustration of processing steps proposed for the SALD of  $\text{ZrO}_2$  using ethanol as the oxygen source.

### 3.2.2 Experimental

SALD of  $\text{ZrO}_2$  was carried out in a custom built, hot wall ALD reactor modified to use ethanol as a co-reactant. The reactor has a base pressure of less than 20 mTorr and is typically operated at 500 mTorr. Detailed description of the reactor can be found elsewhere. (36) 2 cm x 2 cm pieces of highly doped (resistivity 1-10  $\Omega\text{-cm}$ ) p-type silicon (100) were partially coated with 200 nm-thick e-beam evaporated (Varian; Model no. NRC3117) Cu and used as substrates to study the SALD of  $\text{ZrO}_2$  using ethanol. Half patterned samples ensure identical processing conditions for both surfaces. Tris(dimethylamino)cyclopentadienyl zirconium (ZyALD) kept at 50 °C was used as the metal precursor. Ethanol (200 proof) was kept in a glass wash bottle at ice temperature. An ice bath was used to maintain ethanol at a constant temperature and to reduce the concentration of ethanol in the nitrogen stream ( $\sim 10,000$  ppm). Prior to the ALD, the substrates were treated in-situ with ethanol vapor at 200 °C for 5 min to reduce the native oxide on the copper surface. The ALD runs were performed with 6 s of zirconium precursor pulse followed by 15 s of Ar purge, 10 s of ethanol pulse and 20 s of Ar purge in a cyclic manner. The  $\text{ZrO}_2$  deposition was carried out at 200 °C with 5 to 200 ALD cycles. The film thickness on the Si side of the sample was measured using spectral ellipsometry (Model M-44, J. A. Woollam Co.), whereas the film growth on the Cu side was probed with X-ray photoelectron spectroscopy (Kratos AXIS-165, Kratos Analytical Ltd.) equipped with a monochromatic Al  $K\alpha$  X-ray source. The copper diffusion barrier property of  $\text{ZrO}_2$  film was tested by annealing (RTP-600S, Modular Process Technology Co.) Cu/2 nm-thick  $\text{ZrO}_2$ /Si structures in 20 slpm  $\text{N}_2$  for 5 min at different temperatures starting with 500 °C. The breakdown-temperature of

the resulting barrier layer was studied by measuring the sheet resistance of the structure using a Keithley 2400 sourcemeter.

### 3.2.3 Results and Discussion

Figure 35 shows  $\text{ZrO}_2$  ALD film thickness on the silicon part of the substrate after different number of ALD cycles. Error bars in the graph represent the standard deviation of thickness measured at different points across the sample. The apparent linear increase in thickness with the ALD cycle number, at a rate of 0.04 nm/cycle, indicates a surface saturated growth with excellent thickness tunability, which is typical for ALD processes. The apparent absence of growth delay demonstrates good reactivity of the adsorbed alkoxide ions (-O-R) with the zirconium precursor on the silicon side of the substrate. The observed growth rate is, however, half of that of ALD  $\text{ZrO}_2$  when ozone is used as oxygen source (0.087 nm/cycle) with the same metal precursor in the same reactor. (89) A similar reduction in the growth rate has been reported for  $\text{Al}_2\text{O}_3$ ,  $\text{HfO}_2$  and  $\text{TiO}_2$ , when alcohol is used as a co-reactant. (10; 8) Such attenuated growth might be due to the lower reactivity of alcohols with the metal precursor than that of ozone with the precursor.

XPS survey scans on the silicon part of the substrates before the ALD process (Figure 36(a)) showed features corresponding to Si (2p: 103 eV and 2s: 154 eV), O (1s: 532 eV) and C (1s: 285 eV). The Si and O peaks are attributed to  $\sim 1.5$  nm-thick native oxide. The C peak is due to surface contamination from ambient exposure. In addition to Si and O peaks, the



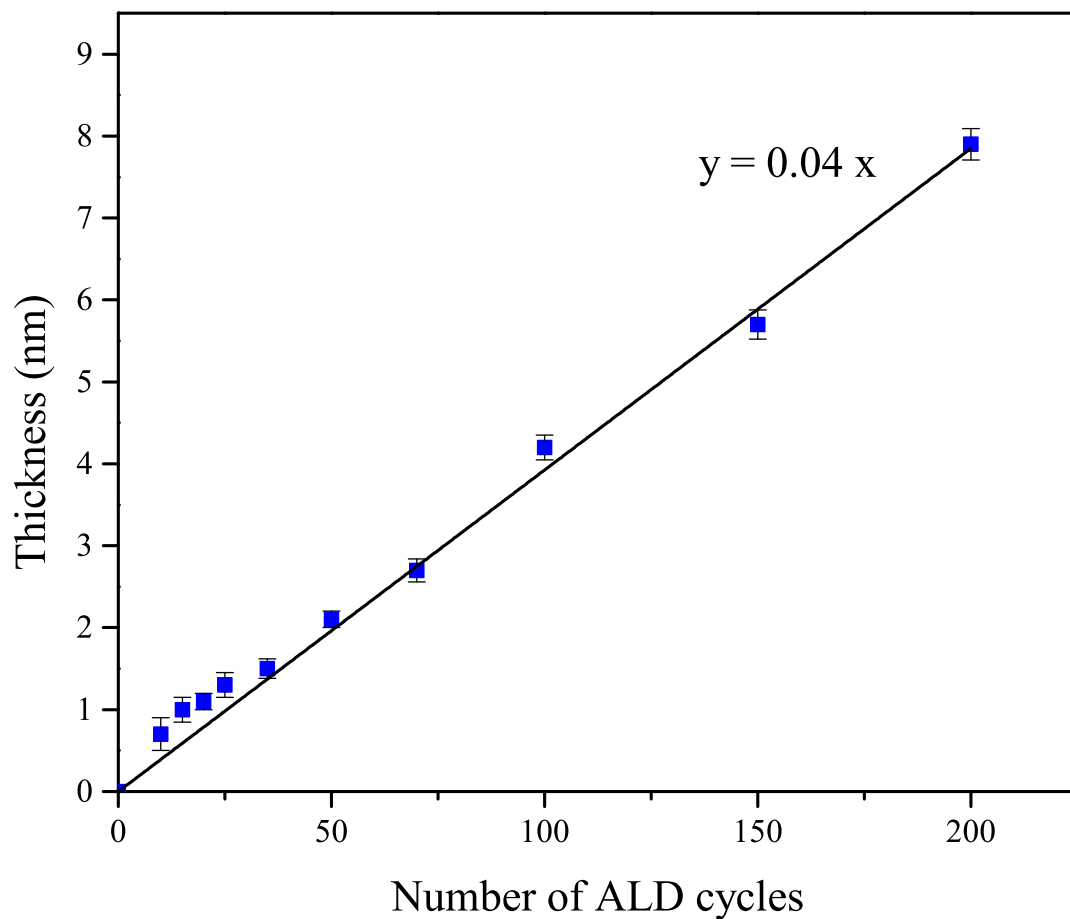


Figure 35:  $\text{ZrO}_2$ -ALD film thickness as a function of ALD cycle number showing excellent thickness tunability of the process on the silicon side of the substrate using ethanol as the oxygen source. The deposition was carried out at 200 °C substrate temperature and 500 mTorr deposition pressure using 6 s ZyALD : 15 s Ar : 10 s ethanol : 20 s Ar pulses.

XPS spectra of samples after 50 ALD cycles (Figure 36(b)) show features attributed to Zr (3d: 182 eV, 3p: 333 & 346 eV and 3s: 433 eV) and a more intense O 1s peak. Upon further ALD deposition, i.e., after 100 cycles (Figure 36(c)) the Zr and O peaks are seen to become intense whereas the Si feature becomes weak due to pinhole-free  $\text{ZrO}_2$ -ALD film on top of the Si substrate. Surface carbon due to ambient exposure was removed upon 5 min of  $\text{Ar}^+$  beam sputtering (Figure 36(d)). XPS scans showed no detectable nitrogen (from the precursor) in the film. Figure 36(a-c) qualitatively corroborate the  $\text{ZrO}_2$  thickness measured with spectral ellipsometry and indicate gradual continuous growth of  $\text{ZrO}_2$  on the silicon portion of the substrate.

The XPS survey scan on the copper side of the substrate before ALD resulted in Cu (2p: 932 & 952 eV, 3s: 122 eV and 3p: 75 eV), O (1s: 532 eV) and C (1s: 285 eV) peaks (Figure 37(a)). This is attributed to  $\sim 1$  nm-thick native oxide formed on the copper surface, as measured using spectral ellipsometry. The spectrum was practically unaltered after 70 ALD cycles except for an increase of the O feature. Stronger O peak might be due to the oxidation of the copper surface when the hot substrate on its way out of the ALD reactor is exposed to ambient air (81) before its cooling down with  $\text{N}_2$ . The absence of Zr features on copper (Figure 37(b)), in contrast to the strong Zr peaks on the Si portion of the substrates (Figure 36(b-d)), demonstrates selective deposition at least up to 70 ALD cycles. Absence of a peak in the Zr 3d core XPS spectra (not shown) taken after 70 ALD cycles also reconfirmed the SALD of  $\text{ZrO}_2$ . Such selectivity was not observed when common ALD oxidizers, i.e., water or oxygen were used. The presence of Zr peaks in the XPS survey scans of the copper surface after 50 ALD cycles of  $\text{ZrO}_2$  using water

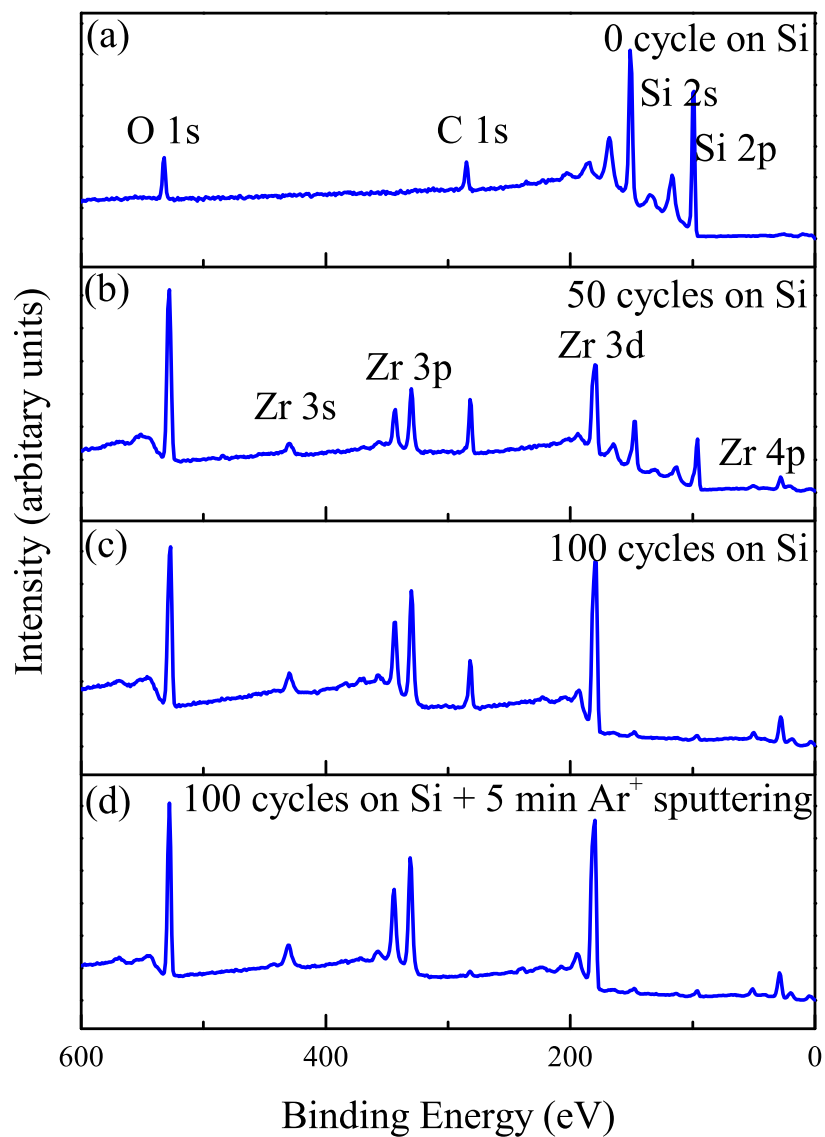


Figure 36: XPS spectra of the silicon side of the substrate after 0 (a), 50 (b) and 100 (c) ALD cycles. Upon 5 min of  $\text{Ar}^+$  beam sputtering, the C 1s peak disappeared (d). All deposition conditions are the same as those mentioned in Figure 35.

(Figure 38(a)) and oxygen (Figure 38(b)) as the oxygen sources indicates no selectivity or loss of selectivity before 50 cycles. The significant increase in selectivity when ethanol is used as the oxygen source could be due to the reduction of surface copper oxide to metallic copper, which in turn would reduce the number of potential nucleation sites on the copper side. However the selectivity appeared to diminish after 70 ALD cycles. This is apparent from the Zr peaks, though weak, on the copper side after 100 ALD cycles (Figure 37(c)). The Zr and O peaks grew in intensity after 200 cycles suggesting growth of  $\text{ZrO}_2$  on the copper surface (Figure 37(d)).

The probable explanation for the selective growth on silicon over copper is that, at the deposition temperature (200 °C), the interaction of ethanol with -OH terminated silicon surface alkoxyates the silicon surface by a dehydration reaction (90) until surface sites are saturated with chemisorbed ethanol. However, on the copper side, due to its catalytic activity, adsorbed alkoxides decompose to yield gaseous products, leaving behind metallic copper surface (85) Once the copper oxide, measured to be  $\sim 1$  nm is reduced, there may not be enough active nucleation sites for ethanol adsorption during the pretreatment and for precursor/ethanol during the ALD. After pretreatment, the silicon surface is alkoxyated and ready for the ALD process, whereas the copper surface becomes metallic copper without enough active nucleation sites for ALD. Thus, in this study, selectivity in the ALD process was achieved at least up to 70 cycles. However, adsorption and decomposition of alkoxides may leave a residual amount of surface oxygen on the copper surface. (85) The residual surface oxygen is believed to serve as a nucleation site for precursor molecules to adsorb, thus forming  $\text{ZrO}_2$  islands that may coalesce

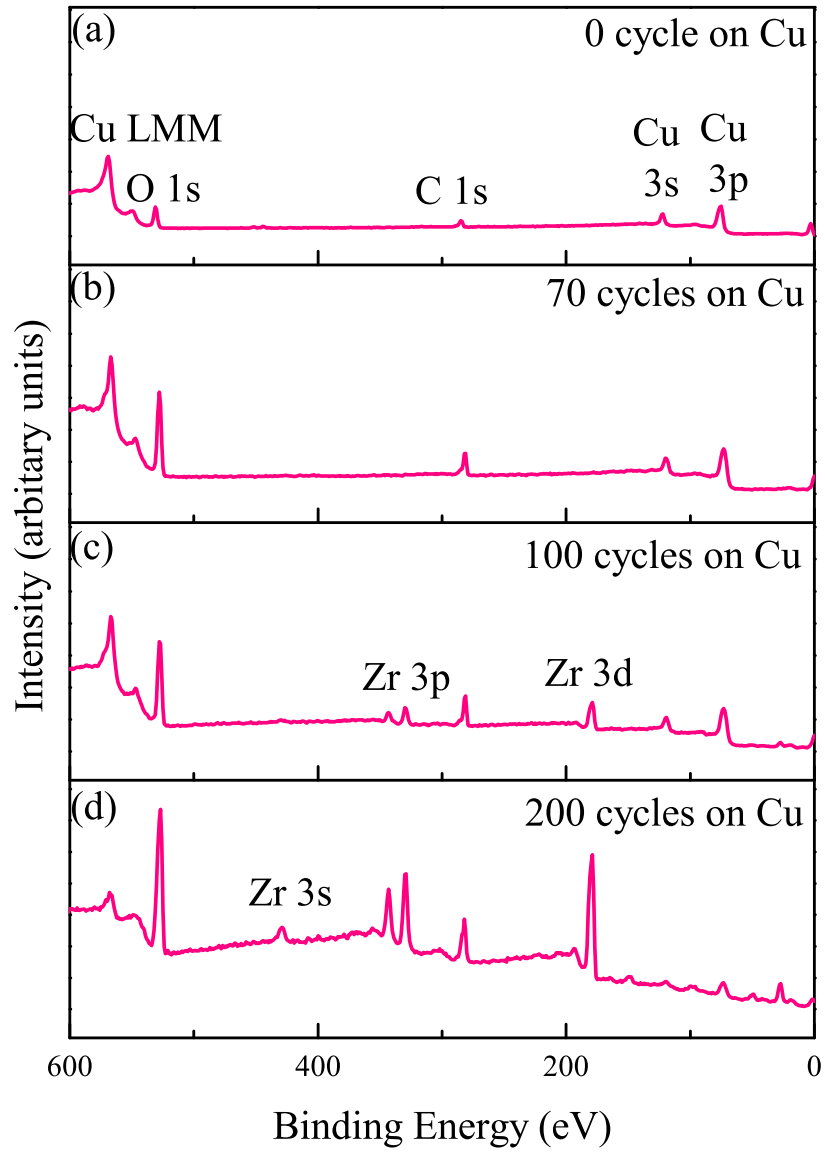


Figure 37: XPS spectra on copper side of the substrate after 0 (a), 70 (b), 100 (c) and 200 (d) ALD cycles, showing the onset of the ZrO<sub>2</sub>-ALD film growth only after 100 or more ALD cycles. The ALD conditions are the same as those in Figure 35.

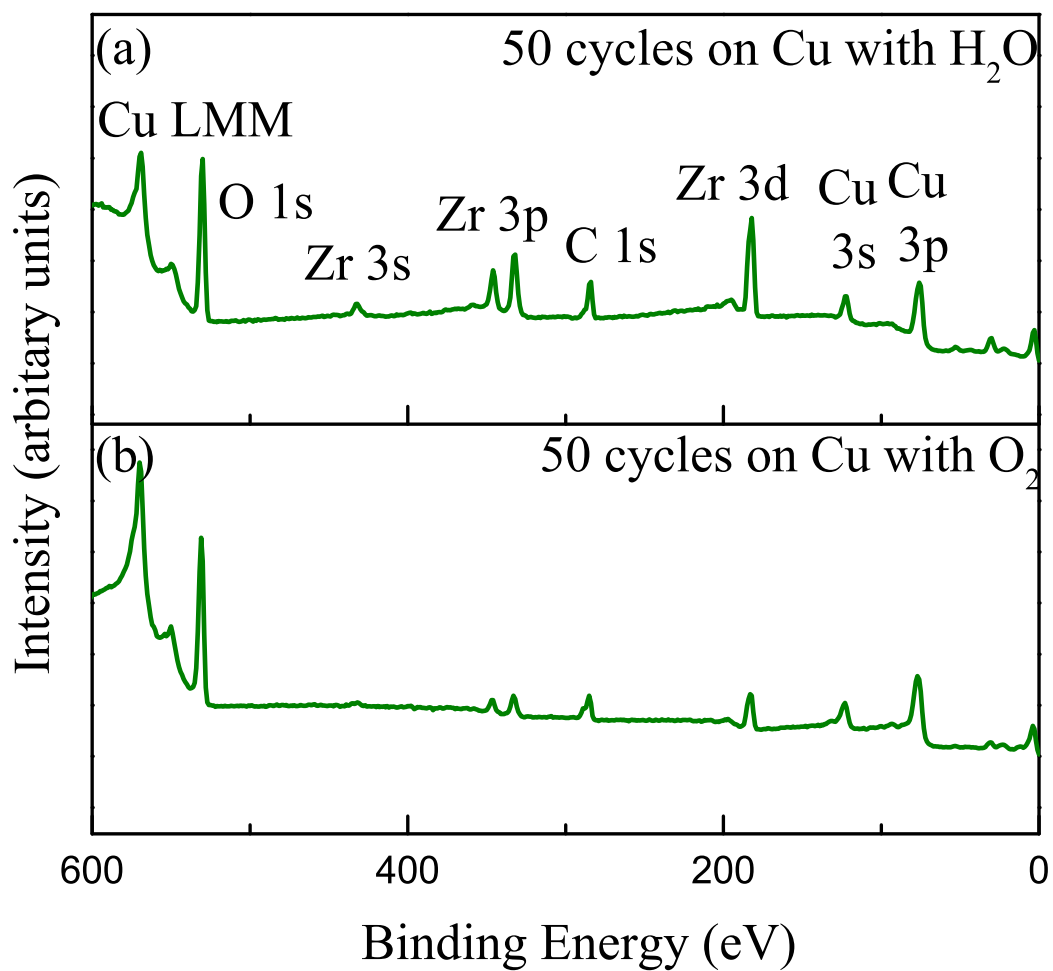


Figure 38: XPS survey scans on copper surface after 50 ZrO<sub>2</sub> ALD cycles using water (a) and oxygen (b) as the ALD oxygen sources. All other ALD parameters are the same as those in Figure 35.

into continuous film with continuing successive precursor and ethanol exposure. Adsorption of precursor molecule and subsequent formation of Cu-O-Zn bonding is corroborated by the FWHM of  $\sim 1$  eV (FWHM of Zr  $3d_{5/2} = 0.9$  eV;  $3d_{3/2} = 1$  eV) in the Zr 3d XPS spectra on the copper side of the substrate after 100 ALD cycles. This indicates the presence of only one type of doublet that corresponds to zirconium oxide with an oxidation state of +4. (91) It also rules out the presence of Zr-Cu or other type of bonding environments in the film or at the interface. Ethanol could also nucleate, to some extent on an oxygen-free copper surface and form alkoxides, (92) which is reactive towards the zirconium precursor. These might be a likely cause for loss of selectivity after 100 or more ALD cycles. However further studies are needed to elucidate the nucleation mechanism and to further prolong and enhance the selectivity.

The thermal stability of the resultant  $ZrO_2$  film as copper diffusion barrier was tested by annealing Cu/2 nm-thick  $ZrO_2$ /Si structures at different temperatures. When the Cu/2 nm-thick  $ZrO_2$ /Si structure is heated at 800 °C, an abrupt increase in the sheet resistance due to the formation of more resistive copper silicides indicates complete breakdown of the copper diffusion barrier (Figure 39). This is comparable to the barrier-breakdown temperature of  $Al_2O_3$  (700 °C) and  $HfO_2$  (675 °C) ALD films deposited using ozone as the oxygen source. (93)

### 3.2.4 Summary

SALD of  $ZrO_2$  was carried out on copper patterned silicon substrates using ethanol as the oxygen source.  $ZrO_2$ -ALD films on the silicon side of the substrate followed the typical ALD linear growth pattern with a growth rate of 0.04 nm/cycle at 200 °C without an apparent

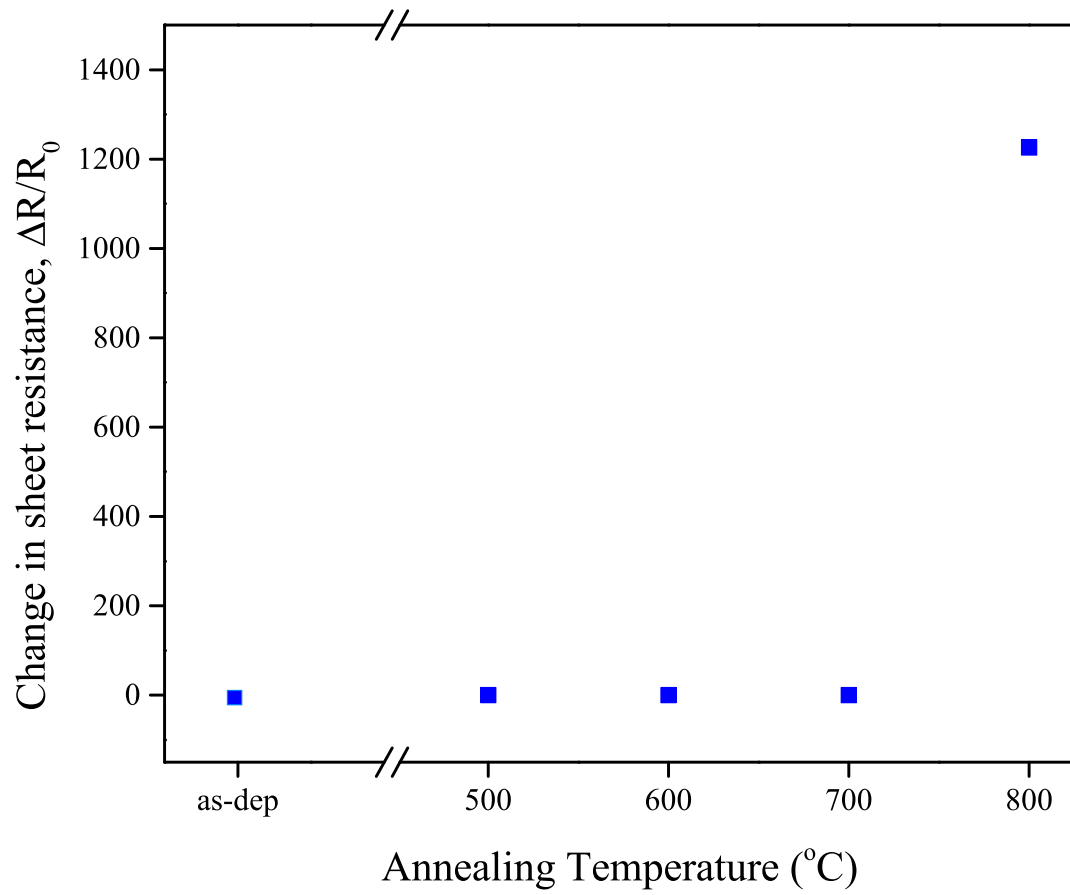


Figure 39: Change in sheet resistance ( $(R-R_0)/R_0$ ) of copper layer in as-deposited ( $R_0$ ) and annealed ( $R$ ) Cu/2 nm-thick  $\text{ZrO}_2/\text{Si}$  structures. The annealing was carried out in 20 slpm of  $\text{N}_2$  for 5 min.



growth delay, whereas technologically significant growth delay was observed on the copper side of the substrate. XPS measurements showed no  $\text{ZrO}_2$  growth at least up to 70 ALD cycles on the copper surface. Copper diffusion barrier characteristics of the resulting  $\text{ZrO}_2$  film were studied using Cu/2 nm-thick  $\text{ZrO}_2$ /Si structures. The  $\text{ZrO}_2$ -ALD films were found to withstand temperatures at least as high as 700 °C. Besides improved diffusion barrier characteristics of the  $\text{ZrO}_2$ -ALD films, the use of ethanol showed significant improvement in selectivity. This approach would work equally well for metal precursors that show reactivity towards ethanol, an effective copper reducing agent. These findings demonstrate the potential of introducing oxygen containing copper reductant for the selective ALD of metal oxides (and other technologically important material thin films) on copper patterned silicon surfaces. It is anticipated that the selective ALD of copper diffusion barriers could be effectively grown and controlled with reaction systems involving metal precursors and oxygen-containing copper reducing agents.

### **3.3 ALD of $\text{HfO}_2$ using ethanol**

This section was previously published as "Effect of using ethanol as the oxygen source on the growth and dielectric behavior of atomic layer deposited hafnium oxide" in ECS Transactions.

#### **3.3.1 Introduction**

Hafnium oxide ( $\text{HfO}_2$ ) is widely regarded as the suitable high-dielectric constant (high-k) material to replace conventionally used low-k silicon oxide for gate dielectric layers in complementary metal-oxide semiconductor (CMOS) devices. (94)  $\text{HfO}_2$  CMOS devices are in commercial production ever since 2007. (95) High dielectric constant ( $\sim 25$ ), large band gap (5.8 eV), sufficient band offset from Si and good thermodynamic stability against silicide formation

make  $\text{HfO}_2$  an ideal candidate for CMOS devices. (96; 97) Thin  $\text{HfO}_2$  high-k layers have been deposited by different deposition techniques such as chemical vapor deposition, physical vapor deposition, atomic layer deposition, sputtering etc. (94) Of all, atomic layer deposition (ALD) seems to be the suitable method to deposit ultra-thin conformal layers on deep trenches and 3D transistor structures. ALD is a vapor phase deposition technique, in which sequential exposure and purging of a substrate surface to reactive elements in vapor phase is used to grow thin films in layer-by-layer fashion with excellent control on film thickness and composition down to Ångstrom length scale. (47)

There are numerous studies on the ALD of  $\text{HfO}_2$  using different precursor and oxygen source combinations. (98) The chemical, structural and electrical properties of the resultant  $\text{HfO}_2$  film depends on precursor combination, deposition conditions, post deposition treatment conditions, etc. Earlier studies of the ALD of  $\text{HfO}_2$  reported the use of water vapor, oxygen or ozone as the ALD oxygen sources. (98) There are reports of uncontrolled oxidation of interfacial layer (IL) and subsequent formation of thick  $\text{SiO}_2$  IL during the ALD process from the use of strong oxidizers. (99) Uncontrolled oxidation will be a concern when further thinning of the chemical oxide formed IL is desired in future transistor scaling. This can be minimized by using an ALD oxygen source that does not oxidize silicon surface at the ALD deposition condition. Thus, to minimize the risk of uncontrolled oxidation and formation of thick IL during the ALD process, we investigated the use of ethanol as the ALD oxygen source and studied its effect on ALD

growth behavior, chemical composition and electrical behavior of the resultant ALD  $\text{HfO}_2$  film.

In this study, the effect of using ethanol as the ALD oxygen source on the ALD growth behavior such as precursor saturation, oxidizer saturation, ALD process temperature window and linear growth behavior is studied and compared with other common oxidizers. The chemical composition, purity and carbon contamination of the ALD  $\text{HfO}_2$  films and  $\text{HfO}_2$ -Si interface are studied with high resolution x-ray photoelectron spectroscopy. Dielectric characterization of the ALD  $\text{HfO}_2$  films are analyzed using current-voltage (I-V) and capacitance-voltage (C-V) curves of as-deposited and annealed samples and compared against similar samples prepared using water as the ALD oxygen source.

### **3.3.2 Experimental**

ALD of  $\text{HfO}_2$  was performed in a custom built hot-wall ALD reactor. The base pressure is less than 20 mTorr and the reactor is typically operated at 500 mTorr. More details about the reactor can be found elsewhere. (36) 2 cm x 2 cm pieces of highly doped Si(100) (resistivity: 1-10  $\Omega\text{cm}$ ; dopant: boron) was used as the substrate. Prior to ALD, the substrate was dipped in 2% hydrofluoric acid (HF) for 20 s to remove native oxide, followed by thorough deionized water rinse. The substrate was then blown dried with nitrogen (99.998% purity) and loaded immediately into the ALD reactor. Tetrakis(diethylamino)hafnium (TDEAH), kept at 60 °C in stainless steel bubbler was used as the metal precursor. Ultra high pure argon (99.999% purity) was used as the precursor carrier gas. 200 proof ethanol, kept in an ice bath, was used as the ALD oxygen source. The ice bath was used to maintain the ethanol temperature constant and

to reduce its vapor pressure. Argon was used to purge the excess precursor and oxidizer out of the deposition chamber. Precursor and ethanol dosages were controlled by changing their pulsing times. Water-based ALD process samples were prepared at 200 °C in a similar ALD system using the same metal precursor and deionized water (resistivity  $\geq 17 \text{ M}\Omega\text{-cm}$ ) as the ALD oxygen source. Details about the water based ALD  $\text{HfO}_2$  process is described elsewhere. (100)

ALD  $\text{HfO}_2$  film thickness was measured using spectral ellipsometry (J.A. Woollam Co. Inc., model M44). Film thickness was measured at three different places across the sample with mean reported as the film thickness and standard deviation represented as error bar in the graphs. A high resolution x-ray photoelectron spectrometer (Kratos AXIS-165) equipped with a monochromatic  $\text{Al K}\alpha$  (1486.6 eV) x-ray source operating at 12 kV and 10 mA was used to study the composition and bonding nature of the ALD  $\text{HfO}_2$  film and  $\text{HfO}_2\text{-Si}$  interface. Dielectric characterization of the film was carried out using a Keithley semiconductor characterization system (model 4200-SCS). 150 nm-thick Al metal contact layer was e-beam evaporated (Varian model no. NRC3117) for dielectric characterization. Shadow mask was used to define circular contacts (area  $0.7 \times 10^{-2} \text{ cm}^2$ ) during e-beam evaporation. C-V and I-V measurements were performed over the voltage range of -5 to +5 V. C-V was done by sweeping voltage from accumulation region to inversion region and then sweeping back to accumulation. C-V measurement was performed with 100 kHz ac frequency. All C-V and I-V curves were recorded in dark at room temperature. Annealing of samples was carried out in preheated quartz furnace (Lindberg Blue STF) in nitrogen environment at 700 °C temperature and ambient pressure for 5 min.

### 3.3.3 Results and Discussion

#### 3.3.3.1 ALD HfO<sub>2</sub> Growth Behavior

ALD growth rate primarily depends on the metal precursor, oxidizer, substrate surface and substrate temperature. The size of the metal precursor ligand affects the ALD growth rate. (47) Bulky precursor ligand causes steric hindrance and blocks the accessibility of nearby surface reactive sites. This causes sub-monolayer coverage, usually observed in ALD processes. The percentage of monolayer coverage determines the ALD growth rate. High coverage leads to high ALD growth rate.

The reactivity of the metal precursor/oxidizer to the substrate reactive sites affects the initial ALD growth rate. The reactive nature of surface reactive sites depends on its surface termination. For instance, HF treated H-terminated silicon is believed to be less reactive silicon surface than its OH-terminated counterpart. H-terminated surface in many cases causes nucleation problems and 3-D growth during initial ALD cycles. Thus the reactivity of metal precursor/oxidizer with substrate reactive sites affects the initial ALD growth rate. The metal precursor reactivity with film surface reactive sites affects the ALD growth rate, once all the substrate surface is covered by the ALD film. The ability of the oxidizer to burn or replace the ligand of adsorbed precursor molecules determines the number of reactive sites made available for the next ALD cycle. More reactive oxidizers help create higher number of reactive sites that results in high ALD growth rate.

ALD of  $\text{HfO}_2$  has been investigated by many investigators using a variety of precursor - oxidizer combinations at different processing conditions and reported wide variation in growth, composition and electrical characteristics of the resultant film. (98) In the context of this study, in order to investigate the effect of using ethanol on the growth behavior, the discussion is limited to studies that used TDEAH as the metal precursor.

ALD of  $\text{HfO}_2$  films were performed after optimizing precursor and oxidizer pulsing times. Figure 40 shows  $\text{HfO}_2$  film thickness as a function of TDEAH precursor dosage. Precursor dosage was controlled by the length of pulsing time. It is seen in the figure that the film growth rate increases gradually and saturates at 5 s precursor pulsing time. No further increase in growth rate was observed for precursor pulsing times beyond 5 s. This indicates the need for about 5 s of precursor pulse in order to saturate the substrate surface with precursor molecules. Similar experiments with different ethanol pulsing times resulted in constant growth rate (Figure 41). The ethanol pulsing time of 1 s seems to be enough to react with the adsorbed precursor molecules on the substrate surface and also to functionalize the film surface for the next ALD cycle. Sufficient purging times of 15 s were used after precursor and oxidizer pulses to avoid gas phase reaction, typically observed in chemical vapor deposition processes. No change in the growth rate for purging times beyond 15 s was also verified. The optimized precursor pulsing time of 5 s and oxidizer pulsing time of 1 s was used to grow our ALD  $\text{HfO}_2$  films.

ALD growth rates of  $\text{HfO}_2$  films deposited at different temperatures are shown in Figure 42. The graph shows three distinct growth regimes. High growth rate at temperatures lower than

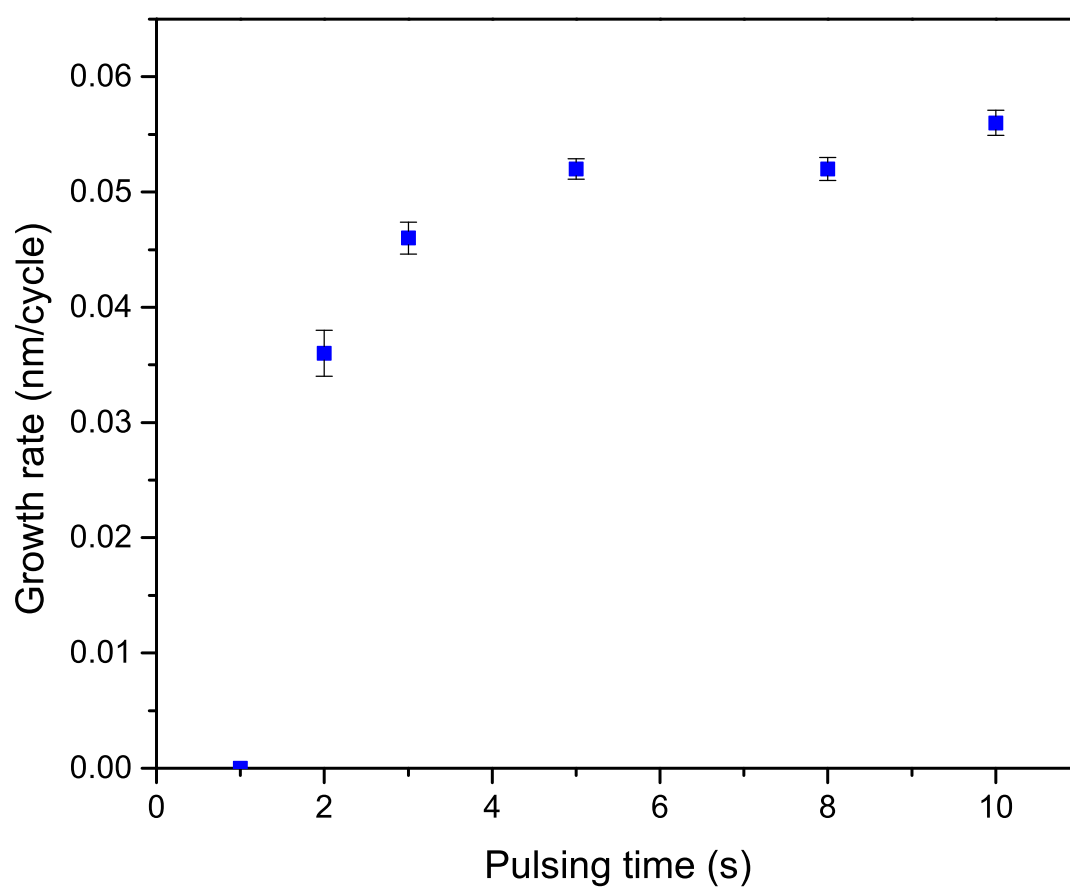


Figure 40: ALD HfO<sub>2</sub> growth rate on Si(100) as a function of precursor pulse time at 200 °C and 500 mTorr. TDEAH was kept at 60 °C.

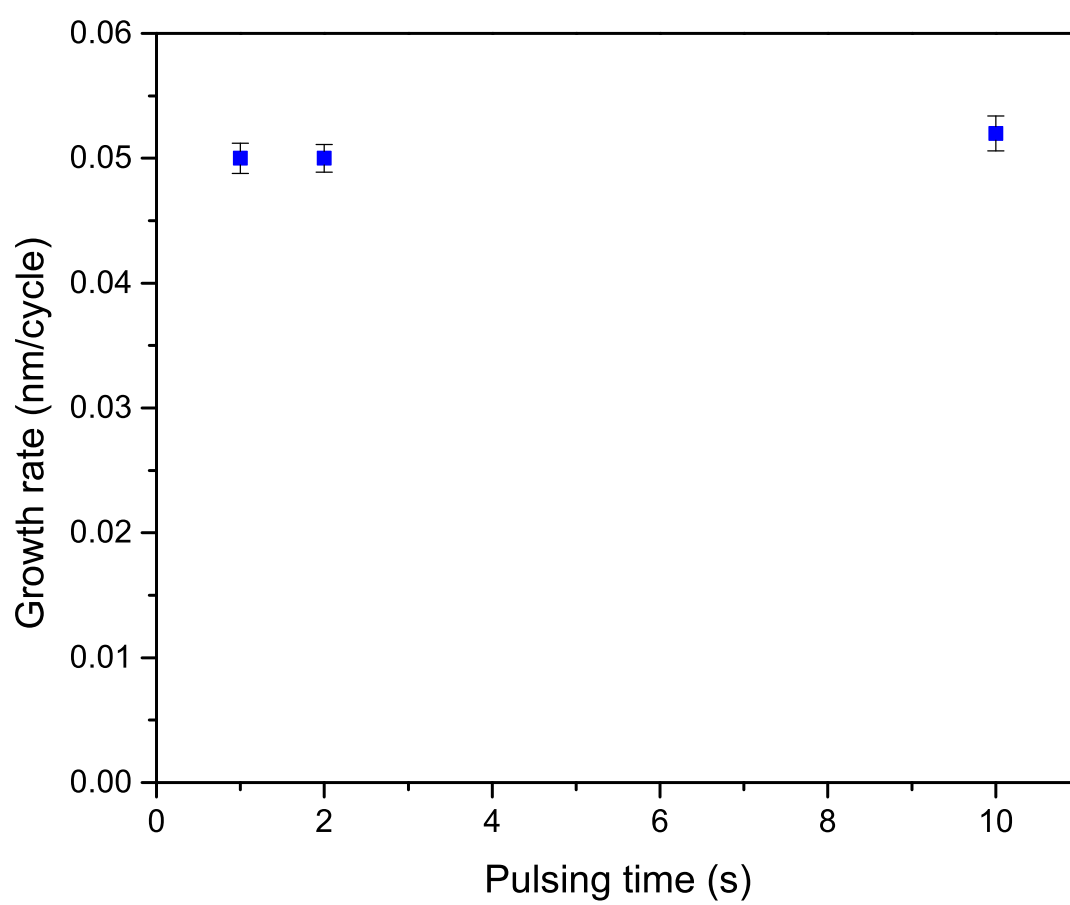


Figure 41: ALD HfO<sub>2</sub> growth rate on Si(100) as a function of oxidizer (ethanol) pulse time.



200 °C is attributed to precursor condensation on the substrate surface. Precursor decomposition at temperatures above 280 °C could have caused multilayer precursor deposition on the substrate surface and resulted in high growth rate beyond 280 °C. The typical ALD working region in between these two high growth regimes where the ALD growth rate is independent of substrate temperature is called ALD temperature window (200-280 °C). Figure 43 shows ALD HfO<sub>2</sub> films deposited with different number of ALD cycles. Linear increase in thickness with increasing number of ALD cycles indicates self-limited ALD growth behavior. The film grew at a rate of 0.05 nm/cycle. The figure also includes the film growth rate of 0.15 nm/cycle using water as the ALD oxygen source. Such lowered growth rate in alcohol based ALD process is observed in other studies using alcohols as the ALD oxygen source too. (10; 5) Other than the attenuated growth rate, the HfO<sub>2</sub> ALD process using ethanol as the ALD oxygen source showed typical ALD growth behavior.

### 3.3.3.2 Compositional Analysis

Figure 44 shows high resolution XPS spectra of 35 nm-thick HfO<sub>2</sub> ALD film on silicon. The film was deposited at 200 °C and subsequently annealed in nitrogen ambient for 5 min at 700 °C. The spectra were taken after sputtering the sample using Ar<sup>+</sup> beam to remove surface contamination. High resolution core spectra of Hf 4f exhibited a single pair of spin orbit doublet (Hf 4f<sub>5/2</sub> at 19.6 eV and 4f<sub>7/2</sub> at 17.9 eV) with spin-orbital splitting of 1.7. (101) No change in peak position or shape was observed before and after Ar<sup>+</sup> beam sputtering. This indicates the presence of same HfO<sub>2</sub> chemical structure at the film surface and in the bulk. The O 1s spectra of the film exhibited a single peak centered at 530.5 eV. This peak is attributed to

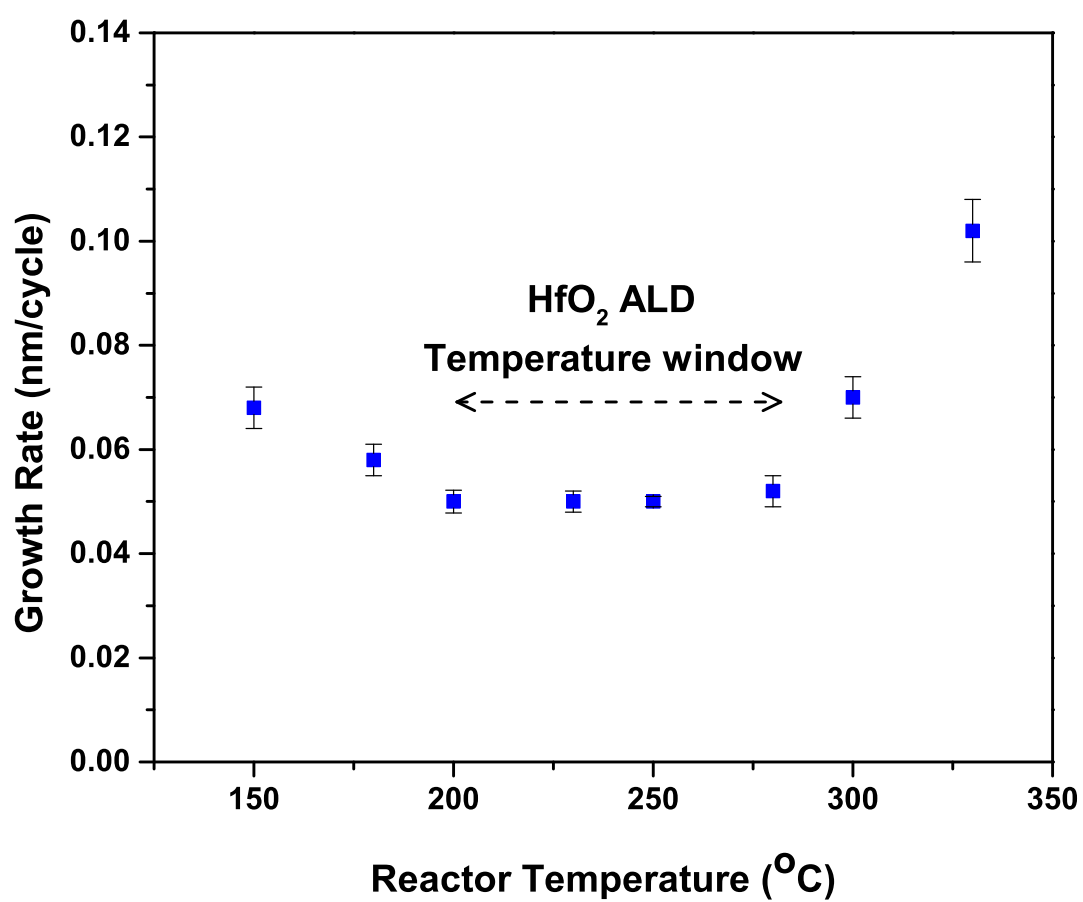


Figure 42: Growth rate of HfO<sub>2</sub> as a function of ALD reactor temperature. ALD cycle times used are 5 s precursor pulse : 15 s purge : 1 s oxidizer pulse : 15 s purge.

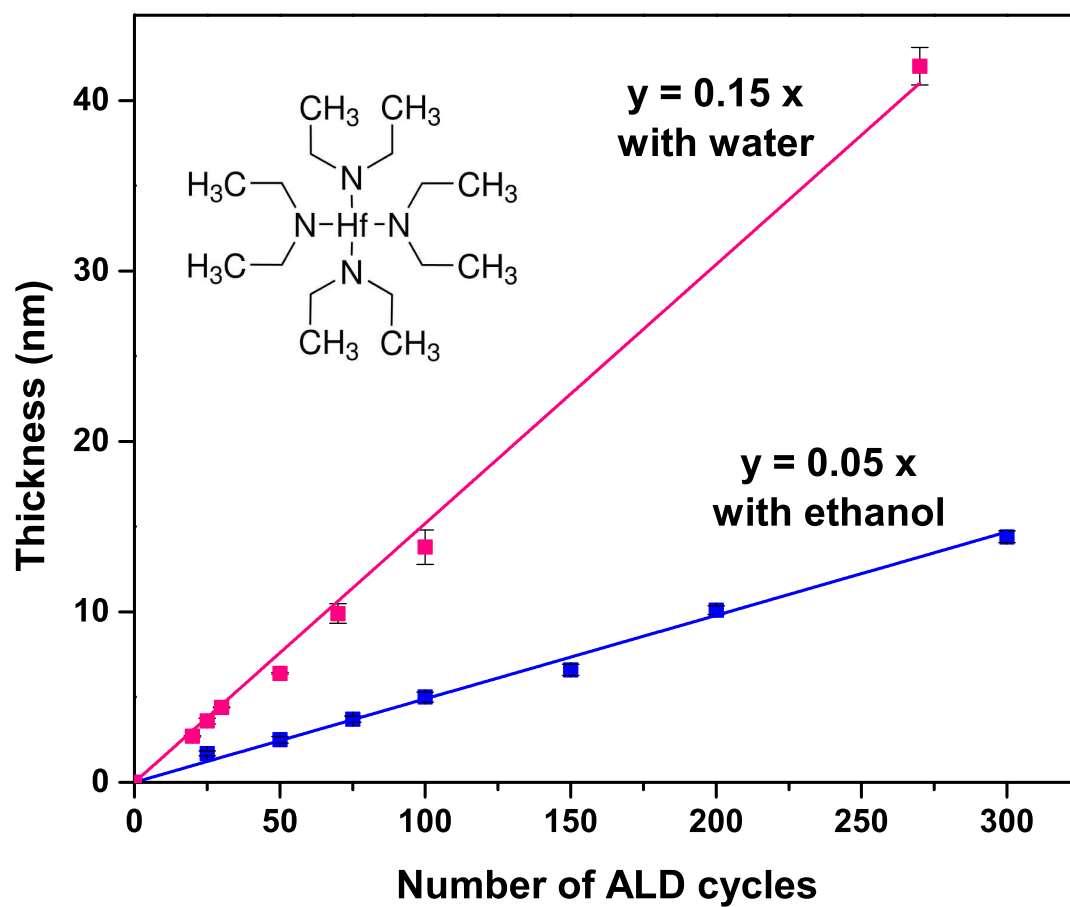


Figure 43: Growth rate of  $\text{HfO}_2$  as a function of number of ALD cycles carried out at 200 °C. Schematic representation of the TDEAH molecule is shown in inset.

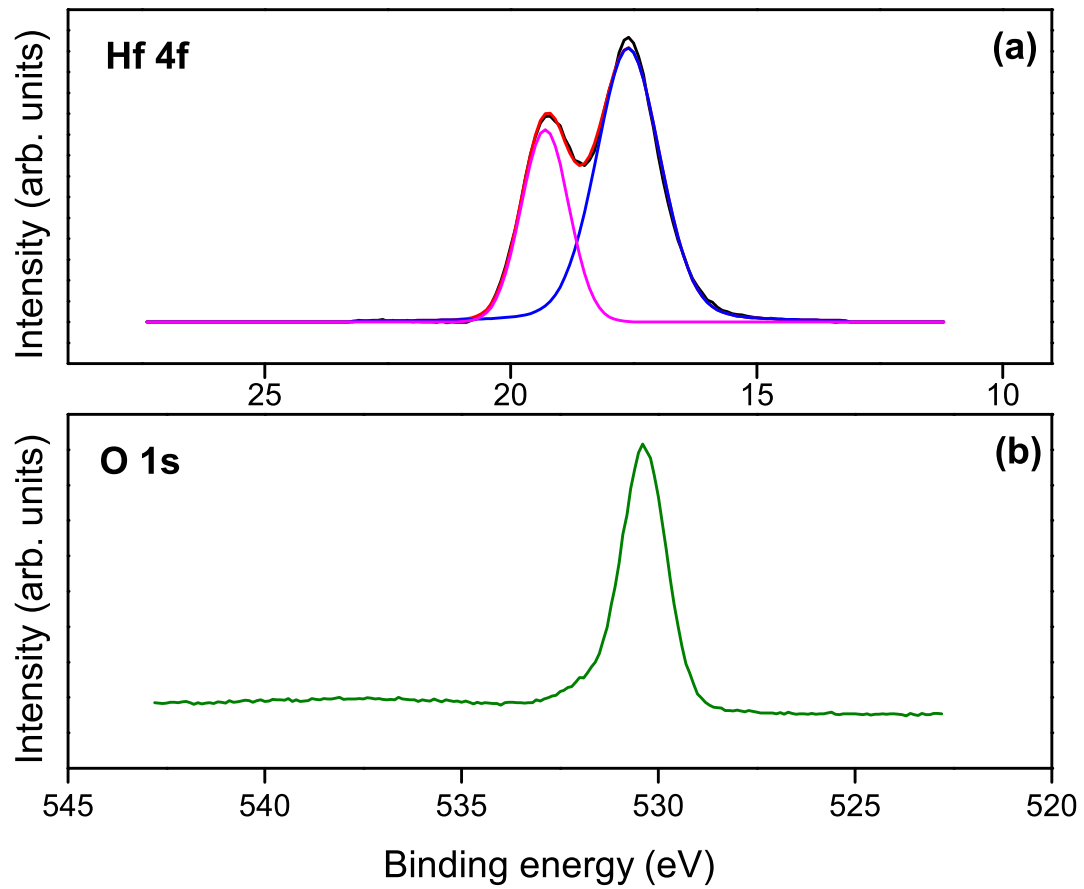


Figure 44: Hf 4f (a) and O 1s (b) core spectra of 35 nm-thick  $\text{HfO}_2$  sample deposited at 200 °C and annealed at 700 °C for 5 min in nitrogen ambient. Spectra were taken after 20 min of  $\text{Ar}^+$  beam sputtering. ALD cycle times used were the same as those in Figure 42.

oxygen in  $\text{HfO}_2$ . Elemental analysis of the  $\text{HfO}_2$  ALD film gave O to Hf atomic ratio of 2.7 before sputtering the sample, 2.4 after 5 min of sputtering and 2.09 after 20 min of sputtering. Once the surface contaminants are sputter-etched, the  $\text{HfO}_2$  ALD film deposited using ethanol showed composition close to its stoichiometric value.

Figure 45 shows C 1s spectra of 35 nm-thick ALD HfO<sub>2</sub> film deposited on silicon substrate. The spectra were taken before and after Ar<sup>+</sup> beam sputtering in order to ascertain the presence and origin of carbon contamination. The sharp peak at 285 eV in the spectra taken before Ar<sup>+</sup> beam sputtering is attributed to adventitious carbon. The adventitious carbon is most likely due to ambient exposure. The carbon contamination at the surface is removed upon sputtering the sample using 200 nA Ar<sup>+</sup> beam for 15 min. After sputtering, the C 1s signal went below the XPS detection limit of 0.5 atom %. The deposition of stoichiometric HfO<sub>2</sub> with such low impurity level indicates the good reactivity of TDEAH with ethanol as it has with other common ALD oxygen sources such as water, oxygen and ozone. Similar results of low impurity level in the ALD HfO<sub>2</sub> using TDEAH and water has been reported earlier. (100; 48)

Interface quality of the films is analyzed by taking high resolution XPS spectra of as-deposited and annealed 4 nm-thick ALD HfO<sub>2</sub> films. The deposition was carried out on HF cleaned Si substrates using ethanol as the ALD oxygen source (Figure 46). Both samples gave the typical bulk silicon doublet at 99.3 and 99.9 eV. The mild feature observed in as-deposited sample Si 2p spectra at 102.4 eV is assigned to silicon sub-oxides formed as a result of HF treatment. (102) The SiO<sub>2</sub> feature typically observed at higher binding energy is not seen in the XPS spectra of as-deposited samples. On the other hand, a strong SiO<sub>2</sub> signal at 102.9 eV is observed in the spectra of annealed sample. This is in agreement with the earlier studies of SiO<sub>2</sub> interface layer formation upon annealing of HfO<sub>2</sub> ALD films. (102) Formation of SiO<sub>2</sub> interfacial layer could have happened either due to the trace amount of oxygen (< 5 ppm) present

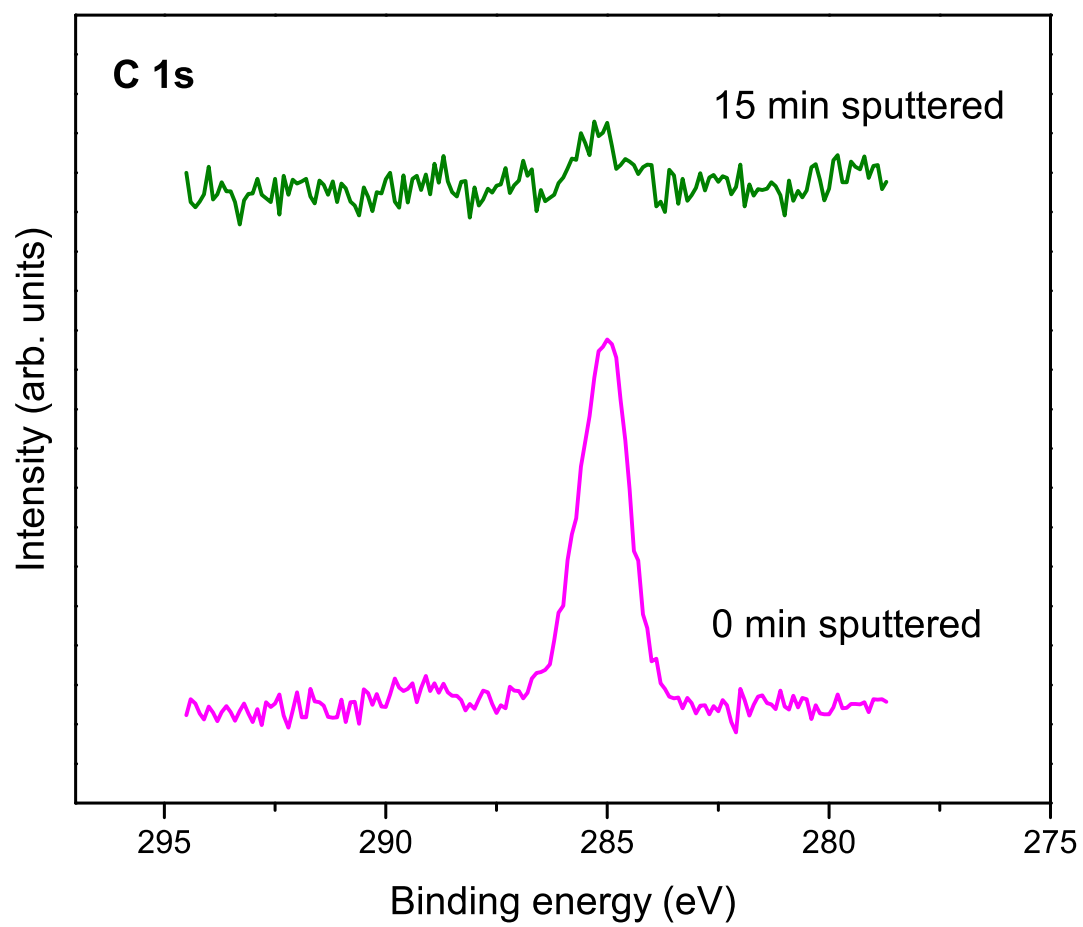


Figure 45: C 1s core XPS spectra showing the removal of surface carbon contamination upon 15 min  $\text{Ar}^+$  beam sputtering.

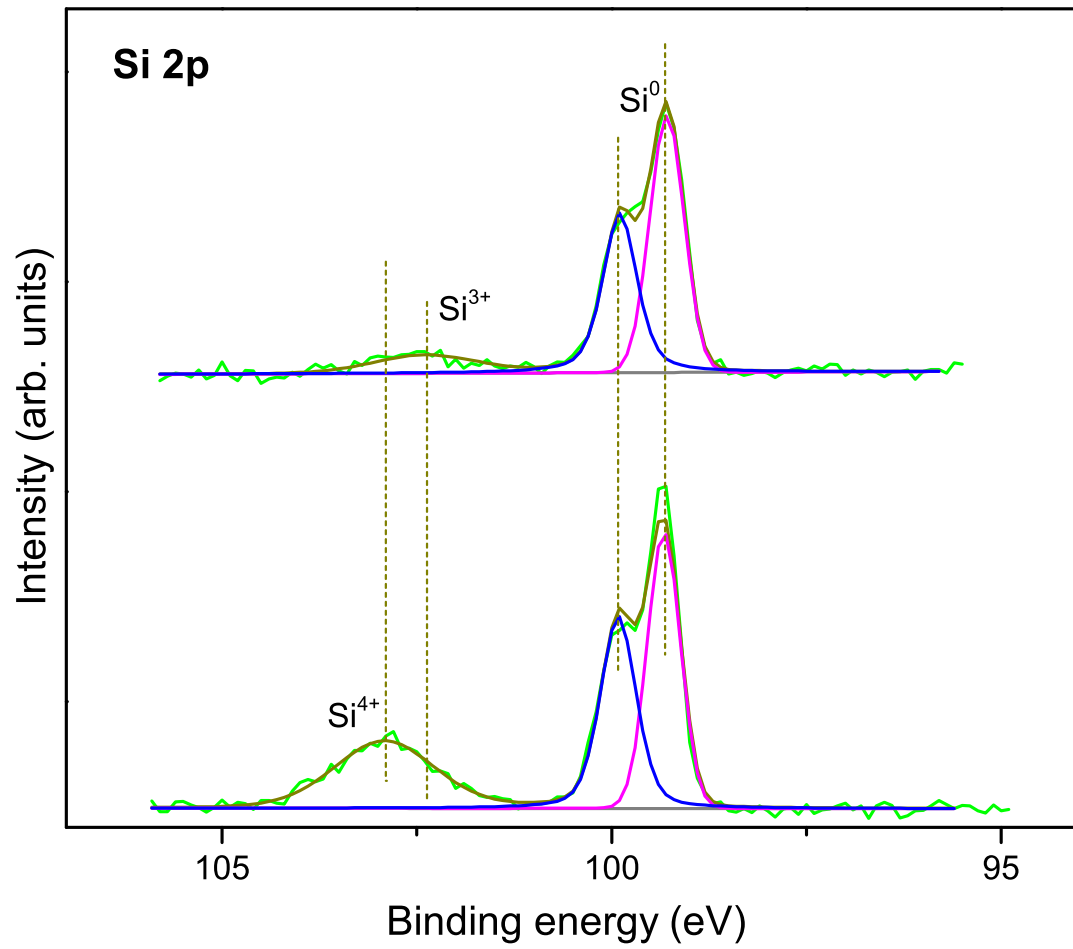


Figure 46: Si 2p core spectra of as-deposited and annealed 4 nm-thick HfO<sub>2</sub> film showing the formation of SiO<sub>2</sub> interface upon high temperature annealing in nitrogen ambient for 5 min.

in the annealing nitrogen gas (103) or segregation of Hf<sub>x</sub>Si<sub>1-x</sub>O<sub>y</sub> layer into SiO<sub>2</sub> and HfO<sub>2</sub>. (99)

### 3.3.3.3 Dielectric Characterization

The effect of the ALD oxygen source on the dielectric behavior of as-deposited and annealed ALD HfO<sub>2</sub> films are studied using C-V and I-V characteristics of Al/HfO<sub>2</sub>/Si capacitors. The dielectric films are 35 nm-thick HfO<sub>2</sub> deposited using ethanol and water as the ALD oxygen sources. C-V curves of films are recorded in the voltage range of +5 to -5 V with 100 kHz ac frequency (Figure 47). The samples showed clear transition from accumulation region through depletion to inversion region. Counter-clockwise hysteresis is observed in both sets of samples, with as-deposited ethanol-based sample showing more pronounced hysteresis of 2.9 V and a flat band voltage of -0.45 V. The presence of horizontal shoulders in the depletion region of the C-V curve indicates high level of interface state density (104). Hysteresis in C-V curve is attributed to the presence of trapped charges in the gate oxide which might be oxygen vacancies or defects formed during the deposition process (35). Flat band voltage of -0.45 V indicates positive charges trapped in the as-deposited ethanol-based ALD film. Such a moderate show of as-deposited ethanol-based samples could be due to the effect of less reactivity of ethanol with H-terminated Si starting surface. HF treated H-terminated Si surface often causes three dimensional growth (105) in HfO<sub>2</sub> ALD and results in modest electrical behavior. The effect is even escalated by the use of ethanol, which doesnt seem to react with H-terminated surface at the processing conditions used. Our earlier experiments of ZrO<sub>2</sub> ALD on H-terminated Si surface yielded no film growth for ~ 50 ALD cycles, indicating the inability/difficulty of ethanol in replacing H-termination at the deposition conditions used; on the contrary, no such nucleation delay was observed in OH-terminated silicon surface. (5) As-deposited water-based sample



showed smooth C-V curve with a smaller hysteresis of 0.2 V and flat band voltage of 0.05 V. Upon high temperature annealing in nitrogen at 700 °C for 5 min, C-V curves of both annealed samples were shifted towards positive bias direction. Annealed ethanol-based sample showed improved C-V curve as compared to as-deposited ethanol-based samples. The hysteresis at flat band reduced to 1.15 V. This could be due to the passivation of trapped charges in the gate oxide or formation of SiO<sub>2</sub> interface. (106) Weak inversion hump observed in inversion region of the annealed ethanol-based sample is attributed to high density of interface states, usually observed in III-V semiconductor stacks. (107) Annealing didn't change the flat band voltage hysteresis in samples deposited using water as the ALD oxygen source.

Figure 48 shows leakage current characteristics of as-deposited and annealed (ethanol and water) samples investigated in the voltage range of -5 to +5V. All samples showed well behaved leakage current characteristics. The as-deposited ethanol-based sample outperformed as-deposited water-based sample by several orders of magnitude lower leakage current in negative bias and about an order of magnitude lower leakage current in positive bias. The as-deposited ethanol-based sample showed leakage current density of  $5 \times 10^{-8}$  A/cm<sup>2</sup> at 1 V. Low leakage current density in as-deposited ethanol-based sample is attributed to amorphous HfO<sub>2</sub> film deposition due to low deposition temperature and the formation of denser film due to the use of ethanol. (10) High temperature annealing in nitrogen ambient increased leakage current in both set of annealed (ethanol and water) samples. This is attributed to the formation of crystalline phase with grain boundaries, which are believed to serve as high leakage paths (108).

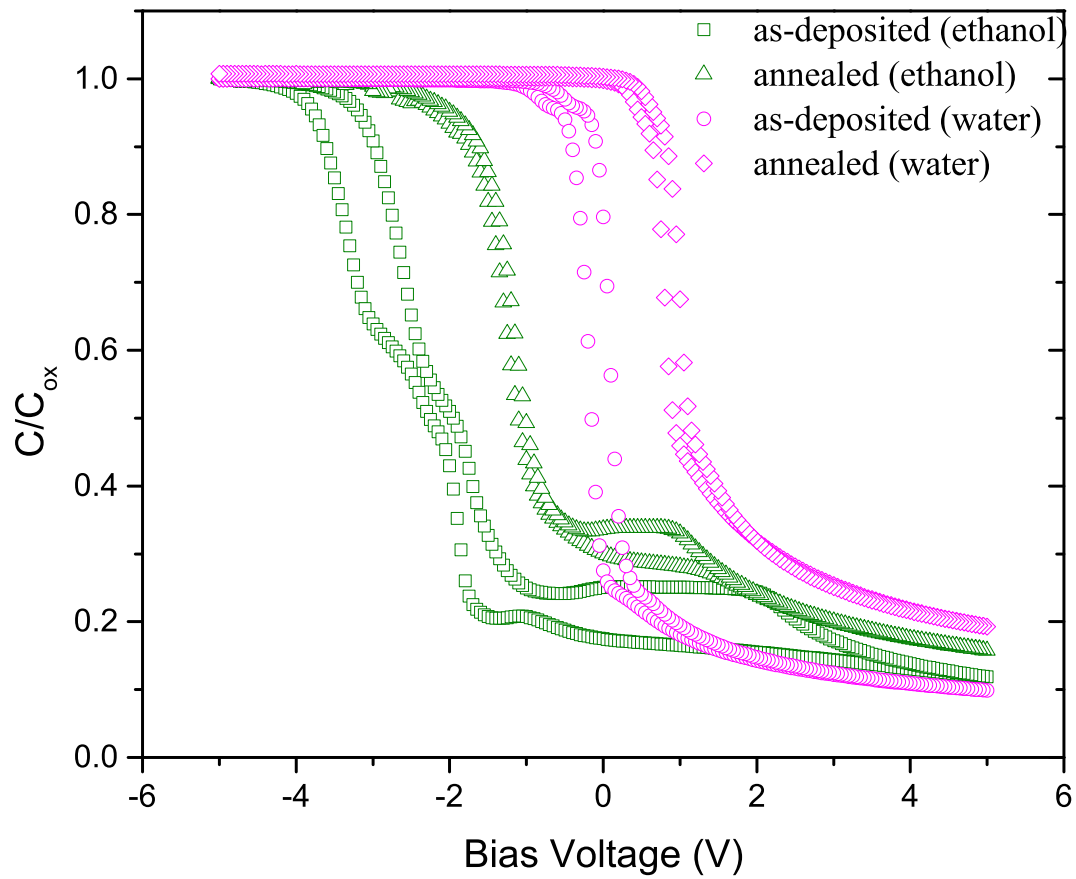


Figure 47: Normalized capacitance-voltage curves of as-deposited and annealed samples prepared using ethanol and water as the ALD oxygen sources. The thickness of films is 35 nm. All other deposition and annealing conditions are the same as those in Figure 44.

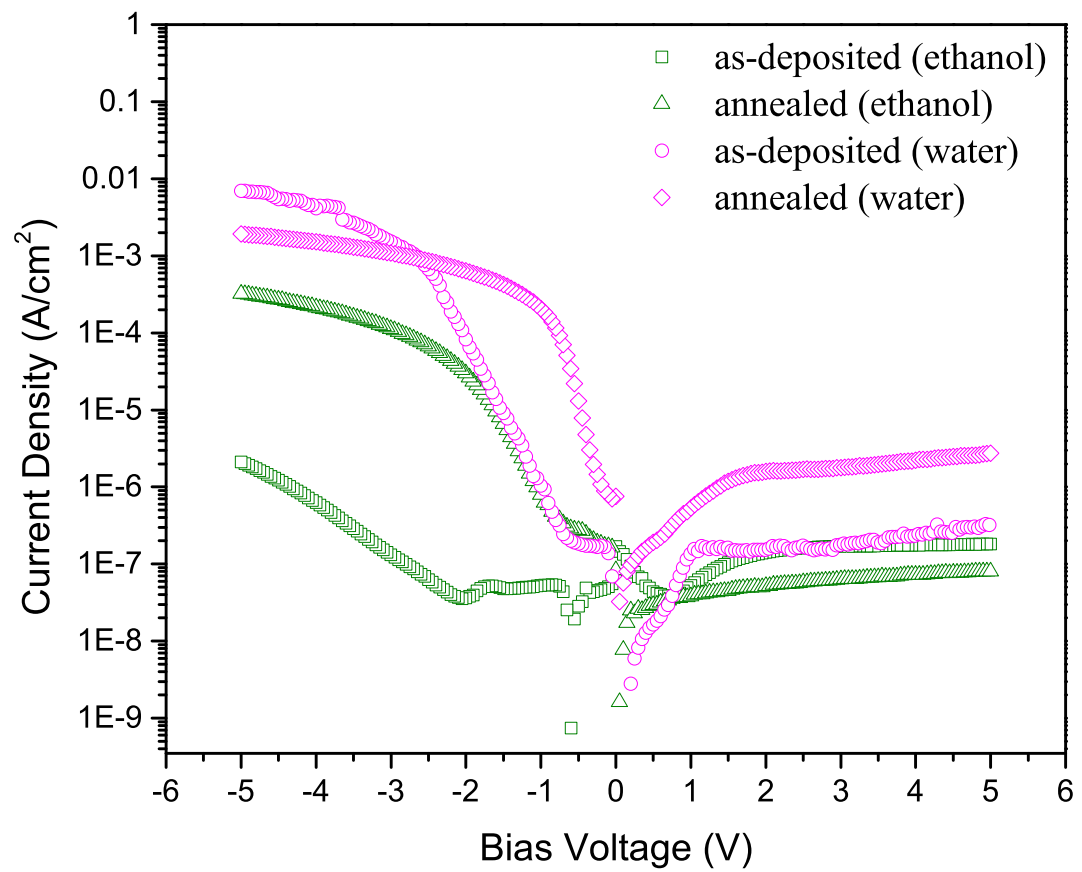


Figure 48: Current-voltage characteristics of 35 nm-thick as-deposited and annealed ALD  $\text{HfO}_2$  deposited using ethanol and water as the ALD oxygen sources. Film deposition and annealing conditions were those mentioned in Figure 44.

### 3.3.4 Summary

In this study, ethanol was successfully used as the ALD oxygen source for the atomic layer deposition of ultra-thin hafnium oxide. Ethanol based ALD process showed typical ALD growth behavior with a wide ALD temperature window from 200-280 °C. HfO<sub>2</sub> ALD films were found to grow at a steady growth rate of 0.05 nm/cycle in the temperature range studied. This growth rate is less than 0.15 nm/cycle found when water was used as the oxidant with the same metal precursor. XPS analyses showed stoichiometric proportion of hafnium to oxygen in HfO<sub>2</sub> ALD film. While, SiO<sub>2</sub> interlayer was not detected in XPS spectra of as-deposited films, sample annealing at 700 °C for 5 min in N<sub>2</sub> ambient triggered SiO<sub>2</sub> IL formation. HfO<sub>2</sub> films showed good dielectric performance, comparable to samples prepared by water based ALD process. Results of this work demonstrate the potential for introducing ethanol as the ALD oxygen source for HfO<sub>2</sub> ALD film deposition for CMOS applications.

## 3.4 ALD of SnTiO<sub>x</sub>

### 3.4.1 Introduction

Titanium dental implants are often used to reinstate intraoral defects such as missing teeth or parts of teeth. These implants are more prone to bacterial infection due to its proximity to oral cavity. Bacterial infection and biofilm formation on the implant surface causes peri-implant diseases such as peri-implant mucositis and peri-implantitis. (109) Peri-implant mucositis is a reversible inflammatory condition of the soft tissues around dental implant. Peri-implantitis is an inflammatory condition that affects jaw bone tissues surrounding the osseointegrated dental implant and results in loss of supporting bone. It affects 20% patients after 5-10 years of

implantation. (110) Bacterial colonization on the implant surface is said to be the major cause for loss of supporting bone around the osseointegrated dental implant. (111) Loss of supporting bone exposes implant surface to oral cavity and accelerates bacterial infection. Untreated peri-implantitis leads to implant loosening and eventual failure. (112) Removal of bacterial deposits from the implant surface is the main step in peri-implantitis and other implant related infection therapies. Non-surgical treatment options for such therapies include the use of antibiotics, antiseptics, mechanical cleansing, laser treatment and UV-irradiation to kill the colonized bacteria. (113) Recent use of nanostructured implant surfaces such as roughened and anodized surfaces (114) shelter microorganisms and make mechanical cleansing, antibiotic and antiseptic therapies less effective. Difficulty in attaching photosensitive dye molecules to implant surface makes laser treatment less common. (115) Use of low intensity UV-radiation seems to be the effective and easier way to disinfect implant surface, owing to the photocatalytic property of titanium implant surface oxide.

The thin surface oxide layer of titanium implant produces reactive oxygen species, such as hydroxyl radical ( $\cdot\text{OH}$ ), superoxide ( $\cdot\text{O}^{2-}$ ), hydrogen peroxide ( $\text{H}_2\text{O}_2$ ), etc., (116) when illuminated with UV. These reactive oxygen species attack and damage bacterial cell wall membrane. Damaged membrane affects normal cell functions such as respiration and semi-permeability and causes cell death. (117) The disinfecting activity of  $\text{TiO}_2$  films can be improved by thickness, structural and compositional modifications. In this project, we studied the effect of tin (Sn) doping in the antibacterial activity of  $\text{TiO}_2$  films. Tin doping helps reduce recombination rate

of holes and electrons, there by increases the generation of reactive oxygen species. (118)

TiO<sub>2</sub> thin films have been deposited by different techniques such as, thermal oxidation, sol-gel, anodic oxidation, chemical vapor deposition, atomic layer deposition (ALD) etc. (119; 120; 121; 116) Among these, thermal oxidation and ALD form conformal layers on nanostructured surfaces. Thermal oxidation of titanium alloy (Ti-6Al-4V) causes segregation of alloy constituents (Aluminum and Vanadium) to the surface and it leads to oxide layer with aluminum concentration two- to three-fold higher than that in the bulk. (122) Thus in this work, ALD is used to deposit thin layers of Sn-doped TiO<sub>2</sub> on Ti-6Al-4V (Ti-V) surface. ALD is a thin film deposition technique in which saturated exposure of a substrate surface to precursor and oxidizer molecules in discrete cyclic manner deposits thin films in layer by layer fashion. Layer by layer deposition of the thin film provides unprecedented control over thickness and composition down to Ångstrom length scale. ALD deposits pin-hole free, conformal films on 3D nanostructures with less impurity content. (47) This deposition technique can easily be scaled up to high-volume production of nano-structured implants.

In this study, ALD is used to deposit thin films of Sn-doped TiO<sub>2</sub>. Most of the earlier studies on Sn-doped TiO<sub>2</sub> films used glass or ceramic substrates. (123; 124; 125; 126) Band energy level positioning of substrate with the film plays pivotal role in the activity of the photocatalytic film. (127) Thus, the more relevant bioimplant material, Ti-V itself was used to study the efficacy of ALD coating. Tin composition in the film was varied from 0% to 75% to study

the effect of tin doping on film property. X-ray photoelectron spectroscopy (XPS) was used to probe the film composition and purity. A low intensity UV light was used to activate the Ti-V surface for photoactivated antibacterial activity tests. The antibacterial study was performed against *Escherichia coli* (e-coli) bacteria. Viable bacteria were analyzed using agar diffusion method.

### **3.4.2 Materials and Methods**

Ultra-thin films of Sn-doped  $\text{TiO}_2$  was deposited on Ti-V alloy disks (McMaster-Carr, IL, USA) of 1.5 cm diameter and 0.1 cm thickness. The samples were polished (roughness  $10 \pm 2$  nm), washed with deionized water (resistivity  $\geq 17 \text{ M}\Omega \text{ cm}$ ) and blown dried with nitrogen (99.998% purity) prior to the ALD process. ALD on these samples were carried out using a custom-built flow type ALD reactor. (1) Tetrakis(diethylamino)titanium (TDEAT) kept at  $65^\circ\text{C}$  and tin(II)acetylacetonate ( $\text{Sn}(\text{acac})_2$ ) kept at  $70^\circ\text{C}$  were used as titanium and tin sources, respectively. Ozone ( $\sim 1000$  ppm) was used as the ALD oxygen source. One  $\text{TiO}_2$ -ALD cycle consists of 8 s TDEAT exposure followed by 25 s  $\text{N}_2$  purging, 1 s ozone exposure and 15 s  $\text{N}_2$  purging.  $\text{SnO}_x$ -ALD cycle was performed by 6 s  $\text{Sn}(\text{acac})_2$  exposure followed by 25 s  $\text{N}_2$  purging, 1 s ozone exposure and 15 s  $\text{N}_2$  purging. Different composition of tin doping was achieved by changing the number of  $\text{SnO}_x$ -ALD cycles with respect to  $\text{TiO}_2$ -ALD cycles. Five different tin compositions (0, 15, 30, 50 and 75%) were tried in this study. Uncoated Ti-V disk was used as control sample. All other samples were coated with 300 ALD cycles of  $\text{TiO}_2$  and different number of  $\text{SnO}_x$ -ALD cycles depending on the required tin percentage. This experimental design ensures equal amount of  $\text{TiO}_2$  (300 ALD cycles) in all the samples. The deposition

process is sequenced to get  $\text{TiO}_2$  as the outermost layer. Spectral ellipsometry (model 44, J.A. Woollam Co. Inc.) was used to measure the thickness of the deposited film. Chemical composition and elemental analysis of the Sn-doped  $\text{TiO}_2$  films were probed with high resolution XPS (Kratos AXIS 165, Kratos Analytical Ltd.) equipped with monochromatic Al  $K\alpha$  X-ray source (1486.6 eV) operating at 12 kV and 10 mA. Photoactivated antibacterial property of the films was studied using a gram negative e-coli bacterial strain ATCC 8739 (Microbiologics Inc.). Gram negative bacteria was used as failing implants were found to have mostly gram-negative bacterial species. (128) Antibacterial test was carried out by immersing the Ti-V samples in bacterial suspension solution ( $2 \times 10^7$  CFU/ml) and exposing them to low intensity UV ( $330 \mu\text{W}/\text{cm}^2$ ) (15 W Philips TUV 15W/G15 T8) for 3 min. The bacterial solution was then diluted to  $10^{-2}$ . 20  $\mu\text{L}$  of the diluted bacterial suspension was plated on agar plate (Lennox L Agar, Alpha Biosciences Inc.) and incubated at  $37^\circ\text{C}$  for 12 hours to count the number of viable bacterial colonies.

### **3.4.3 Results and Discussion**

ALD reactor operating conditions were initially optimized to get self-saturated growth of  $\text{TiO}_2$  and  $\text{SnO}_x$  on Si(100) substrate as described in our earlier reports. (1; 3) Figure 49 shows  $\text{TiO}_2$  and  $\text{SnO}_x$  film thickness as a function of ALD cycle numbers. It is evident from the graph that both films grow linearly with respect to ALD cycle numbers. This linear growth indicates surface saturated ALD growth behavior.  $\text{TiO}_2$  and  $\text{SnO}_x$  films grew at a constant rate of 0.05 and 0.1 nm/cycle respectively. This ALD growth behavior is maintained within  $175\text{--}275^\circ\text{C}$  for  $\text{TiO}_2$  and  $175\text{--}300^\circ\text{C}$  for  $\text{SnO}_x$  -ALD processes. Deposition of Sn-doped  $\text{TiO}_2$



was performed at 200 °C which is within these overlapping temperature windows. Optimized ALD growth parameters and processing conditions were used to grow Sn-doped TiO<sub>2</sub> thin films on Ti-V disks. Layer by layer deposition facilitates precise thickness control. Such control on film thickness can be used to deposit films thick enough to have high photocatalytic property and thin enough to preserve nano-morphological features of the implant surface.

Figure 50 shows XPS spectra of 50% Sn-doped TiO<sub>2</sub> film. XPS survey spectra (Figure 50(a)) peaks show the presence of tin, titanium, oxygen and trace amount of carbon. Absence of other elements such as chlorine and nitrogen indicate clean deposition as typically observed in ALD processes. (35; 36; 1; 34) Further spectra were taken around the observed elements at high resolution (Figure 50(b)-(e)) to identify its chemical nature. High resolution XPS spectra of Ti 2p (Figure 50(b)) has two peaks at 462.7 eV (2p<sub>1/2</sub>) and 457 eV (2p<sub>3/2</sub>). These peaks match with TiO<sub>2</sub> XPS spectra in the literature. (129) The high resolution XPS of Sn (3d<sub>3/2</sub> 495 eV and 3d<sub>5/2</sub> 486.6 eV) has full width half maximum of 1.2 (Figure 50(c)). This indicates the presence of Sn in single oxidation state, which would be SnO<sub>2</sub> due to the use of strong ALD oxidizer. Oxygen peak location at 530.7 eV (O 1s) is also typical to O 1s in TiO<sub>2</sub> and SnO<sub>x</sub>. (69; 129) O 1s peak was recorded after sputtering off the surface contaminants to probe oxygen in the film bulk. Figure 50(e) indicates the carbon contamination. This surface carbon contamination (C 1s 285 eV) is attributed to ambient exposure during the sample transfer from ALD chamber to XPS chamber. Surface contamination was sputtered out in the XPS chamber using 200 nA Ar<sup>+</sup> beam. After sputtering the surface, the film had about 4% of carbon in its bulk. This

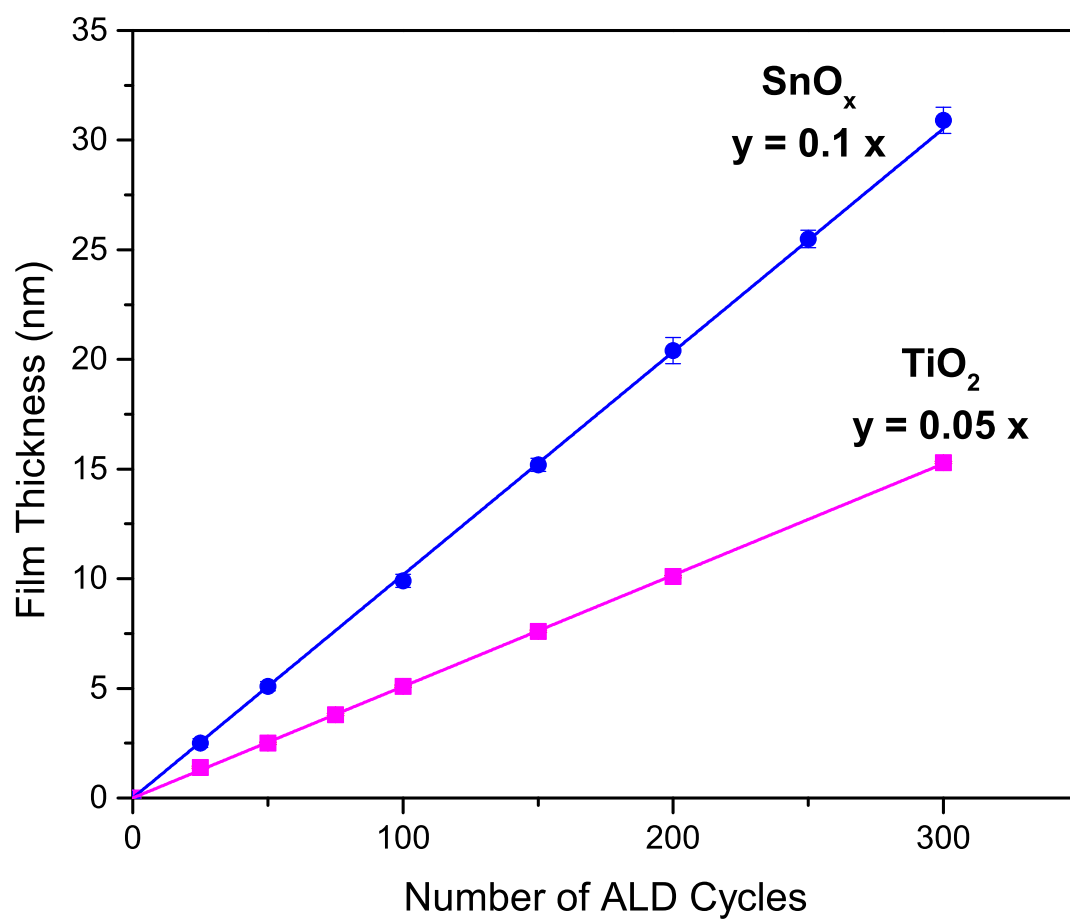


Figure 49:  $\text{TiO}_2$  and  $\text{SnO}_x$  film thickness as a function of number of ALD cycles carried out at 200 °C on silicon(100) substrate. TDEAT and  $\text{Sn}(\text{acac})_2$  were used as titanium and tin sources, respectively. ALD reactor pressure was kept at 0.5 Torr.

purity is better than the Sn-doped  $\text{TiO}_2$  films deposited by other methods reported earlier for photoactivated antibacterial application. (125) Elemental analysis was performed using high resolution XP spectra of Ti 2p and Sn 3d to find the atomic percentages of Sn and Ti in the films. Elemental analysis showed gradual increase in Sn percentage in the film with increase in  $\text{SnO}_x$ -ALD cycle ratio. This demonstrates precious composition tunability of the ALD process. Composition tunability is crucial in tuning band gap of the film, there by its photo-induced antibacterial property.

Figure 51 shows the amount of viable bacterial colonies on control sample (Ti-disk) and on ALD coated Ti-V disk samples after 3 min of UV exposure. Control sample killed 90% of bacteria after the UV exposure. The Ti-V control sample has typically  $\sim 1\text{-}3$  nm thick native oxide layer. The photocatalytic activity of native oxide could be responsible for photoactivated bacterial killing. (115; 130) The lower activity is attributed to thickness and quality of the native oxide layer. (131; 132) Unlike thermally oxidized  $\text{TiO}_2$  film which showed no improvement in antibacterial activity, (130) ALD- $\text{TiO}_2$  coated sample showed marked improvement in antibacterial activity. Bacteria viability came down from 10% in control sample to 5% in ALD- $\text{TiO}_2$  treated sample. Improved activity is attributed to the deposition of high-purity ALD- $\text{TiO}_2$  film. This ALD- $\text{TiO}_2$  film when doped with different amount of tin showed further improvement in anti-bacterial performance. Sn-doped  $\text{TiO}_2$  samples killed most of the bacteria and had only  $\sim 1.5\%$  of viable bacteria after UV irradiation. This is due to the efficient separation of photoactivated holes and electrons or increased band gap. (118) The activity re-

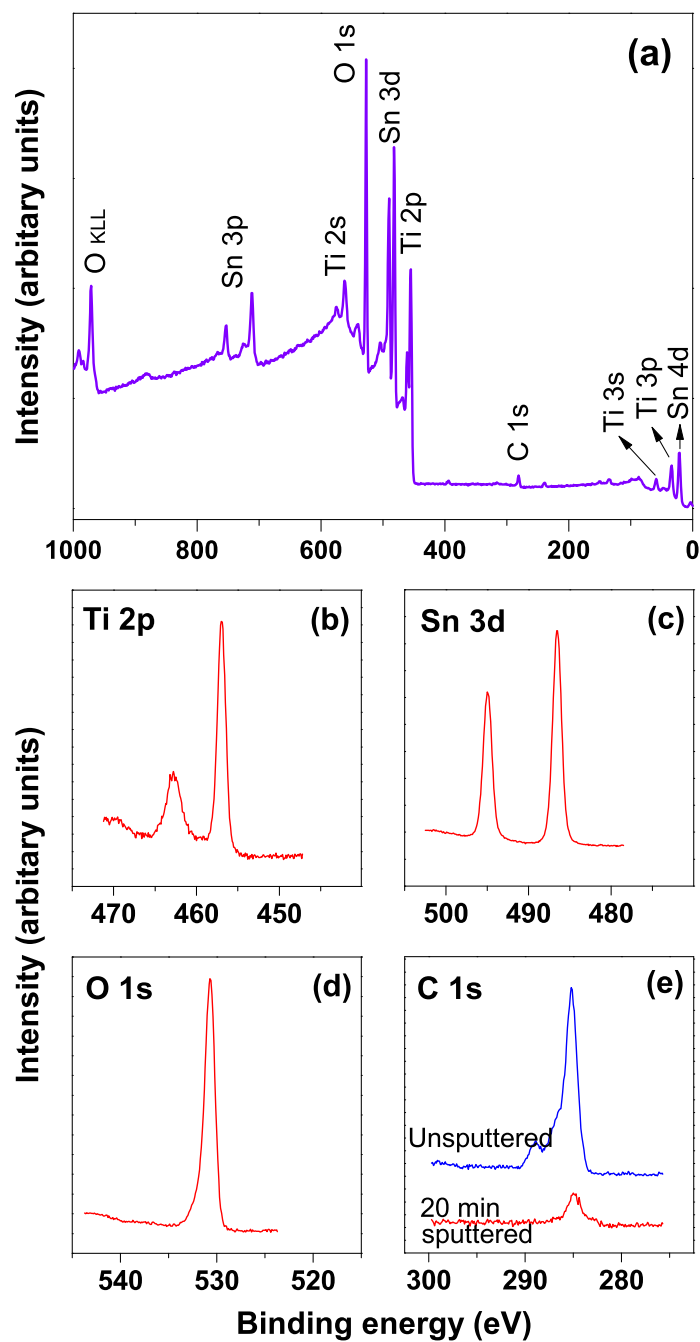


Figure 50: XPS survey (a), Ti 2p (b), Sn 3d (c), O 1s (d) and C 1s (e) spectra of 50% Sn doped  $\text{TiO}_2$  thin film deposited at 200 °C showing contamination-free clean film with appropriate chemical nature.

mained nearly same upon increasing the tin concentration up to 75%. This suggests that even 15% tin is enough to get the beneficial property of tin doping. In the presence of Sn-doped  $\text{TiO}_2$  coated sample, bacteria were killed at a rate of 18 million/min- $\text{cm}^2$  of implant surface. Figure 52 shows representative pictures of the survived bacterial colonies plated on Agar and incubated for 12 hrs at 37 °C. UV irradiation time used in this study is an order of magnitude less than that of other reported studies for the disinfection of implant surface. (115; 133) However, further improvement in surface preparation is needed to reduce the exposure time to below permissible exposure limit of  $\sim 18$  s at the intensity used in this study. (134) Visible light activated photocatalytic coating would be another alternative for implant disinfection without having any deleterious effect on surrounding host tissues. These avenues will be explored using our newly developed ALD surface modification technique in future research for photoactivated disinfection of dental and other biomedical implants.

#### **3.4.4 Summary**

ALD is used to deposit ultra-thin films of Sn-doped  $\text{TiO}_2$  on Ti-V surface for photoactivated disinfection of biomedical implants. Films of different composition were deposited by changing the ALD cycle ratio of  $\text{SnO}_x$ . XPS elemental analysis showed the deposition of contamination-free Sn-doped  $\text{TiO}_2$  films. Antibacterial analysis of the films showed improved activity on  $\text{TiO}_2$  ALD film samples than the Ti-V control sample. Significant additional improvement in activity was observed upon tin doping. Up to 98.5% disinfection was observed with Sn-doped  $\text{TiO}_2$  film sample. The photoactivated disinfection activity remained the same upon

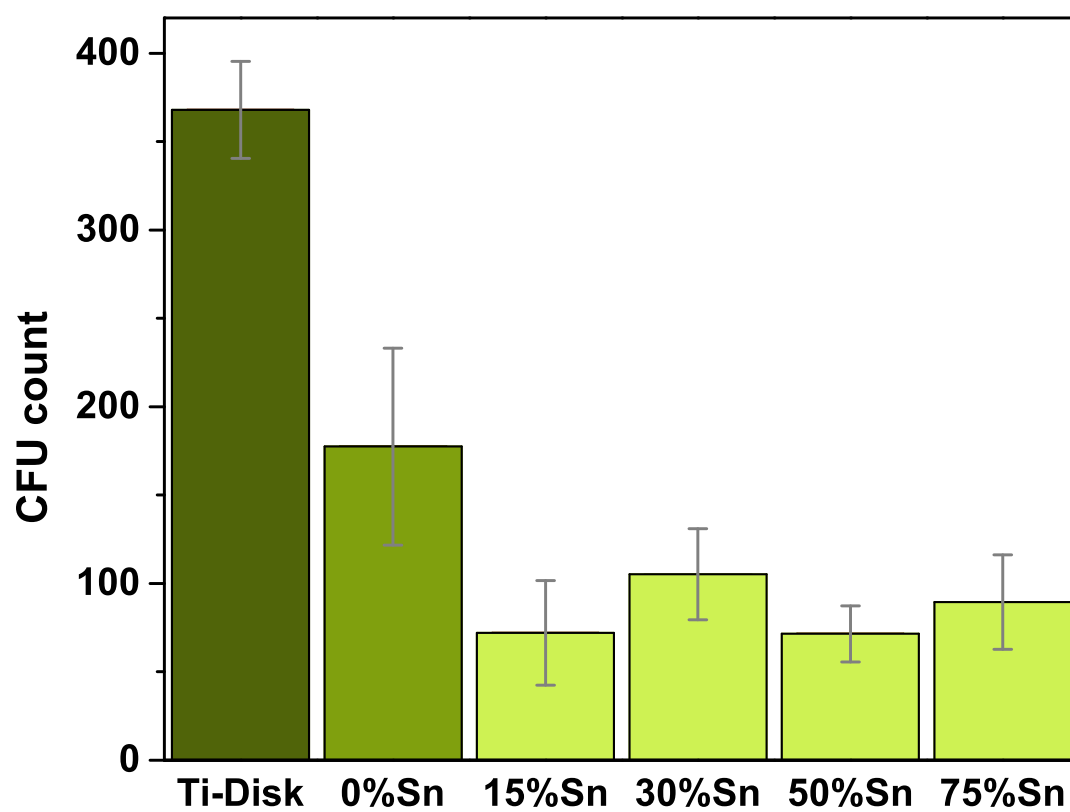


Figure 51: The number of survived e-coli bacteria in six groups after 3 min of UV exposure. The bar graph values represent mean values of six experiments and the error bar indicates standard deviation.

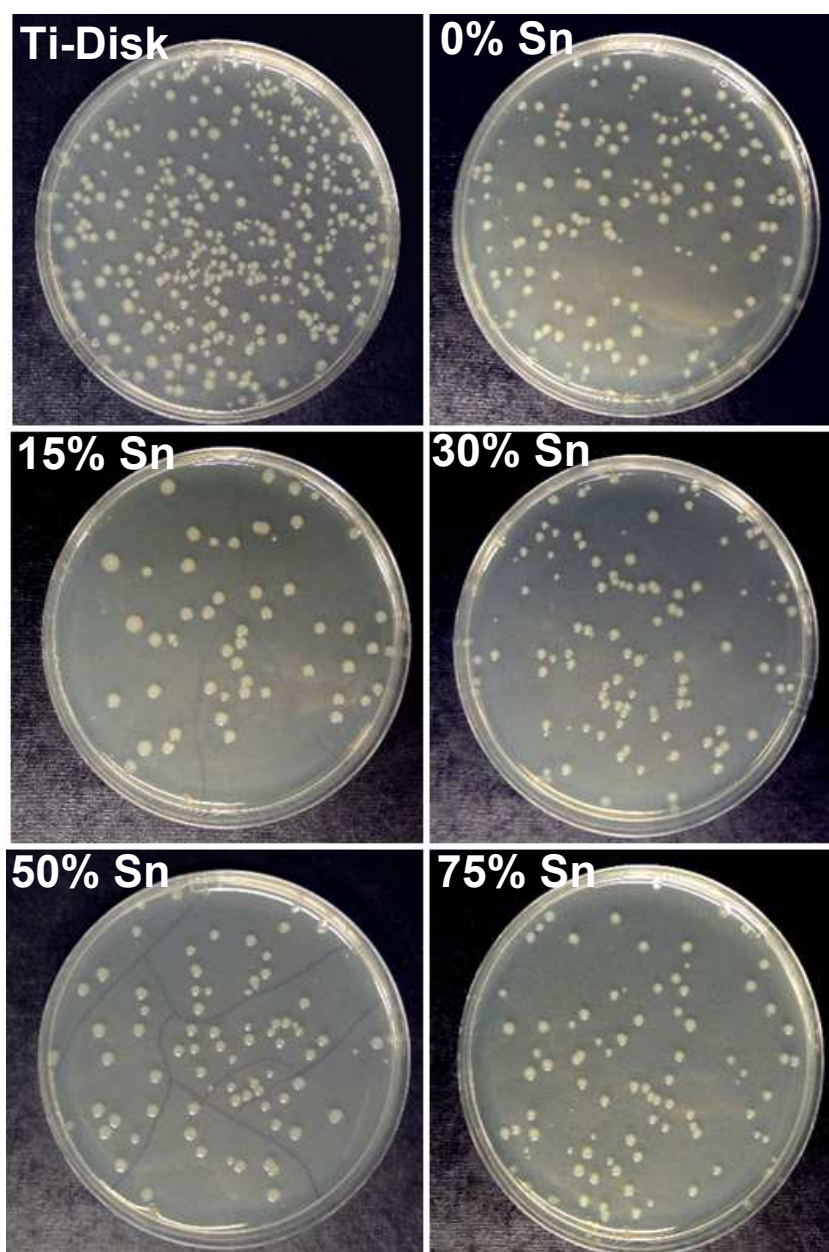


Figure 52: Representative pictures of survived e-coli bacterial colonies in six experimental groups. Inoculated agar plates were incubated at 37 °C for 12 hrs.

increasing the tin concentration beyond 15%. The results of this study show the potential of using atomic layer deposited Sn-doped  $\text{TiO}_2$  (i.e., mixed metal oxide nanofilm in general) for enhanced photoactivated disinfection of nano-structured biomedical implants for antibacterial implant therapies.



## CHAPTER 4

### CONCLUSION AND FUTURE WORK

[Part of this chapter is adapted from my published manuscripts. (1; 2; 3; 4; 5)]

#### 4.1 Conclusion

The conclusion is divided into six sections. First two sections conclude the two projects mentioned in Chapter 2. Following four sections conclude the projects described in Chapter 3.

##### 4.1.1 Design of portable ALD/CVD hybrid system

A portable ALD/CVD hybrid reactor is designed, fabricated and successfully tested. Unique feature of this reactor is the use of ALD/CVD mode in a single portable deposition system to fabricate multi-layer thin films over a broad range from 'bulk-like' multi-micron to nanometer atomic dimensions. The precursor delivery system and control-architecture are designed so that continuous reactant flows for CVD and cyclic pulsating flows for ALD mode are facilitated. A custom-written LabVIEW program controls the valve sequencing to allow synthesis of different kinds of film structures under either ALD or CVD mode or both. The entire reactor set-up weighs less than 40 lbs & has a relatively small footprint of 8 x 9 in., making it compact and easy for transportation. The reactor is tested in the ALD mode with titanium oxide ( $\text{TiO}_2$ ) ALD using tetrakis(diethylamino)titanium (TDEAT) and water vapor.  $\text{TiO}_2$  ALD results demonstrate thickness tunability of the reactor for ALD deposition. The resultant film was analyzed with XPS and found to be stoichiometric  $\text{TiO}_2$  with a trace amount of carbon.

ALD growth rate and film purity are in good agreement with literature values. The ALD/CVD hybrid mode was demonstrated with ALD of  $\text{TiO}_2$  and CVD of tin oxide ( $\text{SnO}_x$ ). Deposition of ALD- $\text{TiO}_2$ /CVD- $\text{SnO}_x$  hybrid films proved the ability of the reactor to deposit thick-thin nano-laminate structures without vacuum break. Transmission electron microscopy images of the resulting film confirms the formation of successive distinct  $\text{TiO}_2$ -ALD and  $\text{SnO}_x$ -CVD layers.

#### **4.1.2 Scalable control program for the hybrid system**

In this project, a scalable control program is designed and implemented in LabVIEW programming environment to control flow type ALD reactor with multiple precursor delivery lines. The program logic is written and tested in LabVIEW environment to control ALD reactor with four precursor delivery lines to deposit up to four layers of different materials in cyclic manner. The programming logic is conceived such that to facilitate scale up for depositing more layers with multiple precursors and scale down for using single layer with any one precursor in the ALD reactor. The program takes precursor and oxidizer exposure and purging times as input and controls the sequential opening and closing of the valves to facilitate the complex ALD deposition process in cyclic manner. The program could be used to deposit materials from any single line or in tandem with other lines in any combination and in any sequence. It is this versatility and scalability that makes this program useful and easily adaptable for similar ALD systems.

### 4.1.3 ALD of SnO<sub>x</sub>

In this work, a novel liquid tin(II) precursor, tin(II)acetylacetonate (Sn(acac)<sub>2</sub>), was used to deposit tin oxide films on Si(100) substrate, using the hybrid reactor. Three different oxidizers, water, oxygen and ozone were tried. Resulting growth rates were studied as a function of precursor dosage, oxidizer dosage, reactor temperature and number of ALD cycles. The film growth rate was found to be  $0.1 \pm 0.01$  nm/cycle within the wide ALD temperature window of 175-300 °C using ozone; no film growth was observed with water or oxygen. Characterization methods were used to study the composition, interface quality, crystallinity, microstructure, refractive index, surface morphology and resistivity of the resulting films. X-ray photoelectron spectra showed the formation of a clean SnO<sub>x</sub>-Si interface. As-deposited films were found to be amorphous with no formation of SiO<sub>2</sub> or other undesirable interfacial reaction products at the interface with silicon. Annealed films showed crystalline features that corresponded to SnO<sub>2</sub>, with simultaneous silicon oxide formation at the interface. Surface morphology studies of films showed fairly smooth films (RMS roughness of 0.9 nm) with a slight increase in roughness upon high temperature annealing. The resistivity of the SnO<sub>x</sub> films was calculated to be 0.3 Ω-cm. Results of this work demonstrate the possibility of introducing Sn(acac)<sub>2</sub> as tin precursor to deposit conducting ALD SnO<sub>x</sub> thin films on a silicon surface, with clean interface and no formation of undesired SiO<sub>2</sub> or other interfacial reaction products, for transparent conducting oxide applications.

#### 4.1.4 Selective ALD of ZrO<sub>2</sub>

SALD of ZrO<sub>2</sub> was carried out on copper patterned silicon substrates using a new chemical approach. Instead of using common ALD oxygen sources like water, oxygen or ozone, we used ethanol, which served as oxygen source for ALD deposition on the silicon side and as effective reducing agent on the copper side, thereby selectively depositing ZrO<sub>2</sub> film on the silicon surface of the substrate without any deposition on copper. ZrO<sub>2</sub>-ALD films on the silicon side of the substrate followed the typical ALD linear growth pattern with a growth rate of 0.04 nm/cycle at 200 °C without an apparent growth delay, whereas technologically significant growth delay was observed on the copper side of the substrate. XPS analysis showed no ZrO<sub>2</sub> growth at least up to 70 ALD cycles on the copper surface. Copper diffusion barrier characteristics of the resulting ZrO<sub>2</sub> film were studied using Cu/2 nm-thick ZrO<sub>2</sub>/Si structures. The ZrO<sub>2</sub>-ALD films were found to withstand temperatures at least as high as 700 °C. Besides improved diffusion barrier characteristics of the ZrO<sub>2</sub>-ALD films, the use of ethanol showed significant improvement in selectivity.

#### 4.1.5 ALD of HfO<sub>2</sub> using ethanol

In this study, ethanol was successfully used as the ALD oxygen source for the atomic layer deposition of ultra-thin hafnium oxide. Ethanol showed good reactivity with the hafnium precursor, tetrakis(diethylamino)hafnium and displayed typical linear film growth behavior within a wide ALD process temperature window (200-280 °C). The ethanol-based ALD process exhibited HfO<sub>2</sub> growth rate of 0.05 nm/cycle which was less than 0.15 nm/cycle obtained when water was used as the ALD oxygen source. XPS showed the deposition of stoichiometric HfO<sub>2</sub> with

trace amount of carbon in the film. SiO<sub>2</sub> interfacial layer was not observed in as-deposited samples, whereas annealed samples showed SiO<sub>2</sub> XPS features. Films prepared using the ethanol based ALD process showed comparable dielectric performance to that of water based ALD process films and displayed well behaved C-V and I-V curves with as-deposited ethanol based HfO<sub>2</sub> samples showing the lowest leakage current density of  $5 \times 10^{-8}$  A/cm<sup>2</sup> at 1 V gate bias.

#### **4.1.6 ALD of SnTiO<sub>x</sub>**

In this project, ALD was used to deposit ultra-thin films (~15 nm) of photoactive tin-doped titanium oxide on medically relevant titanium type-V alloy (Ti-6Al-4V), for peri-implantitis and other implant related infection therapies. Precise thickness and composition tunability of thin films were achieved using the novel ALD process. TiO<sub>2</sub> and SnO<sub>x</sub> films were found to grow at a constant rate of 0.05 and 0.1 nm/cycle, respectively. Antibacterial analysis of the films showed improved activity on TiO<sub>2</sub> ALD film samples than the Ti-V control sample. Progressive improvement in antibacterial activity was observed from bare Ti-V disk to TiO<sub>2</sub> coated disk and Sn-doped TiO<sub>2</sub> coated disks. 15% Sn-doped TiO<sub>2</sub> coated disk was found to kill 98.5% of bacteria within 3 min of low intensity UV exposure. The killing rate was calculated to be 18 million/min-cm<sup>2</sup> of implant surface. The results of this study show the potential of using atomic layer deposited Sn-doped TiO<sub>2</sub> (i.e., mixed metal oxide nanofilm in general) for enhanced photoactivated disinfection of nano-structured biomedical implants for implant related infection therapies.

## **4.2 Future Work**

### **4.2.1 SALD of metal oxides and metals**

Many thin film applications demand the films to be selectively deposited on specific surfaces. In microelectronics industry, such patterning is traditionally performed using photolithography. Photolithography step involves several pre- and post-processing steps. The continuously shrinking feature dimensions in microelectronic industry require more efficient nano-patterning. ALD offers a novel method in nano-patterning. ALD film deposition depends mainly on surface nucleation sites. Modification in the surface functional group leads to enhanced/suppressed/no film growth. This unique property of the ALD technique can be used for SALD. In this thesis, a pilot study on the use of ethanol for SALD process was investigated. The SALD was achieved without the use of a self-assembled monolayer, soft lithography, a scanning tunneling microscopy tip or other surface modifications. Even though the ethanol based SALD was able to inhibit ALD growth on metal surface up to 70 ALD cycles, the process needs to be studied at different temperature and pressure. Effect of using different metal precursors and metal reducing co-reactants (oxygen sources) need to be studied in order to further understand and optimize the SALD process. This novel chemical approach of tuning the ALD nucleation site for SALD of metal oxides should also be extended to selective ALD of metals.

### **4.2.2 ALD on biomaterials**

Most problems related to biomaterials warrant surface modification, such as the deposition of thin films to modify its surface. Uniform film deposition on biomaterial surface is often challenging due to its 3-D nanostructured surface morphology and temperature sensitivity. The

unique ability of ALD in depositing highly conformal thin films on high aspect-ratio nanostructured surface offers potential for biomedical application. Low temperature operation of ALD further expands its applicability to temperature sensitive biomaterials (i.e., teeth, PMMA). These unique aspects of ALD process should be exploited to solve problems related to surface modification of biomaterials. In this thesis, ALD of  $\text{SnTiO}_x$  was performed on medically relevant titanium type-V alloy (Ti-6Al-4V), for implant related infection therapies. This problem needs to be studied further to increase photocatalytic property of the thin film and to develop visible light activated thin films.

## CITED LITERATURE

1. Selvaraj, S. K., Jursich, G., and Takoudis, C. G.: Design and implementation of a novel portable atomic layer deposition/chemical vapor deposition hybrid reactor. Review of Scientific Instruments, 84(9):095109, 2013.
2. Selvaraj, S. K. and Takoudis, C. G.: Scalable control program for multiprecursor flow-type atomic layer deposition system. Journal of Vacuum Science & Technology A, 33(1):013201, 2015.
3. Selvaraj, S. K., Feinerman, A., and Takoudis, C. G.: Growth behavior and properties of atomic layer deposited tin oxide on silicon from novel tin(II)acetylacetonate precursor and ozone. Journal of Vacuum Science & Technology A, 32(1):01A112, 2014.
4. Selvaraj, S. K., Colon, A., Rossero, J. I., Shi, J., and Takoudis, C. G.: Effect of using ethanol as the oxygen source on the growth and dielectric behavior of atomic layer deposited hafnium oxide. ECS Transactions, 61(6):93–102, 2014.
5. Selvaraj, S. K., Parulekar, J., and Takoudis, C. G.: Selective atomic layer deposition of zirconia on copper patterned silicon substrates using ethanol as oxygen source as well as copper reductant. Journal of Vacuum Science & Technology A, 32(1), 2014.
6. Puurunen, R. L.: Surface chemistry of atomic layer deposition: A case study for the trimethylaluminum/water process. Journal of Applied Physics, 97(12):121301, 2005.
7. Puurunen, R. L.: A short history of atomic layer deposition: Tuomo suntola’s atomic layer epitaxy. Chemical Vapor Deposition, 20(10-11-12):332–344, 2014.
8. Vaartstra, B. A.: Systems and methods for forming metal oxides using alcohols, US Patent WO2004020690, 2006.
9. Tarre, A., Aarik, J., Mandar, H., Niilisk, A., Parna, R., Rammula, R., Uustare, T., Rosental, A., and Sammelselg, V.: Atomic layer deposition of  $\text{Cr}_2\text{O}_3$  thin films: Effect of crystallization on growth and properties. Applied Surface Science, 254(16):5149–5156, 2008.



10. Hiltunen, L., Kattelus, H., Leskela, M., Makela, M., Niinisto, L., Nykanen, E., Soininen, P., and Tiittad, M.: Growth and characterization of aluminium oxide thin films deposited from various source materials by atomic layer epitaxy and chemical vapor deposition processes. Materials Chemistry and Physics, 28(4):379–388, 1991.
11. Lee, S. M., Pippel, E., Gosele, U., Dresbach, C., Qin, Y., Chandran, C. V., Brauniger, T., Hause, G., and Knez, M.: Greatly increased toughness of infiltrated spider silk. Science, 324(5926):488–492, 2009.
12. Tao, Q., Jursich, G., and Takoudis, C.: Selective atomic layer deposition of  $\text{HfO}_2$  on copper patterned silicon substrates. Applied Physics Letters, 96(19):192105, 2010.
13. Wiemer, C., Lamagna, L., and Fanciulli, M.: Atomic layer deposition of rare-earth-based binary and ternary oxides for microelectronic applications. Semiconductor Science and Technology, 27(7):074013, 2012.
14. Zhou, Y. N., Xue, M. Z., and Fu, Z. W.: Nanostructured thin film electrodes for lithium storage and all-solid-state thin-film lithium batteries. Journal of Power Sources, 234:310–332, 2013.
15. Coleman, J. J.: Metalorganic chemical vapor deposition for optoelectronic devices. Proceedings of the IEEE, 85(11):1715–1729, 1997.
16. Ohring, M.: Materials Science of Thin Films. San Diego, Academic Press, second edition, 2002.
17. Selvakumar, N. and Barshilia, H. C.: Review of physical vapor deposited (PVD) spectrally selective coatings for mid- and high-temperature solar thermal applications. Solar Energy Materials and Solar Cells, 98:1–23, 2012.
18. Haukka, S., Lakomaa, E. L., and Suntola, T.: Adsorption controlled preparation of heterogeneous catalysts. In Studies in Surface Science and Catalysis, volume 120, Part A, pages 715–750. Elsevier, 1999.
19. Hwang, C. and Lee, S.: Cluster tool for fabricating semiconductor device, US Patent US6530993 B2, 2003.
20. Zeng, X., Pogrebnyakov, A. V., Kotcharov, A., Jones, J. E., Xi, X. X., Lysczek, E. M., Redwing, J. M., Xu, S., Li, Q., Lettieri, J., Schlom, D. G., Tian, W., Pan, X.,

- and Liu, Z. K.: In situ epitaxial  $\text{MgB}_2$  thin films for superconducting electronics. Nature Materials, 1(1):35–38, 2002.
21. Reid, K. G. and Dip, A.: In-situ hybrid deposition of high dielectric constant films using atomic layer deposition and chemical vapor deposition, US Patent 7816278, 2010.
  22. Martin, P. M., Olsen, L. C., Johnston, J. W., and Depoy, D. M.: Hybrid deposition of sputtered and evaporated multilayer thin films. Journal of Vacuum Science & Technology B: Microelectronics and Nanometer Structures, 21(4):1384–1390, 2003.
  23. Mantovan, R., Vangelista, S., Kutrzeba-Kotowska, B., Cocco, S., Lamperti, A., Tallarida, G., Mameli, D., and Fanciulli, M.: Synthesis of magnetic tunnel junctions with full in situ atomic layer and chemical vapor deposition processes. Thin Solid Films, 520(14):4820–4822, 2012.
  24. Kala, S., Mehta, B. R., and Kruis, F. E.: A dual-deposition setup for fabricating nanoparticle-thin film hybrid structures. Review of Scientific Instruments, 79(1):013902, 2008.
  25. Choi, S. M., Park, K. C., Suh, B. S., Kim, I. R., Kang, H. K., Suh, K. P., Park, H. S., Ha, J. S., and Joo, D. K.: Process integration of CVD Cu seed using ALD Ru glue layer for sub-65nm Cu interconnect. In 2004 Symposium on VLSI Technology Digest of Technical Papers, page 64, Hawaii, 2004.
  26. Cheng, C. W. and Fitzgerald, E. A.: In situ metal-organic chemical vapor deposition atomic-layer deposition of aluminum oxide on GaAs using trimethylaluminum and isopropanol precursors. Applied Physics Letters, 93(3):031902, 2008.
  27. Suntola, T. and Hyvarinen, J.: Atomic layer epitaxy. Annual Review of Materials Science, 15(1):177–195, 1985.
  28. Reijnen, L., Meester, B., de Lange, F., Schoonman, J., and Goossens, A.: Comparison of  $\text{Cu}_x\text{S}$  films grown by atomic layer deposition and chemical vapor deposition. Chemistry of Materials, 17(10):2724–2728, 2005.
  29. Gaskell, J. M., Jones, A. C., Aspinall, H. C., Przybylak, S., Chalker, P. R., Black, K., Davies, H. O., Taechakumput, P., Taylor, S., and Critchlow, G. W.: Liquid injection ALD and MOCVD of lanthanum aluminate using a bimetallic alkoxide precursor. Journal of Materials Chemistry, 16(39):3854–3860, 2006.

30. Takoudis, C. G. and Singh, M. K.: Multi-metal films, alternating film multilayers, formation methods and deposition system, US Patent provisional application No.: 61251820, 2009.
31. Singh, M., Yang, Y., Takoudis, C. G., Tatarenko, A., Srinivasan, G., Kharel, P., and Lawes, G.: Metallorganic chemical-vapor-deposited bifeo<sub>3</sub> films for tunable high-frequency devices. Electrochemical and Solid-State Letters, 12(5):H161–H164, 2009.
32. Singh, M. K., Yang, Y., Takoudis, C. G., Tatarenko, A., Srinivasan, G., Kharel, P., and Lawes, G.: Multiferroic BiFeO<sub>3</sub> thin films for multifunctional devices. Journal of Nanoscience and Nanotechnology, 10(9):6195–6199, 2010.
33. Xu, R., Huang, J., Ghosh, S., and Takoudis, C. G.: Deposition and characterization of atomic layer deposited ZnS thin films on p-type GaSb(100) using diethylzinc precursor and hydrogen sulfide. ECS Transactions, 41(2):229–236, 2011.
34. Xu, R., Selvaraj, S. K., Azimi, N., and Takoudis, C. G.: Growth characteristics and properties of yttrium oxide thin films by atomic layer deposition from novel Y(iPrCp)<sub>3</sub> precursor and O<sub>3</sub>. ECS Transactions, 50(13):107–116, 2013.
35. Xu, R. and Takoudis, C. G.: Atomic layer deposition and characterization of amorphous Er<sub>x</sub>Ti<sub>1-x</sub>O<sub>y</sub> dielectric ultra-thin films. ECS Journal of Solid State Science and Technology, 1(6):N107–N114, 2012.
36. Xu, R., Tao, Q., Yang, Y., and Takoudis, C. G.: Atomic layer deposition and characterization of stoichiometric erbium oxide thin dielectrics on Si(1 0 0) using (CpMe)<sub>3</sub>Er precursor and ozone. Applied Surface Science, 258(22):8514–8520, 2012.
37. Kimes, W. A., Moore, E. F., and Maslar, J. E.: Perpendicular-flow, single-wafer atomic layer deposition reactor chamber design for use with in situ diagnostics. Review of Scientific Instruments, 83(8):083106, 2012.
38. Majumder, P., Jursich, G., Kueltoz, A., and Takoudis, C.: Atomic layer deposition of Y<sub>2</sub>O<sub>3</sub> films on silicon using tris(ethylcyclopentadienyl) yttrium precursor and water vapor. Journal of The Electrochemical Society, 155(8):G152–G158, 2008.
39. Sang, B. and Konagai, M.: Growth of transparent conductive oxide ZnO films by atomic layer deposition. Japanese Journal of Applied Physics, 35:L602–L605, 1996.

40. Vig, J. R.: UV/ozone cleaning of surfaces. Journal of Vacuum Science & Technology A: Vacuum, Surfaces, and Films, 3(3):1027–1034, 1985.
41. Lippmann, M.: Health effects of ozone: A critical review. Journal of the Air Pollution Control Association, 39(5):672–695, 1989.
42. Peacock, R. N.: Practical selection of elastomer materials for vacuum seals. Journal of Vacuum Science and Technology, 17(1):330–336, 1980.
43. Katamreddy, R., Omarjee, V., Feist, B., and Dussarrat, C.: Ti source precursors for atomic layer deposition of  $\text{TiO}_2$ , STO and BST. ECS Transactions, 16(4):113–122, 2008.
44. Maruyama, T. and Ikuta, Y.: Tin dioxide thin films prepared by chemical vapor deposition from tin(II) acetylacetonate. Solar Energy Materials and Solar Cells, 28(3):209–215, 1992.
45. Fortunato, E., Barros, R., Barquinha, P., Figueiredo, V., Park, S. H. K., Hwang, C. S., and Martins, R.: Transparent p-type  $\text{SnO}_x$  thin film transistors produced by reactive rf magnetron sputtering followed by low temperature annealing. Applied Physics Letters, 97(5):052105, 2010.
46. Njoroge, W. K., Woltgens, H. W., and Wuttig, M.: Density changes upon crystallization of  $\text{Ge}_2\text{Sb}_{2.04}\text{Te}_{4.74}$  films. Journal of Vacuum Science & Technology A: Vacuum, Surfaces, and Films, 20(1):230–233, 2002.
47. George, S. M.: Atomic layer deposition: An overview. Chemical Reviews, 110(1):111–131, 2009.
48. Tao, Q., Kueltzo, A., Singh, M., Jursich, G., and Takoudis, C. G.: Atomic layer deposition of  $\text{HfO}_2$ ,  $\text{TiO}_2$ , and  $\text{Hf}_x\text{Ti}_{1-x}\text{O}_2$  using metal (diethylamino) precursors and  $\text{H}_2\text{O}$ . Journal of The Electrochemical Society, 158(2):G27–G33, 2011.
49. Hong, T., Jeong, E. D., Byeon, M. R., Kang, Y. B., Yang, H. S., and Kim, S. H.: Characterization of a Ru-based ternary-oxide thin film for a diffusion barrier. Journal of the Korean Physical Society, 61(6):984–987, 2012.
50. Holme, T. P., Lee, C., and Prinz, F. B.: Atomic layer deposition of LSM cathodes for solid oxide fuel cells. Solid State Ionics, 179(27-32):1540–1544, 2008.

51. Thimsen, E., Riha, S. C., Baryshev, S. V., Martinson, A. B. F., Elam, J. W., and Pellin, M. J.: Atomic layer deposition of the quaternary chalcogenide  $\text{Cu}_2\text{ZnSnS}_4$ . Chemistry of Materials, 24(16):3188–3196, 2012.
52. Fuller, M. J. and Warwick, M. E.: The catalytic oxidation of carbon monoxide on tin(IV) oxide. Journal of Catalysis, 29(3):441–450, 1973.
53. Hjortsberg, A., Hamberg, I., and Granqvist, C. G.: Transparent and heat-reflecting indium tin oxide films prepared by reactive electron beam evaporation. Thin Solid Films, 90(3):323–326, 1982.
54. Gordon, R. G., Proscia, J., Ellis Jr, F. B., and Delahoy, A. E.: Textured tin oxide films produced by atmospheric pressure chemical vapor deposition from tetramethyltin and their usefulness in producing light trapping in thin film amorphous silicon solar cells. Solar Energy Materials, 18(5):263–281, 1989.
55. Hosono, H., Ohta, H., Orita, M., Ueda, K., and Hirano, M.: Frontier of transparent conductive oxide thin films. Vacuum, 66(3-4):419–425, 2002.
56. Huang, X. J., Choi, Y. K., Yun, K. S., and Yoon, E.: Oscillating behaviour of hazardous gas on tin oxide gas sensor: Fourier and wavelet transform analysis. Sensors and Actuators B: Chemical, 115(1):357–364, 2006.
57. Kim, Y., Jang, J. H., Kim, J. S., Kim, S. D., and Kim, S. E.: Nitrogen doped p-type  $\text{SnO}$  thin films deposited via sputtering. Materials Science and Engineering B, 177(16):1470–1475, 2012.
58. Batzill, M. and Diebold, U.: The surface and materials science of tin oxide. Progress in Surface Science, 79(2-4):47–154, 2005.
59. Edelman, F., Brener, R., Cytermann, C., Eizenberg, M., Weil, R., and Beyer, W.: Fast interfacial oxidation of amorphous  $\text{Si}_{1-x}\text{Ge}_x\text{:H}$  by  $\text{SnO}_2$ . Applied Physics Letters, 67(3):389–391, 1995.
60. Maddalena, A., Dal Maschio, R., Dire, S., and Raccanelli, A.: Electrical conductivity of tin oxide films prepared by the sol-gel method. Journal of Non-Crystalline Solids, 121(1-3):365–369, 1990.

61. Sundqvist, J., Lu, J., Ottosson, M., and Harsta, A.: Growth of SnO<sub>2</sub> thin films by atomic layer deposition and chemical vapour deposition: A comparative study. Thin Solid Films, 514(1-2):63–68, 2006.
62. Joshi, B. N., Yoon, H., and Yoon, S. S.: Structural, optical and electrical properties of tin oxide thin films by electrostatic spray deposition. Journal of Electrostatics, 71(1):48–52, 2013.
63. Bruneaux, J., Cachet, H., Froment, M., and Messad, A.: Correlation between structural and electrical properties of sprayed tin oxide films with and without fluorine doping. Thin Solid Films, 197(1-2):129–142, 1991.
64. Jin, C., Yamazaki, T., Ito, K., Kikuta, T., and Nakatani, N.: H<sub>2</sub>S sensing property of porous SnO<sub>2</sub> sputtered films coated with various doping films. Vacuum, 80(7):723–725, 2006.
65. Du, X. and George, S. M.: Thickness dependence of sensor response for CO gas sensing by tin oxide films grown using atomic layer deposition. Sensors and Actuators B: Chemical, 135(1):152–160, 2008.
66. Elam, J. W., Baker, D. A., Hryn, A. J., Martinson, A. B. F., Pellin, M. J., and Hupp, J. T.: Atomic layer deposition of tin oxide films using tetrakis(dimethylamino) tin. Journal of Vacuum Science and Technology A, 26(2):244–252, 2008.
67. Choi, W. S.: The fabrication of tin oxide films by atomic layer deposition using tetrakis(ethylmethylamino) tin precursor. Transactions on Electrical and Electronic Materials, 10(6):200–202, 2009.
68. Natarajan, G. and Cameron, D.: Influence of oxygen depletion layer on the properties of tin oxide gas-sensing films fabricated by atomic layer deposition. Applied Physics A, 95(3):621–627, 2009.
69. Heo, J., Hock, A. S., and Gordon, R. G.: Low temperature atomic layer deposition of tin oxide. Chemistry of Materials, 22(17):4964–4973, 2010.
70. Heo, J., Kim, S. B., and Gordon, R. G.: Atomic layer deposition of tin oxide with nitric oxide as an oxidant gas. Journal of Materials Chemistry, 22(11):4599–4602, 2012.
71. Lee, B. K., Jung, E., Kim, S. H., Moon, D. C., Lee, S. S., Park, B. K., Hwang, J. H., Chung, T. M., Kim, C. G., and An, K. S.: Physical/chemical properties of tin

oxide thin film transistors prepared using plasma-enhanced atomic layer deposition. Materials Research Bulletin, 47(10):3052–3055, 2012.

72. Xu, R., Selvaraj, S. K., Jursich, G., Feinerman, A., and Takoudis, C.: Nucleation behavior-morphology-resistivity of atomic layer deposited Pt on atomic layer deposited yttria-stabilized zirconia films. ECS Journal of Solid State Science and Technology, 2(11):P452–P456, 2013.
73. Kitagawa, M., Mori, K., Ishihara, S., Ohno, M., Hirao, T., Yoshioka, Y., and Kohiki, S.: Interaction of hydrogenated amorphous silicon films with transparent conductive films. Journal of Applied Physics, 54(6):3269–3271, 1983.
74. Perry, R. H. and Green, D. W.: Perry’s Chemical Engineers’ Handbook. New York, McGraw-Hill, 7th edition, 1997.
75. Cho, S., Yu, J., Kang, S., and Shih, D. Y.: Oxidation study of pure tin and its alloys via electrochemical reduction analysis. Journal of Electronic Materials, 34(5):635–642, 2005.
76. Ellmer, K.: Resistivity of polycrystalline zinc oxide films: current status and physical limit. Journal of Physics D: Applied Physics, 34(21):3097, 2001.
77. Shanthi, E., Banerjee, A., Dutta, V., and Chopra, K. L.: Annealing characteristics of tin oxide films prepared by spray pyrolysis. Thin Solid Films, 71(2):237–244, 1980.
78. Park, S. S. and Mackenzie, J. D.: Sol-gel-derived tin oxide thin films. Thin Solid Films, 258(1-2):268–273, 1995.
79. Niinisto, L., Nieminen, M., Paivasaari, J., Niinisto, J., and Putkonen, M.: Advanced electronic and optoelectronic materials by atomic layer deposition: An overview with special emphasis on recent progress in processing of high-k dielectrics and other oxide materials. physica status solidi (a), 201(7):1443–1452, 2004.
80. Marichy, C., Bechelany, M., and Pinna, N.: Atomic layer deposition of nanostructured materials for energy and environmental applications. Advanced Materials, 24(8):1017–1032, 2012.
81. Li, J., Mayer, J. W., and Colgan, E. G.: Oxidation and protection in copper and copper alloy thin films. Journal of Applied Physics, 70(5):2820–2827, 1991.

82. Jiang, X. and Bent, S. F.: Area-selective atomic layer deposition of platinum on YSZ substrates using microcontact printed SAMs. Journal of The Electrochemical Society, 154(12):D648–D656, 2007.
83. Tao, Q., Overhage, K., Jursich, G., and Takoudis, C.: On the initial growth of atomic layer deposited TiO<sub>2</sub> films on silicon and copper surfaces. Thin Solid Films, 520(22):6752–6756, 2012.
84. Apen, E., Rogers, B. R., and Sellers, J. A.: X-ray photoelectron spectroscopy characterization of the oxidation of electroplated and sputter deposited copper surfaces. Journal of Vacuum Science and Technology A, 16(3):1227–1232, 1998.
85. Sexton, B. A.: Surface vibrations of adsorbed intermediates in the reaction of alcohols with Cu(100). Surface Science, 88(2-3):299–318, 1979.
86. Satta, A., Shamiryan, D., Baklanov, M. R., Whelan, C. M., Toan Le, Q., Beyer, G. P., Vantomme, A., and Maex, K.: The removal of copper oxides by ethyl alcohol monitored in situ by spectroscopic ellipsometry. Journal of The Electrochemical Society, 150(5):G300–G306, 2003.
87. Soininen, P. J., Elers, K. E., Saanila, V., Kaipio, S., Sajavaara, T., and Haukka, S.: Reduction of copper oxide film to elemental copper. Journal of The Electrochemical Society, 152(2):G122–G125, 2005.
88. Lide, D. R.: CRC Handbook of Chemistry and Physics. CRC Press, 85th edition, 2005.
89. James, C., Xu, R., Jursich, G., and Takoudis, C. G.: Atomic layer deposition of zirconium oxide for fuel cell applications. Journal of Undergraduate Research, 5(1), 2012.
90. Luts, T. and Katz, A.: Chemisorption and dehydration of ethanol on silica: Effect of temperature on selectivity. Topics in Catalysis, 55(1-2):84–92, 2012.
91. Chary, K. V. R., Sagar, G. V., Srikanth, C. S., and Rao, V. V.: Characterization and catalytic functionalities of copper oxide catalysts supported on zirconia. Journal of Physical Chemistry B, 111(3):543–550, 2006.
92. Wachs, I. E. and Madix, R. J.: The oxidation of ethanol on Cu(110) and Ag(110) catalysts. Applications of Surface Science, 1(3):303–328, 1978.



93. Majumder, P., Katamreddy, R., and Takoudis, C.: Effect of film thickness on the breakdown temperature of atomic layer deposited ultrathin  $\text{HfO}_2$  and  $\text{Al}_2\text{O}_3$  diffusion barriers in copper metallization. Journal of Crystal Growth, 309(1):12–17, 2007.
94. Choi, J. H., Mao, Y., and Chang, J. P.: Development of hafnium based high-k materials - a review. Materials Science and Engineering: R: Reports, 72(6):97–136, 2011.
95. Mistry, K., Allen, C., Auth, C., Beattie, B., Bergstrom, D., Bost, M., Brazier, M., Buehler, M., Cappellani, A., Chau, R., Choi, C. H., Ding, G., Fischer, K., Ghani, T., Grover, R., Han, W., Hanken, D., Hattendorf, M., He, J., Hicks, J., Huessner, R., Ingerly, D., Jain, P., James, R., Jong, L., Joshi, S., Kenyon, C., Kuhn, K., Lee, K., Liu, H., Maiz, J., McIntyre, B., Moon, P., Neiryneck, J., Pae, S., Parker, C., Parsons, D., Prasad, C., Pipes, L., Prince, M., Ranade, P., Reynolds, T., Sandford, J., Shifren, L., Sebastian, J., Seiple, J., Simon, D., Sivakumar, S., Smith, P., Thomas, C., Troeger, T., Vandervoorn, P., Williams, S., and Zawadzki, K.: A 45nm logic technology with high-k+metal gate transistors, strained silicon, 9 Cu interconnect layers, 193nm dry patterning, and 100% Pb-free packaging. In Electron Devices Meeting, 2007. IEDM 2007. IEEE International, pages 247–250, 2007.
96. Robertson, J.: High dielectric constant oxides. The European Physical Journal - Applied Physics, 28(03):265–291, 2004.
97. Li, S., Han, L., and Chen, Z.: The interfacial quality of  $\text{HfO}_2$  on silicon with different thicknesses of the chemical oxide interfacial layer. Journal of the Electrochemical Society, 157(11):G221–G224, 2010.
98. Riikka, L. P.: Surface chemistry of atomic layer deposition: A case study for the trimethylaluminum/water process. Journal of Applied Physics, 97(12):121301, 2005.
99. Cho, M., Park, J., Park, H. B., Hwang, C. S., Jeong, J., and Hyun, K. S.: Chemical interaction between atomic-layer-deposited  $\text{HfO}_2$  thin films and the Si substrate. Applied Physics Letters, 81(2):334–336, 2002.
100. Qian, T., Jursich, G. M., and Takoudis, C.: Investigation of surface sputtering and post annealing effects on atomic layer deposited  $\text{HfO}_2$  and  $\text{TiO}_2$ . IEEE Transactions on Semiconductor Manufacturing, 24(2):139–144, 2011.
101. Katamreddy, R., Inman, R., Jursich, G., Soulet, A., and Takoudis, C.: Nitridation and oxynitridation of Si to control interfacial reaction with  $\text{HfO}_2$ . Thin Solid Films, 516(23):8498–8506, 2008.

102. Deshpande, A., Inman, R., Jursich, G., and Takoudis, C.: Characterization of hafnium oxide grown on silicon by atomic layer deposition: Interface structure. Microelectronic Engineering, 83(3):547–552, 2006.
103. Lysaght, P. S., Foran, B., Bersuker, G., Chen, P. J., Murto, R. W., and Huff, H. R.: Physicochemical properties of  $\text{HfO}_2$  in response to rapid thermal anneal. Applied Physics Letters, 82(8):1266–1268, 2003.
104. Black, K., Aspinall, H. C., Jones, A. C., Przybylak, K., Bacsa, J., Chalker, P. R., Taylor, S., Zhao, C. Z., Elliott, S. D., Zydor, A., and Heys, P. N.: Deposition of  $\text{ZrO}_2$  and  $\text{HfO}_2$  thin films by liquid injection MOCVD and ALD using ansa-metallocene zirconium and hafnium precursors. Journal of Materials Chemistry, 18(38):4561–4571, 2008. 10.1039/B807205A.
105. Green, M. L., Ho, M.-Y., Busch, B., Wilk, G. D., Sorsch, T., Conard, T., Brijs, B., Vandervorst, W., Raisanen, P. I., Muller, D., Bude, M., and Grazul, J.: Nucleation and growth of atomic layer deposited  $\text{HfO}_2$  gate dielectric layers on chemical oxide (Si-O-H) and thermal oxide ( $\text{SiO}_2$  or Si-O-N) underlayers. Journal of Applied Physics, 92(12):7168–7174, 2002.
106. Bersuker, G., Zeitzoff, P., Brown, G., and Huff, H. R.: Dielectrics for future transistors. Materials Today, 7(1):26–33, 2004.
107. Krylov, I., Kornblum, L., Gavrilov, A., Ritter, D., and Eizenberg, M.: Experimental evidence for the correlation between the weak inversion hump and near midgap states in dielectric/ $\text{InGaAs}$  interfaces. Applied Physics Letters, 100(17):173508–173508, 2012.
108. Zhu, W. J., Tamagawa, T., Gibson, M., Furukawa, T., and Ma, T. P.: Effect of Al inclusion in  $\text{HfO}_2$  on the physical and electrical properties of the dielectrics. IEEE Electron Device Letters, 23(11):649–651, 2002.
109. Heasman, P., Esmail, Z., and Barclay, C.: Peri-implant diseases. Dental Update, 37(8):511–512, 2010.
110. Mombelli, A., Muller, N., and Cionca, N.: The epidemiology of peri-implantitis. Clinical Oral Implants Research, 23:67–76, 2012.
111. Mombelli, A. and Lang, N. P.: The diagnosis and treatment of peri-implantitis. Periodontology 2000, 17(1):63–76, 1998.

112. Pye, A. D., Lockhart, D. E. A., Dawson, M. P., Murray, C. A., and Smith, A. J.: A review of dental implants and infection. Journal of Hospital Infection, 72(2):104–110, 2009.
113. Renvert, S., Roos-Jansaker, A. M., and Claffey, N.: Non-surgical treatment of peri-implant mucositis and peri-implantitis: a literature review. Journal of Clinical Periodontology, 35:305–315, 2008.
114. Patel, S. B., Hamlekhan, A., Royhman, D., Butt, A., Yuan, J., Shokuhfar, T., Sukotjo, C., Mathew, M. T., Jursich, G., and Takoudis, C. G.: Enhancing surface characteristics of Ti-6Al-4V for bio-implants using integrated anodization and thermal oxidation. Journal of Materials Chemistry B, 2(23):3597–3608, 2014.
115. Riley, D. J., Bavastrello, V., Covani, U., Barone, A., and Nicolini, C.: An in-vitro study of the sterilization of titanium dental implants using low intensity UV-radiation. Dental Materials, 21(8):756–760, 2005.
116. Visai, L., De Nardo, L., Punta, C., Melone, L., Cigada, A., Imbriani, M., and Arciola, C. R.: Titanium oxide antibacterial surfaces in biomedical devices. International Journal of Artificial Organs, 34(9):929–46, 2011.
117. Maness, P. C., Smolinski, S., Blake, D. M., Huang, Z., Wolfrum, E. J., and Jacoby, W. A.: Bactericidal activity of photocatalytic TiO<sub>2</sub> reaction: Toward an understanding of its killing mechanism. Applied and Environmental Microbiology, 65(9):4094–4098, 1999.
118. Lin, J., Yu, J. C., Lo, D., and Lam, S. K.: Photocatalytic activity of rutile Ti<sub>1-x</sub>Sn<sub>x</sub>O<sub>2</sub> solid solutions. Journal of Catalysis, 183(2):368–372, 1999.
119. Velten, D., Biehl, V., Aubertin, F., Valeske, B., Possart, W., and Breme, J.: Preparation of TiO<sub>2</sub> layers on cp-Ti and Ti6Al4V by thermal and anodic oxidation and by sol-gel coating techniques and their characterization. Journal of Biomedical Materials Research, 59(1):18–28, 2002.
120. Pore, V., Rahtu, A., Leskela, M., Ritala, M., Sajavaara, T., and Keinonen, J.: Atomic layer deposition of photocatalytic TiO<sub>2</sub> thin films from titanium tetramethoxide and water. Chemical Vapor Deposition, 10(3):143–148, 2004.

121. Pyun, M. W., Kim, E. J., Yoo, D. H., and Hahn, S. H.: Oblique angle deposition of  $\text{TiO}_2$  thin films prepared by electron-beam evaporation. Applied Surface Science, 257(4):1149–1153, 2010.
122. Brunette, D. M., Tengvall, P., Textor, M., and Thomsen, P.: Titanium in medicine: Material science, surface science, engineering, biological responses and medical applications. Berlin ; New York, Springer, 2001.
123. Cao, Y., Zhang, X., Yang, W., Du, H., Bai, Y., Li, T., and Yao, J.: A bicomponent  $\text{TiO}_2/\text{SnO}_2$  particulate film for photocatalysis. Chemistry of Materials, 12(11):3445–3448, 2000.
124. Li, X., Xiong, R., and Wei, G.: Preparation and photocatalytic activity of nanoglued Sn-doped  $\text{TiO}_2$ . Journal of Hazardous materials, 164(2-3):587–591, 2009.
125. Sayilkan, F., Asilturk, M., Kiraz, N., Burunkaya, E., Arpac, E., and Sayilkan, H.: Photocatalytic antibacterial performance of  $\text{Sn}^{4+}$ -doped  $\text{TiO}_2$  thin films on glass substrate. Journal of Hazardous materials, 162(2-3):1309–1316, 2009.
126. Kaleji, B., Sarraf-Mamoory, R., Nakata, K., and Fujishima, A.: The effect of Sn dopant on crystal structure and photocatalytic behavior of nanostructured titania thin films. Journal of Sol-Gel Science and Technology, 60(2):99–107, 2011.
127. Cheng, H. E., Hsu, C. M., and Chen, Y. C.: Substrate materials and deposition temperature dependent growth characteristics and photocatalytic properties of ALD  $\text{TiO}_2$  films. Journal of the Electrochemical Society, 156(8):D275–D278, 2009.
128. Augthun, M. and Conrads, G.: Microbial findings of deep peri-implant bone defects. International Journal of Oral & Maxillofacial Implants, 12:1–12, 1997.
129. Qian, T., Jursich, G. M., and Takoudis, C.: Investigation of surface sputtering and post annealing effects on atomic layer deposited  $\text{HfO}_2$  and  $\text{TiO}_2$ . IEEE Transactions on Semiconductor Manufacturing, 24(2):139–144, 2011.
130. Choi, J. Y., Kim, K. H., Choy, K. C., Oh, K. T., and Kim, K. N.: Photocatalytic antibacterial effect of  $\text{TiO}_2$  film formed on Ti and TiAg exposed to lactobacillus acidophilus. Journal of Biomedical Materials Research Part B: Applied Biomaterials, 80B(2):353–359, 2007.

131. Sittig, C., Textor, M., Spencer, N. D., Wieland, M., and Vallotton, P. H.: Surface characterization. Journal of Materials Science: Materials in Medicine, 10(1):35–46, 1999.
132. Wu, C. Y., Lee, Y. L., Lo, Y. S., Lin, C. J., and Wu, C. H.: Thickness-dependent photocatalytic performance of nanocrystalline  $\text{TiO}_2$  thin films prepared by sol-gel spin coating. Applied Surface Science, 280(0):737–744, 2013.
133. Suketa, N., Sawase, T., Kitauro, H., Naito, M., Baba, K., Nakayama, K., Wennerberg, A., and Atsuta, M.: An antibacterial surface on dental implants, based on the photocatalytic bactericidal effect. Clinical Implant Dentistry and Related Research, 7(2):105–111, 2005.
134. Occupational exposure to ultraviolet radiation, National Institute for Occupational Safety and Health standard, 1972.

## APPENDICES

## Appendix A

### PERMISSION TO USE PREVIOUSLY PUBLISHED MATERIALS

Chapter 2.1 was previously published as "Design and implementation of a novel portable atomic layer deposition/chemical vapor deposition hybrid reactor" in Review of Scientific Instruments (RSI) journal. RSI journal (American Institute of Physics (AIP)) permits authors to use their paper in thesis. The following statement is given in AIP webpage <http://publishing.aip.org/authors/copyright-reuse>

"AIP permits authors to include their published articles in a thesis or dissertation. It is understood that the thesis or dissertation may be published in print and/or electronic form and offered for sale, as well as included in a university's repository. Formal permission from AIP is not needed. If the university requires written permission, however, we are happy to supply it."

Chapters 2.2, 3.1 & 3.2 were previously published in Journal of Vacuum Science & Technology A (JVST). JVST is published by American Vacuum Society (AVS) through AIP. As a member of AIP, AVS also follows AIP's policies. The following statement is taken from JVST webpage <http://scitation.aip.org/content/avs/journal/jvsta/info/authors>

"As a Member Society of the American Institute of Physics (AIP) and as a close partner, AVS adheres to the policies outlined by AIP in their statement of ethics and responsibilities of authors submitting to AVS Journals."

## Appendix A (Continued)

Chapter 3.3 was previously published as "Effect of using ethanol as the oxygen source on the growth and dielectric behavior of atomic layer deposited hafnium oxide" in ECS Transactions.

Written permission from ECS is given in the next page.



## Appendix A (Continued)

**Request for Permission to Reproduce or Re-Publish ECS Material**

Please fax this form to: The Electrochemical Society (ECS), Attn: Permissions Requests, 1.609.730.0629.  
You may also e-mail your request to: [copyright@electrochem.org](mailto:copyright@electrochem.org). Include all the information as required on this form. Please allow 3-7 days for your request to be processed.

I am preparing a (choose one): ☐ paper ☐ chapter ☐ book ☒ thesis

entitled: Atomic Layer Deposition of Metal Oxides

to be published by: University of Illinois at Chicago

in an upcoming publication entitled: PhD Thesis

I request permission to use the following material in the publication noted above, and request nonexclusive rights for all subsequent editions and in all foreign language translations for distribution throughout the world.

**Description of material to be used**—Indicate what material you wish to use (figures, tables, text, etc.) and give the full bibliographic reference for the source publication. You may attach a separate list, organized by ECS title.

Material to be used: Full text and figures as a chapter in the above mentioned PhD thesis.

Title: Effect of Using Ethanol as the Oxygen Source on the Growth and Dielectric Behavior of Atomic Layer Deposited Hafnium Oxide;

Authors: Sathees Kannan Selvaraj, Albert Colon, Jorge Iván Rossero, Junxia Shi, and Christos G. Takoudis.

doi: 10.1149/06106.0093ecst

ECS Transactions. 2014 volume 61, issue 6, 93-102.

Signature: S. Sathees Kannan Selvaraj

Date: 04/14/2015

Name: Sathees Kannan Selvaraj

Address: 851 S Morgan Street,  
Room 218-SEQ,  
Chicago, IL 60607

Telephone: 773-870-1562

Fax: \_\_\_\_\_

E-mail: sselva2@uic.edu

Permission is granted to include the above-referenced papers in your thesis, provided that you obtain permission of the other individual authors. In the thesis, please acknowledge the authors and the citations given above, and include the words: "Reproduced by permission of ECS — The Electrochemical Society."

April 24, 2015  
Date

Ann F. Goedkoop  
Ann F. Goedkoop, Publications Production Director

## Appendix B

### COAUTHORED PROJECTS

#### B.1 ALD on dentinal tubules

Organic acids produced by bacteria on tooth surface cause loss of minerals from tooth. Lost minerals are regenerated from saliva. Dental caries happen, when the balance between demineralization and remineralization is disturbed. Dental caries results in tooth decay. We developed a novel strategy in which, mineral attracting chemical species or minerals itself are infiltrated in to dentin component of tooth. Such mineral infiltration will expedite remineralization and prevent tooth decay. Dentin is made up of calcium hydroxyapatite matrix in the form of tubules. Dentin tubules are of  $\sim 1$  micron diameter that are separated at  $\sim 5$ -10 microns apart. As a pilot study, long exposure ALD of  $\text{TiO}_2$  was performed to infiltrate titanium oxide into dentin. Tetrakis(diethylamino)titanium and ozone were used as titanium and oxygen source respectively. ALD was performed at  $100^\circ\text{C}$  substrate temperature and 0.5 torr pressure. Precursor exposure time was doubled (from 8 s to 16 s) to improve conformality in the high aspect ratio (1000) tubules. Other ALD parameters were same as mentioned in chapter 2.1. 1 mm thick dentin blocks were used as substrate. ALD process resulted in uniform coating of  $\text{TiO}_2$  inside dentin tubules with average Ti atom percentage of 26 %. The novel coating resulted in increased nucleation and growth of calcium and phosphate crystals on dentin surface.

## Appendix B (Continued)

Further process improvements need to be done to expedite nucleation of minerals inside dentin tubules.

### **B.2    ALD on silicone and PMMA**

ALD on polymeric materials were studied for different applications. Temperature sensitivity of polymer causes ALD on polymeric substrates challenging. In this study, we tried ALD of  $\text{TiO}_2$  on silicone (PDMS - polydimethylsiloxane) and PMMA (poly(methylmethacrylate)). ALD on silicone was studied to get photoactivated antibacterial surface on prosthetic silicone materials. ALD on silicone was performed at temperatures ranging from 100 - 250 °C. Poor nucleation of ALD precursors on completely methylated silicone surface makes the ALD process challenging. Efforts are being taken to oxidize and hydroxylate silicone surface using air/oxygen plasma. Plasma treatment is expected to aid ALD nucleation and  $\text{TiO}_2$  film growth. ALD on PMMA was studied to improve its surface mechanical properties such as, surface hardness, wear resistance and reduced water absorptivity. Unlike silicone, PMMA has low melting point (160 °C). ALD on PMMA was performed at 80 - 100 °C. Even though  $\text{TiO}_2$  film growth was achieved on PMMA surface, the films peeled off from the surface upon sonication. Surface pretreatment of PMMA and/or the use of metal precursors that react at low temperatures (< 100) could help improve the film adhesion.

## VITA

## Sathees Kannan Selvaraj

Education	<p>Ph.D., Chemical Engineering University of Illinois at Chicago, USA June 2015</p> <p>M.Tech., Chemical Engineering Indian Institute of Technology Kanpur, India May 2009</p> <p>B.Tech., Chemical Engineering Coimbatore Institute of Technology, India May 2007</p>
Experience	<p>Development Engineer Larsen &amp; Toubro Ltd., India 2009 - 2011</p>
Patent	<p>Takoudis C. G., Singh M. K. and Selvaraj S. K.: Multi-metal films, alternating film multilayers, formation methods and deposition system, in the process of filing <u>U.S. Patent</u> (2015)</p>
Publications	<p>Selvaraj S. K., Chang S., Bishal A. K., Butt A. and Takoudis C. G.: Photoactivated disinfection of titanium dental implants coated with atomic layer deposited tin-doped titanium oxide, Submitted.</p> <p>Selvaraj S. K. and Takoudis C. G.: Scalable control program for multi-precursor flow-type atomic layer deposition system, <u>Journal of Vacuum Science and Technology A</u>, 33, 013201 (2015).</p>

## Publications

Selvaraj S. K., Parulekar J. and Takoudis C. G.: Selective atomic layer deposition of zirconia on copper patterned silicon substrates using ethanol as oxygen source as well as copper reductant, Journal of Vacuum Science and Technology A, 32, 010601 (2014).

Selvaraj S. K., Colon A., Rossero J. I., Shi J. and Takoudis C. G.: Effect of using ethanol as the oxygen source on the growth and dielectric behavior of atomic layer deposited hafnium oxide, ECS Transactions, 61(6): 93 (2014).

Selvaraj S. K., Feinerman A. and Takoudis C. G.: Growth behavior and properties of atomic layer deposited tin oxide on silicon from novel tin(II) acetylacetonate precursor and ozone, Journal of Vacuum Science and Technology A, 32, 01A112 (2014).

Selvaraj S. K., Jursich G. and Takoudis C. G.: Design and implementation of a novel portable atomic layer deposition / chemical vapor deposition hybrid reactor, Review of Scientific Instruments, 84(9), 095109 (2013).

Xu R., Selvaraj S. K., Jursich G., Feinerman A. and Takoudis C. G.: Nucleation behavior-morphology-resistivity of atomic layer deposited Pt on atomic layer deposited Yttria-stabilized zirconia films, ECS Journal of Solid State Science & Technology, 2 (11), P452 (2013).

Xu R., Selvaraj S. K., Azimi N. and Takoudis C. G.: Growth characteristics and properties of Yttrium oxide thin films by atomic layer deposition from novel Y(iPrCp)<sub>3</sub> Precursor and O<sub>3</sub>, ECS Transactions, 50 (13), 107 (2013).